Durham E-Theses

Three dimensional frequency-domain solution method for unsteady turbomachinery flows

Vasanthakumar, Parthasarathy

University
of Durham

School of Engineering

THREE DIMENSIONAL FREQUENCY-DOMAIN SOLUTION
METHOD FOR UNSTEADY TURBOMACHINERY FLOWS

Parthasarathy Vasanthakumar

2 9 JAN 2003

A thesis submitted for the degree of
Doctor of Philosophy

School of Engineering
University of Durham
2003

Abstract

The three-dimensional calculation of unsteady flows is increasingly gaining importance in the prediction of turbomachinery flow problems. A three-dimensional Euler/Navier-Stokes solver incorporating the time-linearized method and the nonlinear harmonic method in the frequency domain has been developed for predicting unsteady turbomachinery flows.

In the time-linearized method, the flow is decomposed into a steady part and a harmonic perturbation part. Linearization results in a steady flow equation and a time-linearized perturbation equation. A pseudo-time time-marching technique is introduced to time-march them. A cell centred finite volume scheme is employed for spatial discretization and the time integration involves a four stage Runge Kutta scheme. Nonreflecting boundary conditions are applied for far field boundaries and a slip wall boundary condition is used for Navier-Stokes calculations. In the nonlinear harmonic method, the flow is assumed to be composed of a time-averaged part and an unsteady perturbation part. Due to the nonlinearity of the unsteady equations, time-averaging produces extra unsteady stress terms in the time-averaged equation which are evaluated from unsteady perturbations. While the unsteady perturbations are obtained from solving the harmonic perturbation equation, the coefficients of perturbation equations come from the solution of time-averaged equation and this interaction is achieved through a strong coupling procedure. In order to handle flows with strong nonlinearity, a cross coupling of higher order harmonics through a harmonic balancing technique is also employed. The numerical solution method is similar to that used in the time-linearized method.

The numerical validation includes several test cases involving linear and nonlinear unsteady flows with specific attention to flows around oscillating blades. The results have been compared with other well developed linear methods, nonlinear time-marching method and experimental data. The nonlinear harmonic method is able to predict strong nonlinearities associated with shock oscillations well but some limitations have also been observed. A three-dimensional prediction of unsteady viscous flows through a linear compressor cascade with 3D blade oscillation, probably the first of its kind, has shown that unsteady flow calculation in the frequency domain is able to predict three-dimensional blade oscillations reasonably well.

Declaration

This thesis is based on research carried out by the author during the period January 1999- September 2002 at University of Durham, under the supervision of Prof. Li He. No part of it has previously been submitted for any degree, either at this university or anywhere else.

Acknowledgement

Contents

Nomenclature

Symbol

A	Computational cell face area; Diverging channel height
A_m	Amplitude of oscillation
C	Blade chord
c	Local speed of sound
c_f	Friction coefficient
c_p	Pressure coefficient
e	Fluid internal energy
F	Flux vector in the x direction
G	Flux vector in the θ direction
H	Flux vector in the r direction; Blade height
k	Reduced frequency; Coefficient of heat conductivity
L	Reference length
M	Mach number
N	Blade number; Wave number; Number of perturbations
p	Static pressure
P_0	Total pressure
r	Radius; Radial coordinate
Re	Reynolds number
S	Source term vector; Blade Span; Blade Spacing
T	Temperature; Time
t	Time
t'	Pseudo time
U	Conservative variables vector
u	Velocity in the x direction
u_g	Grid moving velocity in the x direction
u_{ref}	Reference velocity
V	Computational cell volume
v	Velocity in the θ direction

v_g	Grid moving velocity in the θ direction; Blade row rotating speed
w	Velocity in the r direction
w_g	Grid moving velocity in the r direction
x	Axial coordinate
Y_p	Blade pitch; Incoming wake pitch
ϕ	Phase angle
θ	Tangential coordinate
γ	Stagger angle; Specific heat ratio
μ	Kinematic viscosity
ρ	Density
σ	Inter-blade Phase Angle
ω	Angular frequency

Subscript

$-$	Complex conjugate
1	Inlet
l	Laminar
t	Turbulent
x, θ, r	Variables in the x, θ and r directions respectively
exit	Variable at exit
inl	Variable at inlet
ref	Reference quantity
wake	Variable in wake

Superscript

$-$	Time-averaged quantity
$'$	Unsteady perturbation
$\hat{}$	Steady state quantity
$\tilde{}$	Complex amplitude of perturbation
l	Lower
u	Upper

Chapter 1

Introduction

1.1   General Background

Turbomachinery flows are highly complex, three-dimensional and unsteady. New blade designs are becoming more three-dimensional with large amounts of twist and sweep and with very small inter-blade spacing. As the aerodynamic loading increases, the evaluation of unsteady loading and blade stress levels becomes more important in the design process. The aeromechanical behaviour of fans, compressors and turbines is strongly dependent on the unsteady aerodynamic behaviour of the blade rows. Aerodynamics related blade vibration is an undesirable consequence of the unsteady flow process in an axial flow turbomachine that can lead to structural failure of the blading. The vulnerability of turbomachines to vibration is not surprising in view of the large gas loads and the small amount of mechanical damping and the high load at the rotor root arising from the centrifugal loading.

Flutter and forced response are the two categories of aerodynamically induced blade vibrations. Flutter is a dynamic aeroelastic instability, in which the aerodynamic forces that sustain the blade motion are regarded as being solely dependent on that motion. The flow perturbation due to motion of internal boundaries produces the physical mechanism for blade flutter. The blade motion, however, causes unsteady forces to act upon the blade surface, and it is the coupling of these forces with the existing blade mode that results in the phenomenon of blade flutter. It is the phase relationship between the blade motion and the unsteady forces induced that determines the onset of flutter. Given the correct phase relation, the unsteady forces will do work on the blade and flutter will commence. Under other conditions, work will be done by the blade on the surrounding fluid, and damping of the blade vibration will take place. Blade flutter modes can occur in two different ways; the bending mode where the tip of the blade vibrates around the axial direction and the torsion mode where the blade rotates around the spanwise direction. Nevertheless, it is now widely accepted that the turbomachinery blade flutter tends to be a single mode phenomenon, unlike the wing flutter in which bending and torsion modes couple together. The turbomachine blade is much stiffer than the airplane wing since the

1

mass ratio of blade/fluid is considerably larger. The unsteady aerodynamic forces are generally not large enough to significantly alter the natural mode shapes and frequencies of the system at the rotational speed of interest. Therefore, the self-excited vibrations are normally not of the coalescence mode type.

Flutter is primarily seen in fans, front and middle compressor blades, and high aspect ratio low pressure turbine stages. The types of flutter observed in turbomachinery blading are shown on an operating map of a compressor in Fig. 1.1. Flutter in compressors is often comparatively ill defined, occurring at frequencies that are not multiples of engine order and at different places in the operating map of the compressor. Flutter rarely occurs at or near the design point. The most common type is high operating line flutter, which is usually called stall flutter. This is seen in fans and frontal compressor stages. The next most common type of flutter is supersonic unstalled flutter, which is commonly seen in shrouded fans. Choke flutter is a less common, low operating line, type of flutter experienced by middle and rear compressor stages (Kielb, 1999). Flutter sometimes occurs on only a few blades in a row with different amplitudes on the individual blades, but as the amplitude rises the flutter tends to be more coherent to involve all the blades at a common frequency with a fixed phase angle between the motions of adjacent blades.

In forced vibration, the aerodynamic forces that excite the motion are independent of that motion. The circumferential asymmetry in the mean flow gives rise to the forced response of the blading (Sisto, 1977). Flutter can occur over a wide range of operating condition while forced vibration can occur when a periodic aerodynamic excitation, with frequency close to a structural system natural frequency acts on the blades in a given row. Such excitations arise from inlet or exit flow non-uniformities and the aerodynamic interactions that occur between a given blade row and neighbouring blade rows. The flow non-uniformities include variations in total pressure, total temperature and static pressure at inlet and variations in static pressure at the exit. The blade row interactions include potential flow and wake interactions. The potential flow interaction is associated with static pressure variation on a given row from upstream and downstream and wake interaction is the effect on the flow through wakes shed by upstream rows (Verdon, 1993). The potential interaction decays exponentially with an increase in the axial gap between the blade rows, whereas the

wake interaction can propagate several blade rows downstream. For forced vibration almost all the sources must be at harmonics of the rotational frequency of the rotor itself. The Campbell diagram, Fig. 1.2, presents the change in blade vibration frequency as the rotational speed of the machine increases, together with the corresponding engine order frequencies. Integral order vibrations correspond to vibrations when the blade vibration frequency lies close to one of the engine orders. Whether in flutter or forced vibration the blades vibrate in their natural modes at their natural frequencies. The natural frequencies can be changed by changing the design of the blade, but once the blade is made the natural frequencies are essentially fixed parameters for the aerodynamic investigation.

The ability to predict the aeromechanical response of blades arising out of flutter and forced response is critical to further improvement in the performance of turbomachinery and requires a detailed understanding of flows in cascades. Since cascade tests of transonic flows are complicated and very expensive, numerical simulation is a very useful and practical tool to study this phenomenon. The development of computational fluid dynamics has provided an opportunity to formulate these tools. Accurate and efficient aerodynamic analyses are needed to determine the unsteady blade loads for the simulation of nonlinear viscous unsteady flows. There are two different types of analysis namely time domain analysis and frequency domain analysis. The present work is concerned with frequency domain analysis and this will be discussed in detail in the following chapters.

1.2   Aerodynamic Damping

The energy method (Carta, 1967) is widely used to predict flutter boundaries. In this method, the unsteady aerodynamics are calculated for a given vibration mode and the system stability is then determined based on the net energy transfer. Therefore, the prediction of the unsteady flow field around oscillating blades is of essential importance. The most direct global parameter that can be obtained from the unsteady pressure distributions over the entire blade surface is the aerodynamic damping parameter. This represents a measure of system stability, i.e. a system is stable if the aerodynamic damping parameter is greater than zero. Under certain conditions, when the unsteady aerodynamic forces do work on the blade, there will be a net energy

3

input to the blade vibration and flutter will commence. It is usual to assume a periodic blade movement to express the blade perturbation in harmonics, and the blade surface pressure coefficient is expressed as

$$C_P(x,t) = \overline{C_P}(x) \cdot e^{i(\omega t + \phi_P(x))}$$

$$= \left\{ [C_P(x)]_R + i[C_P(x)]_I \right\} e^{i\omega t} \tag{1.1}$$

Physically, the real and imaginary parts are interpreted as the components of the pressure coefficient which are in-phase and out-of-phase respectively with the blade motion defined by

$$h(t) = \overline{h} \cdot e^{i\omega t} ; \alpha(t) = \overline{\alpha} \cdot e^{i\omega t}$$

for bending and pitching motions respectively.

In terms of amplitude and phase angle

$$\overline{C_P}(x) = \sqrt{[C_P(x)]_R^2 + [C_P(x)]_I^2}$$

$$\phi_P(x) = \tan^{-1}\{[C_P(x)]_I / [C_P(x)]_R\}$$

The phase angle ϕ_P is defined as positive when the pressure leads the blade motion.

It should be noted that in computing the blade surface pressure distribution only components, and not amplitudes or phase angles may be differentiated (Carta, 1983).

$$\Delta C_P(x,t) = \left\{ [\Delta C_P(x)]_R + i[\Delta C_P(x)]_I \right\} e^{i\omega t} \tag{1.2}$$

System stability is obtained from a computation of the work per cycle, and its conversion to an aerodynamic damping parameter. The general form of the work coefficient, expressed by the product of force or moment and translation or torsion is given by

$$C_{W,h} = \oint \text{Re}[h(t) \cdot C_h(t)] \cdot \text{Re}[dh(t)]$$

$$C_{W,\alpha} = \oint \text{Re}[\alpha(t) \cdot C_M(t)] \cdot \text{Re}[d\alpha(t)] \tag{1.3}$$

Here, $C_{W,h}$ is defined as the work done on the blade during a pure bending cycle, $C_{W,\alpha}$ as the work done on the blade during a pure pitching cycle. $C_h(t)$ and $C_M(t)$ are force and moment coefficients respectively. Positive work indicates that blade absorbs energy from the flow and the blade vibration will be amplified. From equation (1.3) it is seen that the work coefficient becomes negative for a stable motion that is when the flow extracts energy from the blade vibration. The aerodynamic damping parameter can be expressed as the normalized form of the negative aerodynamic work. The

4

normalized aerodynamic damping coefficient is thus positive when the flow damps the blade vibration.

1.3   Some Relevant Parameters

1.3.1   Reduced Frequency

One of the most important non-dimensional parameters for blade unsteadiness is the reduced frequency, k. Reduced frequency is a measure of unsteadiness and is defined as

$$k = \frac{\omega L}{U} \tag{1.4}$$

where $\omega = 2\pi f$ and f (Hz) is the frequency of unsteadiness, L is a reference length scale and U is a reference velocity usually taken as inlet velocity. For blade flutter problems, L is usually taken to be the blade chord length. For blade row interactions, L is either blade chord length or blade pitch length. The reduced frequency can be interpreted as the ratio of the time taken for a fluid particle to flow past the length of a chord to the time taken for the blade to execute one cycle of vibration. Another interpretation by Platzer and Carta (1988) is given as follows: If an airfoil of chord length L is oscillating at a frequency of $\omega = 2\pi / T$ in a stream moving past it at a velocity V, a sinusoidal wake will be formed which is imbedded in the free stream and hence also moves relative to the airfoil at a velocity V with wavelength $\lambda = VT = 2\pi V / \omega$. If the airfoil chord is divided by this wavelength, we obtain $L / \lambda = L\omega / 2\pi V = k / 2\pi$. At low reduced frequency the wavelength is very large relative to the chord while at high reduced frequency the wavelength is small relative to the chord. Thus the reduced frequency is the ratio of the circumference of a circle of radius L and the wavelength of the wake; the larger the wavelength, the smaller is the k. For the unsteady flow induced by blade oscillation, the time scale of unsteadiness is decided by blade oscillating frequency and the length scale is usually taken to be the blade chord length. For small values of reduced frequency (e.g. $k < 0.1$) the flow is quasi-steady, while for large values, unsteady effects dominate. The value of the reduced frequency is an indicator of the temporal and spatial length scales of unsteadiness. In turbomachinery blade design, the reduced frequency is used as a criterion for avoiding the occurrence of blade flutter. For the unsteady flow induced by blade row interactions, the reduced frequency is normally one order of

magnitude larger than the reduced frequency of the blade flutter. The time scale of unsteadiness in blade row interactions is decided by blade passing frequency and the length scale is decided either by the blade pitch or by the blade chord. Also, reduced frequency is a useful design parameter for preliminary flutter design considerations. For the bending mode, the design value is usually kept higher than 0.4, and for the torsion mode, it is higher than 1.2.

1.3.2 Inter-blade Phase Angle

Inter-blade phase angle is a phase relationship that represents the motion of a blade with respect to other blades. In a well-defined travelling wave mode, all the blades vibrate in the same mode and with the same amplitude but with a phase difference between neighbouring blades. Thus each blade will experience exactly the same motion except at a slightly different time. According to Lane (1956), provided that all blades are identical and equally spaced around the rotor and that linearity holds, the inter-blade phase angle can be defined as

$$\sigma = \frac{2\pi n}{N_b}; \qquad (n = 1, 2, 3, ..., N_b) \qquad (1.5)$$

where n is the wave number or the number of nodal diameters. Therefore, if N_b is the number of blades, then there will be N_b possible values of inter-blade phase angles. The blade flutter will happen at the least stable inter-blade phase angle. A plot of the aerodynamic damping versus the inter-blade phase angle normally provides the least stable inter-blade phase angle. If the pattern of vibratory motion can be broken into its harmonics, each of which is associated with a well-defined mode with an inter-blade phase angle, then the unsteady aerodynamic forces acting on blades at a given set of aero and structural parameters can be defined as the sum of all contributing harmonics. As the phase relationship must add up to 2π (or multiples thereof) as one moves from one blade to another around the rotor, if n represents the wave number in equation (1.5), one could consider the contributing harmonics to contain all integer values of n, leading to as many inter-blade phase angles as the number of blades (Srinivasan, 1997). Carta and St. Hilaire (1980) described the inter-blade phase angle as the most important parameter affecting the stability of oscillating cascaded airfoils. For a single blade passage, the steady flow variables on the upper periodic boundary are identical to those on the lower boundary. For unsteady flows induced by blade

oscillation, the amplitude of flow variables are still identical on both upper and lower periodic boundaries, but there is a phase difference between the upper and lower periodic boundaries. The value of this phase difference is the inter-blade phase angle. Due to the inter-blade phase angle, for an unsteady flow calculation in turbomachinery, a phase-shifted periodic boundary condition can be applied when the calculation is carried out on a single blade passage domain, or the unsteady calculation has to be carried out on a multiple passage domain or on a whole annulus. For multiple passage calculations, the number of passages needed depends on the inter-blade phase angle.

For the blade row interaction, the inter-blade phase angle is decided by the pitch ratio of neighbouring blade rows. For example, for a single compressor stage, let the blade pitch of the reference blade row be Y_{P1} and that of the upstream adjacent blade row be Y_{P2}. Assuming that the upstream blade row is moving at a relative speed ωr with a blade passing frequency f (Hz), the time-lead of the upper blade relative to the lower blade in the reference blade row is:

$$\Delta t = \frac{Y_{P2} - Y_{P1}}{\omega r}$$

The inter-blade phase angle between the upper periodic boundary and lower periodic boundary is

$$\sigma = 2\pi \Delta t f = 2\pi \left(1 - \frac{Y_{P1}}{Y_{P2}} \right) \tag{1.6}$$

Usually, the neighbouring blade rows have differing blade numbers, which results in non-zero inter-blade phase angles. The inter-blade phase angle in wake/rotor or potential/blade row interaction problem can also be worked out by the formulation (1.6).

1.4   Relevance of Three-Dimensional Computation

At present, there are two distinct approaches to the prediction of unsteady turbomachinery flows, the nonlinear time-marching approach in the time domain and the time-linearized approach in the frequency domain. The nonlinear time-marching methods are very useful for research purposes, but are not feasible for design use, probably for some time to come because of the large computing resources required.

The linearized harmonic methods are much more efficient than the fully nonlinear methods. Previous work on linearized method has focussed on the development and application of either two or three dimensional inviscid solvers or two-dimensional viscous solvers. Three-dimensional effects can be important for many reasons. Modern blades can have highly three-dimensional shapes. Many flow features in turbomachines like hub and tip boundary layers, secondary flows, tip vortices etc. limit the region in which the flow can be considered two-dimensional. Transonic flows with strong shocks are highly three-dimensional. In the case of blade vibration, even when the mean flow is two-dimensional, the vibration mode shape of the blade may be three-dimensional. Also, even for simple geometries there is three-dimensional (radial) communication of unsteady flow. Moreover, two dimensional modelling and use of strip theory are known to lead to unreliable prediction of aerodynamic damping (Srinivasan, 1997).

Currently, three-dimensional linerized Euler solvers are beginning to be used in design and three-dimensional Navier-Stokes solvers are under active development. However, the basic linear assumption may prove to be restrictive under transonic and viscous flow conditions. Subsonic stall flutter may involve oscillations of a region of separated flow. Further, the unsteady motion of the shock is a major contributor to the unsteady work (Lindquist and Giles, 1994, Hall et al., 1994). Unsteady flow phenomena such as shock oscillation, viscous layer displacement and separation account for potentially important nonlinear effects. In order to take into account the nonlinear effects, He (1996) developed a nonlinear harmonic method. This method takes advantage of the high computing efficiency of the linear method while including the nonlinear effects of unsteadiness on the time-averaged flows. This method has already been successfully implemented in the two-dimensional Euler and Navier-Stokes solvers (Ning, 1998). The results so far have consistently demonstrated the method's effectiveness (Ning and He, 1998, He and Ning, 1998). Since turbomachinery flows are highly three-dimensional, any practical blading design needs to include three-dimensional effects to make the process a viable tool. Therefore, it is natural to extend the nonlinear harmonic method to three dimensions. As steady three-dimensional viscous solvers in the time domain are still to be used in routine design due to their computational cost, the computationally more efficient

three-dimensional solvers in the frequency domain can be used as a reasonably accurate design method.

1.5   Overview of Thesis

The objective of the present work is the development of three-dimensional Navier-Stokes solver for the prediction of unsteady flow due to blade oscillation, based on both time-linearized method and nonlinear harmonic method, and the validation of the developed method. An important feature of the present work is the use of moving computational grid in three-dimensions for the computation of blade flutter. The need to extrapolate the flow variables from the boundary of the grid to the instantaneous location of the airfoil as done in the case of fixed grid solutions is thereby eliminated.

The next chapter gives an overview of the literature related to computational methods in the time domain as well as frequency domain for unsteady flows arising out of flutter and blade row interaction. Then chapter 3 deals with how nonlinear effects could arise in unsteady flow and how time averaging gives rise to the unsteady stress terms due to nonlinearity. Chapter 4 details the formulation of three-dimensional time-linearized method where the flow is assumed to be composed of a steady part and a perturbation part. Chapter 5 gives the derivation of nonlinear harmonic method in three-dimensions where the flow is assumed to be composed of a time-averaged part and a perturbation part. The time averaging produces extra stress terms similar to the Reynolds stress terms due to nonlinearity. The numerical discretization is similar to that of the time-linearized method. The nonlinear harmonic method solves first order harmonic perturbations. To improve the accuracy of nonlinear prediction higher harmonics should be included and this is achieved through a harmonic balance technique. The formulation of this harmonic balance technique is also presented in this chapter. Chapter 6 presents the two-dimensional results and discussions from computations using time-linearized and nonlinear harmonic methods. The discussions also focus on the extent to which nonlinearity can be predicted using the nonlinear harmonic method. Chapter 7 then presents three-dimensional computational results in the frequency domain for blade oscillation. Finally, Chapter 8 gives conclusions and suggestions for future work.

Chapter 2

Review of Literature

2.1 Computational Methods for Unsteady Flows in Turbomachinery

The application of computational fluid dynamics techniques to the analysis of turbomachinery flows has made an enormous impact on the design of all types of turbomachines and steady flow solvers have now become standard tools in the design of turbomachines. However, because of the unsteady nature of turbomachinery flows, introducing unsteady analysis in the design system is the key to further improve the aerodynamic performance and structural integrity of turbomachines. With the advancement in the computational techniques and availability of computing power, considerable efforts have been made in recent years on the numerical calculation of unsteady flows in turbomachines. Unsteady aerodynamic models must be able to accurately predict unsteady aerodynamic loads arising from blade motion and forced response and these models must be computationally efficient if they are to be a part of useful design system.

A number of Euler and Navier-Stokes procedures have been developed to address flow through single blade rows in which the unsteadiness is caused by blade vibration or by aerodynamic disturbances at the inlet or outlet boundaries and flow through aerodynamically coupled blade rows in which the unsteadiness is caused by relative motion between the blade rows. The unsteady computation can be broadly classified into nonlinear time-marching (time domain) methods and time-linearized (frequency domain) methods. In the recent past, the prediction of unsteady flows in turbomachinery has registered some significant advances in terms of development of efficient linearized analyses. Also, considerable progress has been made in developing a number of Euler and Navier-Stokes procedures for the non-linear time-marching method, where the governing equations are time-accurately time-marched. The nonlinear time-marching method offers improved understanding of unsteady aerodynamic processes, but also requires substantial computational resources. On the other hand, the time-linearized analyses are computationally more efficient and also account for the effects of important design features and operation at transonic Mach

numbers. A comprehensive review of computational methods in the time domain as well as in the frequency domain is provided in this section.

2.2   Nonlinear Time-Marching Method

In the nonlinear time-marching method, the nonlinear unsteady equations are discretized on a computational grid and are time-accurately time-marched until all initial transients have decayed and a periodic state is reached. This approach has the advantage of including flow features like complicated shock structures, large amplitude shock motions and viscous effects like flow separation and shock boundary layer interaction. Therefore, the nonlinear time-marching method has the ability to solve highly nonlinear flows in turbomachinery. However, because of the large number of grid points required and the requirement that the analysis be both time-accurate and stable, the size of the time step will generally be quite small, especially for explicit schemes, making these calculations computationally expensive. In addition, the requirement to compute multiple blade passages as against a single blade passage in the linearized approach makes it prohibitively expensive for routine design use. The main factor is the difficulty in realizing a solution in a single blade-to-blade passage domain. For both blade flutter and rotor/stator interaction problems, periodic unsteadiness would normally be in a circumferentially travelling wave mode. A phase-shifted periodicity can then be assumed. Several phase-shifted periodic condition methods have been proposed to enable solution of a single passage domain. However, these methods are subject to various limitations. Consequently, most of the time-marching computational methods use a multiple passage or the whole annulus domain.

Moretti and Abbett (1966) were the first to use the time-marching method for the calculation transonic flows over blunt bodies. Since then, a large number of numerical schemes based on the concept of time-marching have been developed for steady inviscid and viscous internal and external flows. In the turbomachinery design system, time-marching methods are the most widely used methods for steady flow analysis in isolated and multiple blade row environments. The works of Denton (1983,1992), Dawes (1988) and Ni (1989) are some of the well-known contributions in this regard.

In an unsteady time-marching calculation, the time-domain in which the unsteady or the time-dependent solution is marched has a real meaning. Further, the nonlinearity of the unsteady flow is naturally included in the time-marching unsteady solutions by directly solving the nonlinear Euler/Navier-Stokes equations. For a periodic unsteady flow, such as the unsteady flow induced by blade vibration or blade row interaction, the solution must be advanced through many cycles of transient solution until a periodic solution is reached. Usually, the time-marching unsteady calculation is an order of magnitude more CPU time consuming than its steady counterpart. This is one of the factors that constrain applications of unsteady flow analysis in turbomachinery design. Nevertheless, significant development of time-marching methods for unsteady turbomachinery flows has been made in the last two decades.

2.2.1 Blade Row Interaction

The time-marching unsteady calculations of turbomachinery flows were initially confined to the simulation of blade row interactions. A key constraint to the computational efficiency of the unsteady calculations in turbomachines is the treatment of periodic boundaries. In a steady flow calculation, a direct repeating periodic condition is applied by equating flow variables at the lower and upper periodic boundaries in a single blade-to-blade passage domain. For an unsteady flow calculation of the blade row interaction, the simple periodic boundary condition no longer exists in a single passage calculation due to non zero inter-blade phase angles. One either has to carry out an unsteady calculation on a multiple passage domain which will significantly increase the computation time, or implement a phase-shifted periodic boundary condition in a single passage calculation. As far as computational efficiency is concerned, it is desirable to carry out the calculation in a single passage domain. Therefore, developing phase-shifted periodic condition has played an important role in the development of unsteady time-marching methods in turbomachinery.

The first unsteady flow calculation using the time-marching method in turbomachinery was made by Erdos et al. (1977). In this work, the unsteady flow in a fan stage was calculated by solving the 2D Euler unsteady equations using the McCormack predictor-corrector finite difference scheme in a single passage domain. The phase-shifted periodic condition was implemented using the direct store method.

12

In this method, flow parameters on the periodic boundaries are stored at each time step in one unsteady period to update the solution at the next corresponding period. At every time step, parameters at the boundary are updated by averaging the data obtained at the current step and those stored for a given inter-blade phase angle and also correcting the stored parameters. Koya and Kotake (1985) extended this method to calculate the three-dimensional inviscid unsteady flow through a turbine stage. The disadvantage of this direct store method is the requirement of large computer storage in an unsteady flow calculation. For three-dimensional viscous unsteady calculations, the storage requirements become prohibitive.

Rai (1987) developed a 2-D Navier-Stokes solver for stator/rotor interaction avoiding the phase-shifted periodic condition. The calculations were carried out in a simple stator/rotor pitch ratio by modifying the configuration of the rotor in a turbine stage so that the direct repeating periodic condition could be used in the calculation. The calculated unsteady pressure amplitudes largely depended on how close the stator/rotor pitch ratio used in the calculation correlated to the real pitch ratio. He later extended this technique to calculate three-dimensional viscous calculation of blade row interactions (Rai, 1989).

Giles (1988) used a time-inclined method for implementing the phase-shifted periodic boundary treatment in wake/rotor interaction calculation. In this method, the flow governing equations are first transformed from the physical time domain to a computational time domain. The computational domain is inclined along the blade pitchwise direction according to the time lag between neighbouring blades. In the computational domain, a direct repeating periodic condition can be applied at the upper and lower periodic boundaries in a single blade passage. Giles (1990) also used this technique to calculate blade row interaction in a transonic turbine stage. A computer program UNSFLO was developed by Giles (1993) based on the time-inclined method to handle two-dimensional unsteady problems in turbomachinery such as wake/rotor interaction, potential interaction and flutter. This time-inclined method has its limitations. Domain of dependence restrictions of the governing equations restricts the time-inclination angles of the computational plane. These angles are determined by the pitch ratio of rotor/stator in blade row interaction

problems and the inter-blade phase angle in flutter problems. The restriction becomes severe as the frequency becomes lower.

There have been other efforts to improve the computational efficiency of the time-accurate unsteady calculations in addition to the development of methods for phase-shifted periodic conditions. One approach is to develop efficient time-marching implicit schemes in which a much larger time step can be used compared to the explicit scheme (Rai, 1987). Another approach is to use effective multigrid techniques. He (1993) developed a time-consistent two-grid method which can considerably speed up the convergence of unsteady calculations. In another development, Dorney (1997) proposed a loosely coupled approach by which a reduction in computational effort can be achieved by uncoupling the unsteady interactions between the blade rows. Arnone (1998), in his IGV-rotor interaction analysis in a transonic compressor, used multigrid in an efficient time-accurate integration scheme proposed by Jameson (1991) where a dual time stepping in the physical time domain and a non-physical time domain was introduced. In the physical time marching, an implicit scheme is used. In the non-physical time-marching, any efficient accelerating techniques which are used in steady calculations can be used to speed up the calculation, such as multigrid, local time step, implicit residual smoothing.

Adamczyk (1985, 2000) proposed a notable concept of modelling unsteady effects by solving an average passage Navier-Stokes equation system. In this system, three different averaging methods, namely ensemble-averaging, time-averaging and passage-to-passage averaging were used to average out the unsteady effects due to random flow fluctuations (turbulence) and periodic flow fluctuations (unsteady deterministic flow). This averaging concept transforms the solving of an unsteady problem to solving a set of averaged equations. Any efficient steady flow solver can then solve the averaged equations. But the difficulty in doing this is that the averaging produces unknown deterministic stress terms in the averaged equations due to nonlinearity of the original Euler/Navier-Stokes equations. Extra closure models are required to work out all deterministic stress terms similar to turbulence models for modelling the Reynolds stress terms in the Reynolds averaged Navier-Stokes equations. Hall (1997) addressed the problem of closure for various stress correlation terms in the average passage approach by proposing a simple empirical modelling

14

procedure. Rhie et al. (1998) implemented the concept of deterministic stresses into stator/rotor interface treatment in the blade row interaction problem. In this approach, the deterministic stresses were transferred across the interface of the mixing plane effecting the continuous nature of all parameters across the interface.

2.2.2 Flutter

The treatment of boundary conditions is also a difficulty in unsteady flow calculation for blade flutter analysis. For a non zero inter-blade phase angle, phase shifted periodic boundary conditions have to be applied if the unsteady calculation are carried out in a single blade passage domain. The requirement of computational efficiency is more important in flutter analysis as it involves a large number of repeated calculations.

Gerolymos (1988) modelled two-dimensional Euler equations to calculate unsteady flows in oscillating cascades using the direct store method. This time-marching scheme was later extended to model three-dimensional unsteady Euler equations (Gerolymos, 1993). A two-dimensional Euler solver was developed by He (1990) for unsteady flows around oscillating blades. In this work, the phase-shifted periodic boundary condition was applied using a shape correction method. The unsteady flow variables on the periodic boundaries were transformed into Fourier components by using a Fourier transformation. Compared with the direct store method, the computer storage is greatly reduced by only storing the Fourier coefficients. Since all the phase-shifted methods could deal only with problems with a single perturbation, He (1992) developed the generalized shape correction method for multiple perturbations. He (1994) later extended the 2D method to a three-dimensional time-marching method for inviscid and viscous unsteady flows around oscillating blades. Abhari and Giles (1997) computed unsteady flow around oscillating airfoils in a cascade using a quasi-three-dimensional, unsteady Navier-Stokes solver. They observed that for a transonic compressor case, the nondimensional aerodynamic damping was influenced by the amplitude of the oscillation. Gruber and Carstens (1998) have computed unsteady transonic flows in oscillating turbine cascade using two-dimensional Reynolds averaged Navier-Stokes equations to include viscous effects. Ayer and Verdon (1998) validated a nonlinear time-marching method using two-dimensional unsteady Navier-Stokes equations for subsonic and transonic unsteady flows through vibrating

cascades. They observed that for subsonic flows the unsteady surface pressure responses were essentially linear and for unsteady transonic flows, shocks and their motions caused significant nonlinear contributions to the local unsteady response. It was further shown that viscous displacement effects tend to diminish shock strength and impulsive unsteady shock loads. Isomura and Giles (1998) studied flutter in a transonic fan using quasi three-dimensional thin shear layer Navier-Stokes equations. They have found that the source of flutter is not stall but the shock oscillation of the passage shock near the blade's leading edge on the pressure surface. Further, the unsteady blade surface pressure on the pressure surface generated by the foot of the passage shock wave becomes a dominant source of aerodynamic excitation. They have also observed that once the flutter starts the blade surface pressure on the suction surface has a damping effect and if the the shock wave is fully detached then the flutter may not occur. Recently, Bell and He (2000) investigated the aerodynamic response of a turbine blade oscillating in a bending mode using three-dimensional nonlinear Euler method and compared the results with their experimental data to find good agreement for the full range of reduced frequency tested. The numerical and experimental results also showed a predominantly linear behaviour of the unsteady aerodynamics.

The blade flutter problem is also approached from the aspect of fluid structure interaction, and nonlinear time-marching methods are used by many researchers for developing coupling methods for blade flutter analysis (He, 1994, Marshall and Imregun, 1996, Carstens and Belz, 2000). In the coupling method, the nonlinear aerodynamic equations and the structural equations are solved by time-marching schemes with data being transferred between the aerodynamic model and the structural model at each time step. For the aerodynamic model, the temporal changes of flow variables depend on the blade vibrating velocities and for the structural dynamic model the temporal changes of blade vibrating velocities depend on the instantaneous aerodynamic forces and moments determined by the flow variables. The inter-blade phase angle at which the instability occurs is a part of the solution; therefore the calculations are normally carried out on a multiple passage domain or on a whole annulus. The drawback of the coupling methods is the computational cost, not only due to nonlinear time-marching but also due to the coupling between aerodynamic and structural dynamic models.

Hah et al. (1998) investigated the effects of circumferential distortion in inlet total pressure on the flow field in a transonic compressor rotor by solving steady and unsteady forms of the three-dimensional Reynolds-averaged Navier-Stokes equations. The flow field was also studied experimentally and the experimental measurements and numerical analysis were found to be highly complementary because of the extreme complexity of the flow field. At a high rotor speed where the flow is transonic, the passage shock was found to oscillate by as much as 20 percent of the blade chord, and very strong interactions between the unsteady passage shock and the blade boundary layer were observed.

The nonlinear time-marching method has provided a significant physical understanding of the unsteady flow phenomenon in turbomachines, especially flows with strong nonlinearity, despite its drawback in the form of high computational cost. In addition, the time-marching method provides reliable results for validation of other numerical methods.

2.3   Time-Linearized Harmonic Method

Time-linearized harmonic methods are the result of efforts to find a computationally simpler alternative to the nonlinear time-marching methods and are widely used for unsteady flows in turbomachinery. In the time-linearized approach, the unsteady flow is approximated as the sum of a mean or steady flow and a small perturbation linear unsteady flow. The small perturbation assumption is valid for flows where the unsteady perturbations are less than about 10% of the flow. The nonlinear time-dependent equations are linearized about the steady solution to obtain the linearized unsteady equations. These equations are linear with variable coefficients and describe the small disturbance behaviour of the flow. The variable coefficients are a function of the mean flow field. Since many unsteady flows of interest are periodic in time, the unsteady flow is assumed to be harmonic in time. Under this assumption, the explicit time dependency is eliminated from the unsteady problem. As with steady solvers, the unsteady flow is computed in a single blade passage. The validity of these methods depends on the linearity of the unsteady flow problems. Over the years, it has been

17

shown by many researchers that in many cases of turbomachinery unsteadiness the time-linearized methods are adequate to model the flow phenomenon.

Initially, time-linarized approaches were made using the potential flow model. (Verdon and Casper, 1982 and 1984, Whitehead, 1987) The time-linearized models were developed for two-dimensional potential flow in cascades. The governing equations were obtained by linearizing the full potential equations about a mean flow resulting in the linearized unsteady potential perturbation equations. Because of the assumption of isentropic and irrotational flow, these potential analyses cannot be used to model unsteady flows with strong shocks.

The linearized Euler analysis was first introduced by Ni and Sisto (1976). They used a pseudotime time-marching technique to solve the linearized harmonic Euler equations. Hall and Crawley (1989) later developed a direct method of solving the linearized Euler equations and applied the work to subsonic cascade geometries and transonic channel flows. In their work, the steady flow solution was obtained by solving the steady Euler equations by the Newton iteration technique and the linearized harmonic Euler equations were solved by a finite volume operator similar to the one used by Ni (1982). A shock fitting technique was used to handle shock waves in transonic flow. However, shock fitting techniques are not practical due to complex shock systems in turbomachinery flows. It is therefore preferable to use shock capturing techniques. Lindquist and Giles (1994) have showed that it is possible to use shock capturing in time-linearized Euler method to predict blade unsteady loading correctly provided the time-marching scheme is conservative and the steady shock is sufficiently smeared. In order to consider three-dimensional effects, Hall and Lorence (1993) developed a fully three-dimensional linearized Euler analysis for unsteady flows to predict flutter and forced response. The three-dimensional Euler equations in rotating frame of reference were solved using the pseudo time-marching technique originally suggested by Ni and Sisto (1976). Hall et al. (1994) extended the above method for transonic flows in turbomachines where shock capturing was used to model the shock impulse (the unsteady load due to harmonic motion of the shock). Marshall and Giles (1997) have also applied the fully three-dimensional linearized Euler analysis for flutter and forced response.

The next step is the extension of Euler methods to Reynolds-averaged Navier-Stokes equations (Holmes and Lorence, 1997). The Navier-Stokes methods are more realistic for flutter analysis, especially for subsonic stall flutter prediction in which the oscillation of the flow separation region is the dominant phenomenon. Another aspect of interest is the interaction from adjacent blade rows. Silkowski and Hall (1998) have shown that the aerodynamic damping of a blade row that is part of a multistage machine can be significantly different from that predicted using an isolated blade row model. Further, Clark and Hall (2000) have applied the time-linearized Navier-Stokes analysis to predict both low-incidence flutter and high-incidence flutter at low speed in two-dimensional cascades. Their results show that the time-lineraized analysis is able to model accurately the unsteady aerodynamics associated with turbomachinery stall flutter. Chassaing and Gerolymos (2000) have used time-linearized analysis, based on linearization of an upwind scheme for convective fluxes, for compressor flutter analysis to compute three-dimensional Navier-Stokes equations and showed that computationally the time-linearized method is more than one order of magnitude faster than nonlinear time-marching method.

The time-linearized harmonic solvers are computationally efficient using linearized techniques while still modelling the dominant flow physics. Since linearization converts a nonlinear unsteady equation into a steady flow equation and a linearized perturbation equation, any well-developed time-marching techniques applicable for steady flow solutions can be used by introducing a pseudo-time technique. Moreover, the calculation can be performed in a single blade passage domain as application of the phase-shifted periodic condition becomes easier due to the harmonic assumption. However, the validity of time-linearized analysis is limited to flows in which nonlinear effects arising from complex flow conditions like shock oscillations, finite amplitude excitation, flow separation etc. do not play a role.

2.4   Nonlinear Harmonic Method

Considering the computational efficiency of the time-linearized method and the ability of the nonlinear time-marching method to predict nonlinear effects of unsteady flows, it is highly desirable to develop a method that has high computational

efficiency like the time-linearized method and which can also account for nonlinear effects like the nonlinear time-marching method.

As mentioned earlier, Adamczyk (1985,2000) showed that time averaging the Navier-Stokes equations resulted in the inclusion of the effect of the deterministic periodic unsteadiness on the mean flow through stress terms similar to the Reynolds stress terms. Giles (1992) combined the idea of Adamczyk with linear unsteady flow modelling to formulate an asymptotic approach in which the level of unsteadiness was the small asymptotic parameter. Unsteady flow was calculated using the linearized form of the unsteady Euler equations assuming that its magnitude was sufficiently small. Changes to the nonlinear steady flow field due to the time-averaged effect of the linear unsteadiness were introduced through the inclusion of quadratic source terms. He (1996) proposed a nonlinear harmonic methodology in which the extra stress terms in the time-averaged equations due to nonlinearity were solved simultaneously with the harmonic perturbation terms in a strongly coupled approach.

In the nonlinear harmonic approach, the time-averaged flow, instead of steady flow, is used as the basis for unsteady perturbations. The nonlinear effects are included in a coupled solution between time-averaged flow and unsteady perturbations. To illustrate this approach in a simple way, a one-dimensional convection model equation is used here:

$$\frac{\partial u}{\partial t} + \frac{1}{2}\frac{\partial uu}{\partial x} = 0 \tag{2.1}$$

The time-dependent flow variable in the above equation is composed by

$$u(x,t) = \overline{u}(x) + u'(x,t) \tag{2.2}$$

where $\overline{u}$ is the time-averaghed quantity and u' is a periodic unsteady perturbation. Substituting equation (2.2) into equation (2.1), we have

$$\frac{\partial u'}{\partial t} + \frac{1}{2}\frac{\partial}{\partial x}(\overline{uu} + 2\overline{u}u' + u'u') = 0 \tag{2.3}$$

The time-averaged equation is obtained from time-averaging equation (2.3)

$$\frac{\partial \overline{uu}}{\partial x} + \frac{\partial}{\partial x}(\overline{u'u'}) = 0 \tag{2.4}$$

20

Comparing equation (2.1) and (2.4), it is evident that time-averaging has generated an extra term in the time-averaged equation (2.4). This extra term $\frac{\partial}{\partial x}(\overline{u'u'})$ is a nonlinear term that is similar to the turbulence (Reynolds) stress terms.

The unsteady perturbation equation can be obtained by the difference between the basic unsteady flow equation (2.1) and the time-averaged equation (2.4),

$$\frac{\partial u'}{\partial t} + \frac{1}{2}\frac{\partial}{\partial x}(2\bar{u}u' + u'u' - \overline{u'u'}) = 0 \tag{2.5}$$

However, equation (2.5) is not readily solvable if a frequency domain approach is to be used. It is assumed that the unsteady perturbation is dominated by first order terms. Neglecting second order terms, the resultant first order equation is given by

$$\frac{\partial u'}{\partial t} + \frac{\partial}{\partial x}(\bar{u}u') = 0 \tag{2.6}$$

The unsteady perturbation equation (2.6) is of the same form as the perturbation equation in the time-linearized method. However, equation (2.6) is no longer linear because the time-averaged variable $\bar{u}$ is unknown, which in turn depends on the unsteady perturbation. Due to the interaction between the time-averaged and the unsteady perturbation equations, the nonlinear effects due to the unsteadiness can be included in a time-averaged flow and unsteady perturbation coupled solution.

The nonlinear harmonic method has already been shown to predict flow unsteadiness due to blade flutter with improvement over conventional methods for two-dimensional cases (Ning and He, 1998; He and Ning, 1998). Chen et al (2001) have shown that this method is more efficient than the conventional nonlinear time-domain methods in modelling the three-dimensional unsteady blade row interaction effects. In this paper, the rotor/stator interface treatment follows a flux-averaged characteristic based mixing plane approach and includes the deterministic stress terms due to upstream running potential disturbances and downstream running wakes, resulting in the continuous nature of all parameters across the interface. At the inlet to the downstream row, incoming wake perturbations, in terms of velocities, pressure and density are produced by a spatial Fourier transform of the time-averaged non-uniform field of the outlet from the upstream row. At the outlet from the upstream row, upstream running potential disturbances can be produced by a spatial Fourier transform of the time-averaged non-uniform field at the inlet to the downstream row.

Hall et al (2002) proposed a harmonic balance technique for modelling unsteady nonlinear flows in turbomachinery. This technique enables the inclusion of harmonic perturbations of order higher than one. Since many unsteady flows of interest in turbomachinery are periodic in time, the unsteady flow conservation variables can be represented by a Fourier series in time with spatially varying coefficients leading to a harmonic balance form of the Euler or Navier-Stokes equations. These equations are then solved using efficient computational techniques like pseudo-time time-marching with local time stepping and multigrid acceleration. The original form of the harmonic balance equations outlined in this paper is quite complex and to overcome this, the Fourier coefficients are reconstructed at 2N+1 equally spaced points in time over one temporal period, where N being the number of harmonics.

Recently, He (2001) proposed to include higher order harmonics in the nonlinear harmonic method using the harmonic balance technique in a simple approach and the details of this method are provided in chapter 5. The results show that though the inclusion of higher harmonics improved the prediction of nonlinearity, for highly nonlinear flows, the prediction capability of the method has some shortcomings. These are discussed in chapter 6.

A comprehensive review of computation of unsteady flows in time domain as well as in frequency domain has been presented. Since the present work is concerned with three-dimensional computation in the frequency domain the following chapters will deal with the detailed derivation of time-linearized harmonic method and nonlinear harmonic method followed by computational results and discussions.

Chapter 3

Unsteadiness and Flow Nonlinearity

3.1 Unsteady Flow and the Concept of Averaging

As discussed in chapter 2, many researchers have so far developed numerical methods for calculating nonlinear unsteady flows. These codes have been of great help in terms of understanding and investigating the unsteady flow phenomena in turbomachinery. However, despite the capabilities of these nonlinear time-marching methods, they could not be used as regular design tools in industrial applications due to the high computational cost associated with these codes. This becomes acute especially in multi-stage calculations. Therefore, the quest is to perform the turbomachinery flow calculation that includes the unsteady effects in the best possible way. In the process, it is pertinent to focus on the importance of unsteady effects in such predictions.

The flow field in multistage compressors and turbines is extremely unsteady with frequencies ranging from a fraction of shaft speed to several times that of the highest blade passing frequency. The length scales also vary considerably from the whole circumference to a fraction of the blade chord. With such vast time and length scales, it is easier to describe the flow with appropriately averaged set of equations that deal with particular unsteadiness of interest instead of attempting to directly simulate the entire set of nonlinear unsteady equations. Basically, the averaged set of equations governs the underlying mean velocity field while including the effect of unsteadiness on the steady flow. The unsteadiness in turbomachinery flows includes both random unsteadiness and periodic unsteadiness. The random fluctuations are characterised by turbulence. The Reynolds-averaged modelling of turbulent flows is an example of modelling complex unsteadiness using averaged set of equations. The Reynolds-averaging of unsteady Navier-Stokes equations decouples the random disturbances from deterministic periodic unsteadiness. The fluctuating field depends in a nonlinear fashion on the mean velocity distribution, which in turn is governed by these Reynolds averaged equations. The Reynolds stresses arising out of this averaging process contain the fluctuating velocities and need closure in the form of turbulence models. It is therefore essential to understand how the averaging process produces these stress terms due to nonlinearity of the unsteady flow equations and makes these

averaged set of equations different from the steady (mean) flow equations. The following sections demonstrate how this approach can be used, first to resolve the random fluctuations that account for turbulence and then to resolve the deterministic periodic unsteadiness and the associated nonlinear effects on the mean flow.

3.1.1 Random Unsteadiness and Reynolds Averaging

The instabilities in a turbulent flow are related to the interaction of viscous terms and nonlinear inertia terms in the equations of motion. This interaction is very complex because it is rotational, fully three-dimensional and time dependent. Randomness and nonlinearity combine to make the equations of turbulence very intractable. Therefore, before attempting to solve the fluid flow momentum and energy equations, there exists the question of resolving the consistency between the random nature of turbulent flows, and the deterministic nature of classical mechanics embodied in the Navier-Stokes equations. According to Newton's principle of determinism, if the initial positions and velocities are known, for a given time t_0, at all scales, then there exists only one possible state for the flow at any time $t > t_0$. Theoretically, it may seem impossible to consider the deterministic evolution of a given turbulent flow for arbitrary times, starting with a given field of initial conditions. Although the fluid turbulence evolves with time in a complicated way due to the nonlinear interactions, with a well-defined set of partial differential equations subject to well-defined boundary and initial conditions, suitably large and powerful computers should be able to solve the equations numerically. However, at higher Reynolds numbers, the simulations generally only deal with large scales of flow, and contain errors due to the lack of detail concerning the initial and boundary conditions in addition to the inaccuracy of the numerical schemes. These errors are amplified by the nonlinearities of the equations and after a period of time the predicted turbulent flow will differ significantly from the actual field. These large eddy simulations (LES) generally predict only the shape of the large structures existing in the flow.

On the other hand, it is also very useful to employ statistical tools and consider the various fluctuating quantities as random functions and try to model the evolution of averaged quantities of flow. The idea is to decompose a turbulent velocity field into a mean and a fluctuating part in an attempt to extract the relevant mean physical

quantities. The averaged set of equations is derived starting from the Navier-Stokes equations that govern the underlying turbulent velocity field. The most basic of these averaged equations are those that govern the mean velocity field. Since direct numerical simulation is still an expensive proposition in terms of computational effort, the averaging approach provides the necessary tool wherein the determination of the solution of the Navier-Stokes equations is achieved by formulating averaged flow equations based on the mean flow field.

The incompressible momentum (N-S) equation is given by

$$\frac{\partial u_i}{\partial t} + u_j \frac{\partial u_i}{\partial x_j} = -\frac{1}{\rho}\frac{\partial p}{\partial x_i} + \upsilon \frac{\partial^2 u_i}{\partial x_j \partial x_j} \tag{3.1}$$

Now, assuming that the velocity field is decomposed into a time-averaged (mean) value and a random fluctuation, it can be expressed as

$$u_i(x,t) = \overline{u_i(x)} + u_i'(x,t) \tag{3.2}$$

The decomposition of the velocity into its mean and fluctuation is called Reynolds decomposition. The averaging of the flow equations can be carried out in different ways but if the intention is to study the underlying steady flow then the method of time averaging is the most commonly used one.

The time averaging operation is defined as

$$\overline{u_i(x)} = \frac{1}{T}\int_{t_0}^{t_0+T} u_i(x,t)dt \tag{3.3}$$

The average of a fluctuating quantity is zero by definition:

$$\overline{u_i'(x,t)} = \frac{1}{T}\int_{t_0}^{t_0+T}\left[u_i(x,t) - \overline{u_i(x)}\right]dt = 0 \tag{3.4}$$

The average of products is computed in the following way:

$$\overline{u_i u_j} = \overline{(\overline{u_i} + u_i')(\overline{u_j} + u_j')}$$

$$= \overline{\overline{u_i}\,\overline{u_j} + u_i'\overline{u_j} + u_j'\overline{u_i} + u_i'u_j'}$$

$$= \overline{u_i}\,\overline{u_j} + \overline{u_i'u_j'} \tag{3.5}$$

For a time average to make sense, the integrals in (3.3) and (3.4) have to be

intepdendent of t_0. It then follows that the mean flow has to be steady, i.e. $\dfrac{\partial \overline{u_i}}{\partial t} = 0$.

Without this constraint (3.3) and (3.4) would be meaningless. The averaging time T
needed to measure mean values is large compared to the time scale of fluctuations and
the actual value depends on the accuracy desired. If we are interested in periodic or
transient behaviour of an unsteady flow, an ensemble averaging process is usually
resorted to in the place of time-averaging so that the averaged quantity still remains
time dependent. There is no loss of generality however as expressions (3.4) and (3.5)
are valid for all kinds of averaging. In order to simplify the time-averaging process,
equation (3.1) is written in conservative form;

$$\frac{\partial u_i}{\partial t} + \frac{\partial}{\partial x_j}(u_i u_j) = -\frac{1}{\rho}\frac{\partial p}{\partial x_i} + \upsilon \frac{\partial^2 u_i}{\partial x_j \partial x_j} \tag{3.6}$$

Substituting the Reynolds decomposition (3.2) in the momentum equation (3.6) and
time averaging it, we get

$$\frac{\partial}{\partial x_j}(\overline{u_i u_j} + \overline{u_i' u_j'}) = -\frac{1}{\rho}\frac{\partial \overline{p}}{\partial x_i} + \upsilon \frac{\partial^2 \overline{u_i}}{\partial x_j \partial x_j} \tag{3.7}$$

Since mass conservation holds for time-averaged flow, utilising the continuity

condition $\dfrac{\partial \overline{u_i}}{\partial x_i} = 0$ the above equation becomes

$$\overline{u_j}\frac{\partial \overline{u_i}}{\partial x_j} + \frac{\partial}{\partial x_j}(\overline{u_i' u_j'}) = -\frac{1}{\rho}\frac{\partial \overline{p}}{\partial x_i} + \upsilon \frac{\partial^2 \overline{u_i}}{\partial x_j \partial x_j} \tag{3.8}$$

In equation (3.8), aside from replacement of instantaneous variables by mean values,
time-averaging has brought about the appearance of the term $\overline{u_i' u_j'}$ due to nonlinearity
of the convection terms. Because a momentum flux is related to a force by Newton's
second law, the turbulent transport term may be thought of as the divergence of a
stress. Because of the Reynolds decomposition that represents the instantaneous flow
as a combination of mean and fluctuation, the turbulent motion can be perceived as an
agency that produces stresses in the mean flow. Therefore, this term $\overline{u_i' u_j'}$ is called the
Reynolds stress term. Rewriting equation (3.8) by placing the Reynolds stresses along
with the viscous stresses, we have

$$\overline{u_j} \frac{\partial \overline{u_i}}{\partial x_j} = -\frac{1}{\rho} \frac{\partial \overline{p}}{\partial x_i} + \frac{1}{\rho} \frac{\partial \overline{\tau_{ij}}}{\partial x_j} \qquad (3.9)$$

where $\overline{\tau_{ij}} = \mu \left(\frac{\partial \overline{u_i}}{\partial x_j} + \frac{\partial \overline{u_j}}{\partial x_i} \right) - \overline{\rho u_i' u_j'}$

The Reynolds stresses are written in Eq. (3.9) on the right side of the equation to reflect their contribution to the forces acting on a fluid element, but they arise from the nonlinearity of the convection terms on the left side. While the viscous stresses stem from momentum transfer at the molecular level, the Reynolds stresses stem from momentum transfer by the fluctuating velocity field. The Navier-Stokes equations thus modified after Reynolds averaging are called Reynolds averaged Navier-Stokes equations. The Reynolds averaged Navier-Stokes equations, therefore, represent an unsteady deterministic flow field. The effects of turbulence on this flow field are accounted for by means of the Reynolds stresses. Thus the application of time averaging has resulted in the transformation of the original random turbulent flow field into that of a deterministic flow, and the decomposition of the flow into a time-averaged flow and random velocity fluctuations has isolated the effects of turbulence on the time-averaged flow.

3.2   Nonlinearity in Deterministic Unsteady Flow

In turbomachinery flows, in addition to the random disturbances, the coherent blade-to-blade unsteady flow structure gives rise to deterministic periodic unsteadiness. Figure 3.1 illustrates a typical unsteady velocity distribution that includes both random and periodic unsteadiness. Reynolds averaging such a flow separates the random unsteadiness associated with turbulence from deterministic periodic unsteadiness. Once the random disturbances are taken care of, we are left only with the problem of tackling the periodic unsteadiness.

In numerical simulation of turbomachinery unsteady flows, the nonlinear time-marching method in the time-domain is capable of resolving the nonlinearity arising from periodic unsteadiness, as the equations are not constrained by any major assumptions. On the other hand, in the case of time-linearized frequency domain approach the linear assumption eliminates the nonlinear effects arising out of periodic

27

unsteadiness. However, there should be ways to include nonlinear effects due to periodic disturbances in a frequency domain approach. According to Adamczyk (1985,2000), the unsteady components of the flow are important only in as much as they change the mean flow. In his passage-averaged equation system, he includes the effect of deterministic periodic unsteadiness on the mean flow through terms that are similar in nature to the Reynolds stresses in the Reynolds–averaging of turbulent flow equations. Adamczyk showed that time averaging a three-dimensional unsteady equation system results in an equation system with deterministic stress terms from periodic unsteadiness. If nonlinear effects are significant, the time-averaged flow will be different from the steady flow. Therefore, if time averaging can be incorporated in the frequency domain approach, it should be possible to predict nonlinear unsteady effects that affect the mean flow.

3.2.1 Time Averaging and Deterministic Stresses

The unsteady Reynolds averaged Navier-Stokes equations are:

$$\frac{\partial u_i}{\partial t} + u_j \frac{\partial u_i}{\partial x_j} = -\frac{1}{\rho} \frac{\partial p}{\partial x_i} + \frac{1}{\rho} \frac{\partial \tau_{ij}}{\partial x_j} \tag{3.10}$$

The unsteady velocity field in the above equation is deterministic, as the Reynolds averaging has already decoupled the random fluctuations. For a steady flow, equation (3.10) will become

$$u_j \frac{\partial u_i}{\partial x_j} = -\frac{1}{\rho} \frac{\partial p}{\partial x_i} + \frac{1}{\rho} \frac{\partial \tau_{ij}}{\partial x_j} \tag{3.11}$$

The unsteady deterministic variable in Eq. (3.10) can be decomposed into a time-averaged part and a fluctuating unsteady part

$$u_i(x,t) = \overline{u_i(x)} + \tilde{u}_i(x,t) \tag{3.12}$$

The time averaging operator is the same as in (3.3) except that T is the time of one period in the case of periodically unsteady flows. Substituting Eq. (3.12) into Eq. (3.10) and time averaging it, we get

$$\overline{u_j} \frac{\partial \overline{u_i}}{\partial x_j} + \frac{\partial}{\partial x_j}(\overline{\tilde{u}_i \tilde{u}_j}) = -\frac{1}{\rho} \frac{\partial \overline{p}}{\partial x_i} + \frac{1}{\rho} \frac{\partial \overline{\tau_{ij}}}{\partial x_j} \tag{3.13}$$

Comparing the time-averaged equation (3.13) with the steady flow equation (3.11), it is seen that time averaging of a periodically unsteady flow results in an extra term $\overline{\tilde{u_i}\tilde{u_j}}$ due to nonlinearity of the equation. Since this extra term has been generated in the same fashion as the Reynolds stress term, it can be termed as unsteady deterministic stress. Since the deterministic stress is a correlation of fluctuating quantities that depend in a nonlinear fashion on the steady flow, if nonlinear effect is significant then the corresponding time-averaged flow should be significantly different from the steady flow. Therefore, the extent of nonlinearity of a periodically disturbed unsteady flow can be illustrated by the difference between a time-averaged flow and a steady flow. In this context, it should be mentioned that in the case of a time-linearized model or a linear flow response, a time-averaged flow would have to be the same as a steady one.

The effect of the extra nonlinear term in the time-averaged equation depends on the spatial gradient and not just the magnitude of the unsteady perturbation. In the case of random disturbance (i.e. turbulence) in a time-mean flow, where the Reynolds stresses are generated in the same fundamental mechanism by nonlinearity, the turbulent fluctuations are normally much smaller in comparison to the time-mean flow quantities, but their effect on the mean flow can be significant at certain conditions. Therefore, the nonlinear effects cannot be easily neglected simply because the unsteadiness under consideration is of a small magnitude. The variation of the nonlinear term in space in terms of its phase and amplitude matters more than just its magnitude.

The extent of nonlinearity in an unsteady flow can also be indicated by different harmonics, compared to the periodically varying disturbances specified at boundaries (He, 1999). On the other hand, a linear response will be in the same harmonic form as that of the boundary disturbance. This can be illustrated by considering the motion of a blade subject to sinusoidal oscillation, given by

$$x = A_x \sin(\omega t) \tag{3.14}$$

where A_x is the amplitude of the blade vibration. The response of the unsteady flow to the blade oscillation can be considered linear, if the unsteady flow parameters also vary in a sinusoidal form. Therefore, the fluctuating velocity can be expressed by

$$\tilde{u} = A_u \sin(\omega t + \phi) \tag{3.15}$$

where A_u is the amplitude of the velocity fluctuation and ϕ is the relative phase angle between the velocity and the blade oscillation. However, if the unsteady flow response is nonlinear, the nonlinear product term becomes

$$\tilde{u}\tilde{u} = A_u^2 \sin^2(\omega t + \phi) = \frac{A_u^2}{2}\left[1 - \cos(2\omega t + 2\phi)\right] \tag{3.16}$$

From the above expression it is evident that nonlinearity is responsible for the creation of a second harmonic component from the first harmonics, in addition to a steady part. Thus, the appearance of second or higher harmonic components in a system subject to only first harmonic disturbances at the boundaries is an indication of the extent of nonlinearity. For flows with strong nonlinear effects the magnitude of the second harmonic disturbances will be comparable to that of the first order harmonic disturbances and even disturbances of third and higher order would also not be very insignificant.

The nonlinear harmonic method, as mentioned in the previous chapter, makes use of the concept of time-averaging as explained above to include nonlinear effects in a frequency domain analysis. The extra unsteady stress terms resulting from time-averaging include nonlinear unsteady flow effects on the mean flow. The detailed derivation of the nonlinear harmonic method is presented in chapter 5. Thus the inclusion of nonlinearity through time-averaging makes it possible for a linearized approach to predict in a computationally efficient way unsteady nonlinear flow features that are otherwise possible only through nonlinear time-marching methods. This enables the frequency domain analysis to be used as an efficient tool in the turbomachinery design process.

Chapter 4

Linear Harmonic Method

4.1 Governing Equations

The basic laws of fluid dynamics are conservation laws that express the conservation of mass, momentum and energy in a volume closed by a surface. Only with the supplementary requirement of sufficient regularity of solution can these laws be converted into partial differential equations. In case discontinuities such as shocks occur, the solution of the differential equations is to be interpreted in a weak form, i.e. as a solution of the integral form of the equations. In such cases, it is extremely important that the conservation laws in their integral form are represented accurately. The most natural method to accomplish this is to discretize the integral form of the equations and not the differential form. The finite volume method is then the appropriate choice for discretization.

The governing equations in the present case are three-dimensional Reynolds averaged unsteady Navier-Stokes equations in cylindrical coordinates (x, θ, r) in an absolute frame of reference. The integral form of the three-dimensional Navier-Stokes equations over a moving finite volume ΔV is

$$\frac{\partial}{\partial t} \iiint_{\Delta V} U dV + \oiint_A \left[(F - F_V)\vec{n_x} + (G - G_V)\vec{n_\theta} + (H - H_V)\vec{n_r} \right] dA = \iiint_{\Delta V} S dV$$

(4.1)

where

$$U = \begin{pmatrix} \rho \\ \rho u \\ \rho v \\ \rho w \\ \rho e \end{pmatrix} ; F = \begin{pmatrix} \rho u - \rho u_g \\ \rho uu + p - \rho uu_g \\ r(\rho uv - \rho vu_g) \\ \rho uw - \rho wu_g \\ (\rho e + p)u - \rho eu_g \end{pmatrix} ; G = \begin{pmatrix} \rho v - \rho v_g \\ \rho uv - \rho uv_g \\ r(\rho vv + p - \rho vv_g) \\ \rho vw - \rho wv_g \\ (\rho e + p)v - \rho ev_g \end{pmatrix} ; H = \begin{pmatrix} \rho w - \rho w_g \\ \rho uw - \rho uw_g \\ r(\rho vw - \rho vw_g) \\ \rho ww + p - \rho ww_g \\ (\rho e + p)w - \rho ew_g \end{pmatrix}$$

$$F_V = \begin{pmatrix} 0 \\ \tau_{xx} \\ r\tau_{x\theta} \\ \tau_{xr} \\ u\tau_{xx} + v\tau_{x\theta} + w\tau_{xr} - q_x \end{pmatrix} ; G_V = \begin{pmatrix} 0 \\ \tau_{\theta x} \\ r\tau_{\theta\theta} \\ \tau_{\theta r} \\ u\tau_{\theta x} + v\tau_{\theta\theta} + w\tau_{\theta r} - q_\theta \end{pmatrix} ; H_V = \begin{pmatrix} 0 \\ \tau_{rx} \\ r\tau_{r\theta} \\ \tau_{rr} \\ u\tau_{rx} + v\tau_{r\theta} + w\tau_{rr} - q_r \end{pmatrix}$$

31

and

$$S = \begin{pmatrix} 0 \\ 0 \\ 0 \\ \rho v^2/r \\ 0 \end{pmatrix} \qquad \tau_{xx} = \frac{2}{3}\mu\left[2\frac{\partial u}{\partial x} - \frac{\partial w}{\partial r} - \frac{1}{r}\frac{\partial v}{\partial \theta}\right] - \rho\overline{u'u'}$$

$$\tau_{\theta\theta} = \frac{2}{3}\mu\left[2\frac{1}{r}\frac{\partial v}{\partial \theta} - \frac{\partial u}{\partial x} - \frac{\partial w}{\partial r}\right] - \rho\overline{v'v'} \qquad \tau_{rr} = \frac{2}{3}\mu\left[2\frac{\partial w}{\partial r} - \frac{1}{r}\frac{\partial v}{\partial \theta} - \frac{\partial u}{\partial x}\right] - \rho\overline{w'w'}$$

$$\tau_{x\theta} = \tau_{\theta x} = \mu\left[\frac{\partial v}{\partial x} + \frac{1}{r}\frac{\partial u}{\partial \theta}\right] - \rho\overline{u'v'} \qquad \tau_{\theta r} = \tau_{r\theta} = \mu\left[\frac{1}{r}\frac{\partial w}{\partial \theta} + \frac{\partial v}{\partial r}\right] - \rho\overline{v'w'}$$

$$\tau_{rx} = \tau_{xr} = \mu\left[\frac{\partial x}{\partial r} + \frac{\partial w}{\partial x}\right] - \rho\overline{w'u'} \qquad q_x = -k\frac{\partial T}{\partial x}; q_\theta = -k\frac{1}{r}\frac{\partial T}{\partial \theta}; q_r = -k\frac{\partial T}{\partial r}$$

The inviscid fluxes in the three coordinate directions are represented by the flux vectors F, G and H and the viscous fluxes are represented by the flux vectors F_V, G_V and H_V. The field vector U represents the vector of conservation variables. In the above expression for the fluxes, u_g, v_g and w_g are grid velocities, used to accommodate the movement of the mesh due to the blade motion. The system of equations is closed by an expression for pressure. For an ideal gas it is given by

$$p = (\gamma - 1)\left[\rho e - \frac{1}{2}\rho(u^2 + v^2 + w^2)\right] \tag{4.2}$$

The viscosity is $\mu = \mu_l + \mu_t$. The laminar viscosity μ_l is obtained from Sutherland's law. For the present work, it is assumed that the laminar and turbulent viscosity coefficients are frozen during linearization. The turbulent viscosity, μ_t, is obtained by the standard Baldwin-Lomax algebraic mixing length model (Baldwin and Lomax, 1978). The coefficient of heat conductivity, k, is related to the viscosity through Prandtl number.

4.2 Time Linearization

The governing equation can be linearized, provided the flow perturbations as well as the effects of deterministic stresses are small enough compared to the steady flow. The unsteady flow can be approximated as the sum of a mean or steady flow component and a small disturbance unsteady component. The small perturbation

32

assumption is valid for flows where the unsteady perturbations are less than about 10% of the mean flow. Therefore, the unsteady flow can be represented as

$$U(x,\theta,r,t) = \widehat{U}(x,\theta,r) + U'(x,\theta,r,t) \tag{4.3}$$

However, many flows of interest are harmonic in time. Further, many flows that are not harmonic are periodic in time. For the latter case, the unsteady perturbation flow can be expressed as a Fourier series where the frequency ω is $2\pi/T$. Since a linear assumption has been made, the behaviour of each Fourier component can be analysed individually, then summed together to form the total solution. Therefore, assuming that unsteady flow can be divided into two parts, a steady flow and a small harmonic perturbation part, for a single periodic disturbance, it can be represented as

$$U = \widehat{U} + \widetilde{U}e^{i\omega t} + \widetilde{U}_{-}e^{-i\omega t} \tag{4.4}$$

Here $\widetilde{U}$ is the vector of complex amplitudes of perturbations in the conservation variables given by

$$\widetilde{U} = \begin{pmatrix} \widetilde{\rho} \\ \widetilde{(\rho u)} \\ \widetilde{(\rho v)} \\ \widetilde{(\rho w)} \\ \widetilde{(\rho e)} \end{pmatrix} \tag{4.5}$$

and $\widetilde{U}_{-}$ is the complex conjugate of $\widetilde{U}$.

The unsteady grid moving velocities u_g, v_g and w_g are also assumed to change in a harmonic form,

$$u_g = \widehat{u}_g + (\widetilde{u}_g e^{i\omega t} + \widetilde{u}_{g-} e^{-i\omega t}), v_g = \widehat{v}_g + (\widetilde{v}_g e^{i\omega t} + \widetilde{v}_{g-} e^{-i\omega t}),$$
$$w_g = \widehat{w}_g + (\widetilde{w}_g e^{i\omega t} + \widetilde{w}_{g-} e^{-i\omega t}) \tag{4.6}$$

For a rotor, $\widehat{v}_g$ is the blade row rotating speed.

The computational grid is also assumed to undergo a small harmonic deformation about its steady position, i.e.,

$$x = \widehat{x} + (\widetilde{x}e^{i\omega t} + \widetilde{x}_{-}e^{-i\omega t}), \theta = \widehat{\theta} + (\widetilde{\theta}e^{i\omega t} + \widetilde{\theta}_{-}e^{-i\omega t}), r = \widehat{r} + (\widetilde{r}e^{i\omega t} + \widetilde{r}_{-}e^{-i\omega t}) \tag{4.7}$$

Substituting the relationships (4.4) through (4.7) into the integral form of the governing equation (4.1) and collecting the zeroth and first order terms, equation (4.1)

can be divided into two equations, i.e., the steady and the linearized unsteady equations respectively. The steady equation is given by

$$\oiint_A \left[\left(\widehat{F} - \widehat{F}_V \right) d\widehat{A}_x + \left(\widehat{G} - \widehat{G}_V \right) d\widehat{A}_\theta + \left(\widehat{H} - \widehat{H}_V \right) d\widehat{A}_r \right] = \iiint_{\Delta V} \widehat{S} d\widehat{V}$$

(4.8)

The linearized equation is

$$\oiint_A [(\widetilde{F} - \widetilde{F}_V)d\widehat{A}_x + (\widetilde{G} - \widetilde{G}_V)d\widehat{A}_\theta + (\widetilde{H} - \widetilde{H}_V)d\widehat{A}_r + (\widehat{F} - \widehat{F}_V)d\widetilde{A}_x +$$

$$(\widehat{G} - \widehat{G}_V)d\widetilde{A}_\theta + (\widehat{H} - \widehat{H}_V)d\widetilde{A}_r] = \iiint_{\Delta V}(\widehat{S}d\widetilde{V} + \widetilde{S}d\widehat{V}) - i\omega \iiint_{\Delta V}(\widehat{U}d\widetilde{V} + \widetilde{U}d\widehat{V})$$

(4.9)

All the variables in equations (4.8) and (4.9) are only space dependent and time does not appear as they are cast in the frequency domain. The coefficients in the linearized equation are obtained from the solution of the steady flow equation.

The perturbation fluxes are given by

$$\widetilde{F} = \begin{pmatrix} (\widetilde{\rho u}) - (\widetilde{\rho u}_g) \\ (\widehat{\rho u})(\tilde{u} - \tilde{u}_g) + (\widetilde{\rho u})(\hat{u} - \hat{u}_g) + \tilde{p} \\ r\left[(\widehat{\rho v})(\tilde{u} - \tilde{u}_g) + (\widetilde{\rho v})(\hat{u} - \hat{u}_g) \right] \\ (\widehat{\rho w})(\tilde{u} - \tilde{u}_g) + (\widetilde{\rho w})(\hat{u} - \hat{u}_g) \\ \left[(\widehat{\rho e}) + \hat{p} \right]\tilde{u} + \left[(\widetilde{\rho e}) + \tilde{p} \right]\hat{u} - (\widehat{\rho e})\tilde{u}_g - (\widetilde{\rho e})\hat{u}_g \end{pmatrix}$$

$$\widetilde{G} = \begin{pmatrix} (\widetilde{\rho v}) - (\widetilde{\rho v}_g) \\ (\widehat{\rho u})(\tilde{v} - \tilde{v}_g) + (\widetilde{\rho u})(\hat{v} - \hat{v}_g) \\ r\left[(\widehat{\rho v})(\tilde{v} - \tilde{v}_g) + (\widetilde{\rho v})(\hat{v} - \hat{v}_g) + \tilde{p} \right] \\ (\widehat{\rho w})(\tilde{v} - \tilde{v}_g) + (\widetilde{\rho w})(\hat{v} - \hat{v}_g) \\ \left[(\widehat{\rho e}) + \hat{p} \right]\tilde{v} + \left[(\widetilde{\rho e}) + \tilde{p} \right]\hat{v} - (\widehat{\rho e})\tilde{v}_g - (\widetilde{\rho e})\hat{v}_g \end{pmatrix}$$

34

$$\widetilde{H} = \begin{pmatrix} (\widetilde{\rho w}) - (\widetilde{\rho w}_g) \\ (\widehat{\rho u})(\widetilde{w} - \widetilde{w}_g) + (\widetilde{\rho u})(\widehat{w} - \widehat{w}_g) \\ r\left[(\widehat{\rho v})(\widetilde{w} - \widetilde{w}_g) + (\widetilde{\rho v})(\widehat{w} - \widehat{w}_g) \right] \\ (\widehat{\rho w})(\widetilde{w} - \widetilde{w}_g) + (\widetilde{\rho w})(\widehat{w} - \widehat{w}_g) + \widetilde{p} \\ \left[(\widehat{\rho e}) + \widehat{p} \right]\widetilde{w} + \left[(\widetilde{\rho e}) + \widetilde{p} \right]\widehat{w} - (\widehat{\rho e})\widetilde{w}_g - (\widetilde{\rho e})\widehat{w}_g \end{pmatrix}$$

$$\widetilde{F_V} = \begin{pmatrix} 0 \\ \widetilde{\tau}_{xx} \\ r\widetilde{\tau}_{x\theta} \\ \widetilde{\tau}_{xr} \\ \widehat{u}\widetilde{\tau}_{xx} + \widehat{v}\widetilde{\tau}_{x\theta} + \widehat{w}\widetilde{\tau}_{xr} + \widetilde{u}\widehat{\tau}_{xx} + \widetilde{v}\widehat{\tau}_{x\theta} + \widetilde{w}\widehat{\tau}_{xr} - \widetilde{q}_x \end{pmatrix}$$

$$\widetilde{G_V} = \begin{pmatrix} 0 \\ \widetilde{\tau}_{\theta x} \\ r\widetilde{\tau}_{\theta\theta} \\ \widetilde{\tau}_{\theta r} \\ \widehat{u}\widetilde{\tau}_{\theta x} + \widehat{v}\widetilde{\tau}_{\theta\theta} + \widehat{w}\widetilde{\tau}_{\theta r} + \widetilde{u}\widehat{\tau}_{\theta x} + \widetilde{v}\widehat{\tau}_{\theta\theta} + \widetilde{w}\widehat{\tau}_{\theta r} - \widetilde{q}_\theta \end{pmatrix}$$

$$\widetilde{H_V} = \begin{pmatrix} 0 \\ \widetilde{\tau}_{rx} \\ r\widetilde{\tau}_{r\theta} \\ \widetilde{\tau}_{rr} \\ \widehat{u}\widetilde{\tau}_{rx} + \widehat{v}\widetilde{\tau}_{r\theta} + \widehat{w}\widetilde{\tau}_{rr} + \widetilde{u}\widehat{\tau}_{rx} + \widetilde{v}\widehat{\tau}_{r\theta} + \widetilde{w}\widehat{\tau}_{rr} - \widetilde{q}_r \end{pmatrix}$$

$$\widetilde{S} = \begin{pmatrix} 0 \\ 0 \\ 0 \\ \left[(\widehat{\rho v})\widetilde{v} + (\widetilde{\rho v})\widehat{v} \right]/r \\ 0 \end{pmatrix}$$

In the perturbation equation, the perturbation of viscosity is neglected by freezing the viscosity to its steady value. Although the turbulence modelling could be linearized to get the turbulent viscosity perturbation, this will increase the computation time and make the code writing more complex. Under the Boussinesq approximation, the primary role of turbulence is to provide enhanced diffusivities intended to mimic the turbulent mixing. For moderate Mach numbers and moderate turbulent kinetic energies, so long as there is no large separation, the interaction of the turbulence with the mean flow is minor compared to the added diffusivity introduced by the eddy viscosity. Holmes and Lorence (1997) have made blade flutter computations using a linearized turbulence model and a normal turbulence model with frozen viscosity and found that the results are nearly identical in both the cases for normal blade flutter frequencies and the difference appears only in extremely low frequency cases (reduced frequency of 0.034).

4.3 Numerical Solution Method

Firstly, a steady flow solution is obtained by solving the steady Navier-Stokes equation. The grid moving velocities are then prescribed according to the blade vibrating mode shape. Then, for a given frequency and inter-blade phase angle, the coefficients of the time-linearized equations are formed from the steady flow solution and the time-linearized perturbation equations are solved. By linearization and harmonic representation, solving a time-dependent unsteady problem in the time domain is effectively transformed to solving two steady equations in the frequency domain.

4.3.1 Pseudo Time Dependence and Numerical Discretization

In order to fully take advantage of the existing time-marching methods that are widely used for steady flow calculations, a pseudo time variable (t'), as originally proposed by Ni and Sisto (1976), is introduced to make the steady equation and the time-linearized perturbation equation time-dependent, so equations (4.8) and (4.9) can be rewritten as

$$\frac{\partial}{\partial t'}\iiint_{\Delta V}\widehat{U}d\widehat{V}+\oiint_{A}\left[(\widehat{F}-\widehat{F}_V)d\widehat{A}_x+(\widehat{G}-\widehat{G}_V)d\widehat{A}_\theta+(\widehat{H}-\widehat{H}_V)d\widehat{A}_r\right]=\iiint_{\Delta V}\widehat{S}d\widehat{V}$$

$$(4.10)$$

and

$$\frac{\partial}{\partial t'}\iiint_{\Delta V}\widetilde{U}d\widehat{V} + \oiint_{A}[(\widetilde{F}-\widetilde{F}_V)d\widehat{A}_x + (\widetilde{G}-\widetilde{G}_V)d\widehat{A}_\theta + (\widetilde{H}-\widetilde{H}_V)d\widehat{A}_r + (\widehat{F}-\widehat{F}_V)d\widetilde{A}_x$$
$$+(\widehat{G}-\widehat{G}_V)d\widetilde{A}_\theta + (\widehat{H}-\widehat{H}_V)d\widetilde{A}_r] = \iiint_{\Delta V}(\widehat{S}d\widetilde{V}+\widetilde{S}d\widehat{V}) - i\omega\iiint_{\Delta V}(\widehat{U}d\widetilde{V}+\widetilde{U}d\widehat{V})$$

$$(4.11)$$

Now both the steady equation and the linear perturbation equation are hyperbolic in nature and any well-developed time-marching scheme can be used to solve them. Since only a steady state solution for steady flow equations and unsteady perturbation equations is desired, any efficient acceleration technique like local time stepping and multigrid can be used to speed up the convergence of the solution.

The spatial discretization for both Eq. (4.10) and Eq. (4.11) is made using a cell centred finite volume scheme. For a hexahedral control volume, as shown in Fig. 4.1, after semi-discretization, equations (4.10) and (4.11) can be written as

$$\frac{d}{dt'}(\widehat{U}d\widehat{V})_{ijk} = \widehat{Flux} + (\widehat{S}\Delta\widehat{V})_{ijk} = \widehat{R}_{ijk} \qquad (4.12)$$

and

$$\frac{d}{dt'}(\widetilde{U}d\widehat{V})_{ijk} = \widetilde{Flux} + (\widetilde{S}\Delta\widehat{V})_{ijk} + (\widehat{S}\Delta\widetilde{V})_{ijk} - i\omega(\widetilde{U}\Delta\widehat{V}+\widehat{U}\Delta\widetilde{V}) = \widetilde{R}_{ijk} \qquad (4.13)$$

where

$$\widehat{Flux} = (\widehat{F}+\widehat{F}_V)(\Delta\widehat{A}_{x_x}+\Delta\widehat{A}_{\theta_x}+\Delta\widehat{A}_{r_x}) + (\widehat{G}+\widehat{G}_V)(\Delta\widehat{A}_{x_\theta}+\Delta\widehat{A}_{\theta_\theta}+\Delta\widehat{A}_{r_\theta}) +$$
$$+(\widehat{H}+\widehat{H}_V)(\Delta\widehat{A}_{x_r}+\Delta\widehat{A}_{\theta_r}+\Delta\widehat{A}_{r_r})$$

and

$$\widetilde{Flux} = (\widetilde{F}+\widetilde{F}_V)(\Delta\widehat{A}_{x_x}+\Delta\widehat{A}_{\theta_x}+\Delta\widehat{A}_{r_x}) + (\widetilde{G}+\widetilde{G}_V)(\Delta\widehat{A}_{x_\theta}+\Delta\widehat{A}_{\theta_\theta}+\Delta\widehat{A}_{r_\theta})$$
$$+(\widetilde{H}+\widetilde{H}_V)(\Delta\widehat{A}_{x_r}+\Delta\widehat{A}_{\theta_r}+\Delta\widehat{A}_{r_r}) + (\widehat{F}+\widehat{F}_V)(\Delta\widetilde{A}_{x_x}+\Delta\widetilde{A}_{\theta_x}+\Delta\widetilde{A}_{r_x})$$
$$+(\widehat{G}+\widehat{G}_V)(\Delta\widetilde{A}_{x_\theta}+\Delta\widetilde{A}_{\theta_\theta}+\Delta\widetilde{A}_{r_\theta}) + (\widehat{H}+\widehat{H}_V)(\Delta\widetilde{A}_{x_r}+\Delta\widetilde{A}_{\theta_r}+\Delta\widetilde{A}_{r_r})$$

$\widehat{A}_{x_x}, \widehat{A}_{\theta_x}$ and $\widehat{A}_{r_x}$ are steady projected areas and $\widetilde{A}_{x_x}, \widetilde{A}_{\theta_x}$ and $\widetilde{A}_{r_x}$ are unsteady projected areas in the x direction of faces normal to the streamwise, pitchwise and radial directions respectively. Similarly, $\widehat{A}_{x_\theta}, \widehat{A}_{\theta_\theta}$ & $\widehat{A}_{r_\theta}$, $\widehat{A}_{x_r}, \widehat{A}_{\theta_r}$ & $\widehat{A}_{r_r}$, $\widetilde{A}_{x_\theta}, \widetilde{A}_{\theta_\theta}$ & $\widetilde{A}_{r_\theta}$ and $\widetilde{A}_{x_r}, \widetilde{A}_{\theta_r}$ & $\widetilde{A}_{r_r}$ are steady and unsteady projected areas in the θ and r directions respectively. Fluxes in all three directions through faces in streamwise, pitchwise and radial directions are summed up. For viscous fluxes, the first order spatial derivatives

are evaluated using the Gauss theorem. The cell centred finite volume scheme is a spatial second order central difference scheme. In order to suppress numerical oscillation, a second and fourth order adaptive smoothing (Jameson, 1981) is applied in the streamwise, pitchwise and radial directions. The semi-discretized equations (4.12) and (4.13) become

$$\frac{d}{dt'}(\widehat{U}d\widehat{V})_{ijk} = \widehat{R}_{ijk} + \widehat{d}_x + \widehat{d}_\theta + \widehat{d}_r - \widehat{D}_x - \widehat{D}_\theta - \widehat{D}_r \qquad (4.14)$$

$$\frac{d}{dt'}(\widetilde{U}d\widehat{V})_{ijk} = \widetilde{R}_{ijk} + \widetilde{d}_x + \widetilde{d}_\theta + \widetilde{d}_r - \widetilde{D}_x - \widetilde{D}_\theta - \widetilde{D}_r \qquad (4.15)$$

where $\widehat{d}_x, \widehat{d}_\theta$ and $\widehat{d}_r$ are second order steady smoothing terms and $\widehat{D}_x, \widehat{D}_\theta$ and $\widehat{D}_r$ are the fourth order smoothing terms in x, θ and r directions respectively. $\widetilde{d}_x, \widetilde{d}_\theta$ and $\widetilde{d}_r$ are the unsteady amplitudes of second order smoothing terms and $\widetilde{D}_x, \widetilde{D}_\theta$ and $\widetilde{D}_r$ are unsteady amplitudes of fourth order smoothing terms. For the steady flow equations $\widehat{d}_x$ and $\widehat{D}_x$ are given by

$$\widehat{d}_x = \varepsilon_{ijk}^{(2)}(\widehat{U}_{i+1,j,k} - 2\widehat{U}_{i,j,k} + \widehat{U}_{i-1,j,k})\Delta\widehat{V}/\Delta t' \qquad (4.16)$$

$$\widehat{D}_x = \varepsilon_{ijk}^{(4)}(\widehat{U}_{i+2,j,k} - 4\widehat{U}_{i+1,j,k} + 5\widehat{U}_{i,j,k} - 4\widehat{U}_{i-1,j,k} + \widehat{U}_{i-2,j,k})\Delta\widehat{V}/\Delta t' \qquad (4.17)$$

where

$$\varepsilon_{ijk}^{(2)} = k^{(2)}\theta_{ijk}^{(2)} \qquad (4.18)$$

$$\theta_{ijk}^{(2)} = \left| \frac{p_{i+1,j,k} - 2p_{i,j,k} + p_{i-1,j,k}}{p_{i+1,j,k} + 2p_{i,j,k} + p_{i-1,j,k}} \right| \qquad (4.19)$$

and

$$\varepsilon_{ijk}^{(4)} = \max\left(0,(k^{(4)} - \varepsilon_{ijk}^{(2)})\right) \qquad (4.20)$$

where $k^{(2)}$ is the second order smoothing coefficient with a typical value of 1/2 and $k^{(4)}$ is the fourth order smoothing coefficient with a typical value of 1/32. $\widehat{d}_\theta, \widehat{d}_r$ and $\widehat{D}_\theta, \widehat{D}_r$ can be given similarly.

For unsteady perturbation equation $\widetilde{d}_x$ and $\widetilde{D}_x$ are given by

$$\widetilde{d}_x = \varepsilon_{ijk}^{(2)}(\widetilde{U}_{i+1,j,k} - 2\widetilde{U}_{i,j,k} + \widetilde{U}_{i-1,j,k})\Delta\widehat{V}/\Delta t' \qquad (4.21)$$

$$\widetilde{D}_x = \varepsilon_{ijk}^{(4)}(\widetilde{U}_{i+2,j,k} - 4\widetilde{U}_{i+1,j,k} + 5\widetilde{U}_{i,j,k} - 4\widetilde{U}_{i-2,j,k} + \widetilde{U}_{i-1,j,k})\Delta\widehat{V}/\Delta t' \qquad (4.22)$$

The pressure sensor $\theta_{ijk}^{(2)}$ in the above expression (4.19) has not been linearized and smoothing coefficients for the unsteady amplitudes are frozen at their steady value. The unsteady fluctuations of the pressure sensor have been neglected here and this is acceptable for and consistent with linear problems.

The pseudo time-marching for both the equations (4.14) and (4.15) is performed by using the four stage Runge-Kutta scheme. The formulation for four stage Runge-Kutta scheme from time step n to n+1 is

$$\widehat{U}^{n+\alpha_k} = \widehat{U}_{ijk}^n - \alpha_k \frac{\Delta t'}{\Delta\widehat{V}}\left[\widehat{R}_{ijk} + \widehat{d}_x + \widehat{d}_\theta + \widehat{d}_r - \widehat{D}_x - \widehat{D}_\theta - \widehat{D}_r\right]^{n+\alpha_{k-1}} \qquad (4.23)$$

and

$$\widetilde{U}^{n+\alpha_k} = \widetilde{U}_{ijk}^n - \alpha_k \frac{\Delta t'}{\Delta\widehat{V}}\left[\widetilde{R}_{ijk} + \widetilde{d}_x + \widetilde{d}_\theta + \widetilde{d}_r - \widetilde{D}_x - \widetilde{D}_\theta - \widetilde{D}_r\right]^{n+\alpha_{k-1}} \qquad (4.24)$$

where $k = 1$ to 4, and for a four stage scheme the values of α are

$$\alpha_0 = 0, \alpha_1 = \frac{1}{4}, \alpha_2 = \frac{1}{3}, \alpha_3 = \frac{1}{2} \text{ and } \alpha_4 = 1.$$

4.3.2 Boundary Conditions

For a single blade passage domain as in the present case, there are four kinds of boundary conditions, i.e. inlet, outlet, periodic and solid wall boundary conditions. For steady flow calculation, the conventional boundary conditions are implemented. A critical step in the implementation of boundary conditions is to separate the waves into incoming and outgoing modes. The propagation properties in a one-dimensional flow are expressed in a straightforward way by the characteristic variables. The form of the missing information is defined by variables associated with the outgoing characteristics. In a three-dimensional flow, for a subsonic inlet, four characteristics are incoming and one is outgoing. At outlet, four characteristics are outgoing and one is incoming. Therefore, at inlet, total pressure, total temperature and inlet flow angle for subsonic flow or inlet Mach number for supersonic flow are prescribed, and the static pressure at inlet is extrapolated from the interior domain. At outlet, the static pressure is prescribed and other flow variables are extrapolated from the interior domain. For periodic boundaries, a direct repeating condition is applied on both the

upper and lower boundaries. On the blade surface, zero flux is applied across the boundaries for inviscid and viscous flow calculation. For viscous flow calculation, either a no slip wall or slip wall boundary treatment can be used. For the no slip wall boundary condition, the velocities on the blade surface are set to be zero and the wall shear stress is evaluated from the local velocity gradients. The no slip wall boundary condition requires a very fine mesh in the boundary layer region. For slip wall condition, the wall shear stress for turbulent flows is approximated by a log law formulation (Denton, 1990), as

$$\hat{\tau}_w = \frac{1}{2}\hat{c}_f \hat{\rho}_2 \hat{V}_2^2 \tag{4.25}$$

where

$$\hat{c}_f = \begin{cases} \dfrac{2}{\widehat{Re}_2}; \widehat{Re}_2 < 125 \\ -0.001767 + \dfrac{0.03177}{\ln(\widehat{Re}_2)} + \dfrac{0.25614}{\left[\ln(\widehat{Re}_2)\right]^2}; \widehat{Re}_2 \geq 125 \end{cases}, \tag{4.26}$$

$$\widehat{Re}_2 = \hat{\rho}_2 \hat{V}_2 \Delta y_2 / \mu_l,$$

$$\hat{V}_2 = \sqrt{\hat{u}_2^2 + \left(\hat{v}_2 - \hat{v}_g\right)^2 + \hat{w}_2^2} \tag{4.27}$$

The subscript 2 in the above expressions represents the mesh point one grid away from the wall. The slip wall condition requires fewer mesh points near the wall than the no slip wall condition and thereby saves computational time.

The boundary conditions for solving the time-linearized equations are different from those for solving steady flow equations. For periodic boundaries, a phase-shifted periodic condition is applied for solving the perturbation equation, i.e.

$$\widetilde{U}^U = \widetilde{U}^L e^{i\sigma} \tag{4.28}$$

where σ is the inter-blade phase angle and the superscript U refers to the upper boundary and L refers to the lower boundary.

At inlet and outlet, the one-dimensional non-reflecting boundary conditions developed by Giles (1990) and Saxer and Giles (1993) are implemented. The usual one-dimensional approach is to assume perturbation travelling normal to the boundary in

the x direction. Hence the one-dimensional linearized Euler equations pre-multiplied by the left eigenvector are written as

$$\frac{\partial \widetilde{\phi}}{\partial t} + \Lambda \frac{\partial \widetilde{\phi}}{\partial x} = 0 \tag{4.29}$$

where $\widetilde{\phi} = T^{-1}\widetilde{U}$ and Λ is the diagonal vector whose components represent the speed of propagation (eigenvalues) of five characteristic waves, called the entropy, the two vorticity and the upstream running and downstream running pressure waves. T^{-1} is the left eigenvector and $\widetilde{\phi}$ is referred to as the vector of linearized characteristic variables.

To implement the non-reflecting boundary conditions, firstly the transformation between the amplitudes of five characteristic waves and amplitudes of pressure, density and velocities are given by

$$
\begin{pmatrix} \widetilde{\phi_1} \\ \widetilde{\phi_2} \\ \widetilde{\phi_3} \\ \widetilde{\phi_4} \\ \widetilde{\phi_5} \end{pmatrix}
=
\begin{pmatrix}
-\hat{c}^2 & 0 & 0 & 0 & 1 \\
0 & 0 & \hat{\rho}\hat{c} & 0 & 0 \\
0 & 0 & 0 & \hat{\rho}\hat{c} & 0 \\
0 & \hat{\rho}\hat{c} & 0 & 0 & 1 \\
0 & -\hat{\rho}\hat{c} & 0 & 0 & 1
\end{pmatrix}
\begin{pmatrix} \widetilde{\rho} \\ \widetilde{u} \\ \widetilde{v} \\ \widetilde{w} \\ \widetilde{p} \end{pmatrix}
\tag{4.30}
$$

and

$$
\begin{pmatrix} \widetilde{\rho} \\ \widetilde{u} \\ \widetilde{v} \\ \widetilde{w} \\ \widetilde{p} \end{pmatrix}
=
\begin{pmatrix}
-\dfrac{1}{\hat{c}^2} & 0 & 0 & \dfrac{1}{2\hat{c}^2} & \dfrac{1}{2\hat{c}^2} \\
0 & 0 & 0 & \dfrac{1}{2\hat{\rho}\hat{c}} & -\dfrac{1}{2\hat{\rho}\hat{c}} \\
0 & \dfrac{1}{\hat{\rho}\hat{c}} & 0 & 0 & 0 \\
0 & 0 & \dfrac{1}{\hat{\rho}\hat{c}} & 0 & 0 \\
0 & 0 & 0 & \dfrac{1}{2} & \dfrac{1}{2}
\end{pmatrix}
\begin{pmatrix} \widetilde{\phi_1} \\ \widetilde{\phi_2} \\ \widetilde{\phi_3} \\ \widetilde{\phi_4} \\ \widetilde{\phi_5} \end{pmatrix}
\tag{4.31}
$$

41

where $\widetilde{\phi}_1, \widetilde{\phi}_2, \widetilde{\phi}_3, \widetilde{\phi}_4$ and $\widetilde{\phi}_5$ are the amplitudes of the five characteristic waves (entropy, two vorticity and upstream and downstream running pressure waves). $\hat{c}$ is the local speed of sound.

In order to handle the forced response problems induced by incoming wakes or distortions, the transformation relationships of (4.28) and (4.29) at inlet can be rewritten as

$$
\begin{pmatrix} \widetilde{\phi}_1 \\ \widetilde{\phi}_2 \\ \widetilde{\phi}_3 \\ \widetilde{\phi}_4 \\ \widetilde{\phi}_5 \end{pmatrix} = \begin{pmatrix} -\hat{c}^2 & 0 & 0 & 0 & 1 \\ 0 & 0 & \hat{\rho}\hat{c} & 0 & 0 \\ 0 & 0 & 0 & \hat{\rho}\hat{c} & 0 \\ 0 & \hat{\rho}\hat{c} & 0 & 0 & 1 \\ 0 & -\hat{\rho}\hat{c} & 0 & 0 & 1 \end{pmatrix} \begin{pmatrix} \widetilde{\rho} - \widetilde{\rho}_{inl} \\ \widetilde{u} - \widetilde{u}_{inl} \\ \widetilde{v} - \widetilde{v}_{inl} \\ \widetilde{w} - \widetilde{w}_{inl} \\ \widetilde{p} - \widetilde{p}_{inl} \end{pmatrix}
\tag{4.32}
$$

$$
\begin{pmatrix} \widetilde{\rho} - \widetilde{\rho}_{inl} \\ \widetilde{u} - \widetilde{u}_{inl} \\ \widetilde{v} - \widetilde{v}_{inl} \\ \widetilde{w} - \widetilde{w}_{inl} \\ \widetilde{p} - \widetilde{p}_{inl} \end{pmatrix} = \begin{pmatrix} -\dfrac{1}{\hat{c}^2} & 0 & 0 & \dfrac{1}{2\hat{c}^2} & \dfrac{1}{2\hat{c}^2} \\ 0 & 0 & 0 & \dfrac{1}{2\hat{\rho}\hat{c}} & -\dfrac{1}{2\hat{\rho}\hat{c}} \\ 0 & \dfrac{1}{\hat{\rho}\hat{c}} & 0 & 0 & 0 \\ 0 & 0 & \dfrac{1}{\hat{\rho}\hat{c}} & 0 & 0 \\ 0 & 0 & 0 & \dfrac{1}{2} & \dfrac{1}{2} \end{pmatrix} \begin{pmatrix} \widetilde{\phi}_1 \\ \widetilde{\phi}_2 \\ \widetilde{\phi}_3 \\ \widetilde{\phi}_4 \\ \widetilde{\phi}_5 \end{pmatrix}
\tag{4.33}
$$

where $\widetilde{\rho}_{inl}, \widetilde{u}_{inl}, \widetilde{v}_{inl}, \widetilde{w}_{inl}$ and $\widetilde{p}_{inl}$ are amplitudes of the prescribed incoming wake profile. The incoming wake can be prescribed by different ways such as a simple sinusoidal distribution or superposition of different Fourier harmonic components for a more accurate expression.

At a subsonic inlet the correct unsteady, non-reflecting boundary conditions would be

$$
\begin{pmatrix} \widetilde{\phi}_1 \\ \widetilde{\phi}_2 \\ \widetilde{\phi}_3 \\ \widetilde{\phi}_4 \end{pmatrix} = 0
\tag{4.34}
$$

while at an outlet the correct non-reflecting boundary conditions would be

42

$$\widetilde{\phi}_5 = 0 \tag{4.35}$$

The standard numerical method for implementing these would be to calculate or extrapolate the outgoing characteristic values from the interior domain, and then use Eq. (4.31) to reconstruct the solution on the boundary.

A more accurate two-dimensional boundary condition is also implemented as proposed by Saxer and Giles (1993) and is given as

At inlet:
$$\frac{\partial}{\partial t'}\begin{pmatrix} \widetilde{\phi}_1 \\ \widetilde{\phi}_2 \\ \widetilde{\phi}_3 \\ \widetilde{\phi}_4 \end{pmatrix} = \alpha \begin{pmatrix} -\widetilde{\phi}_1 \\ -\left[\left(\beta+\hat{v}\right)\Big/\left(\hat{c}+\hat{u}\right)\right]\widetilde{\phi}_5 - \widetilde{\phi}_2 \\ -\widetilde{\phi}_3 \\ \left[\left(\beta+\hat{v}\right)\Big/\left(\hat{c}+\hat{u}\right)\right]^2 \widetilde{\phi}_5 - \widetilde{\phi}_4 \end{pmatrix} \tag{4.36}$$

At outlet:
$$\frac{\partial \widetilde{\phi}_5}{\partial t'} = \alpha \left[\left(\frac{2\hat{u}}{\beta-\hat{v}}\right)\widetilde{\phi}_2 - \left(\frac{\beta+\hat{v}}{\beta-\hat{v}}\right)\widetilde{\phi}_4 - \widetilde{\phi}_5 \right] \tag{4.37}$$

where $\beta = \begin{cases} \sqrt{\hat{c}^2 - \left(\hat{u}^2 + \hat{v}^2\right)}, & \left(\hat{u}^2 + \hat{v}^2\right) < \hat{c}^2 \\ \sqrt{\left(\hat{u}^2 + \hat{v}^2\right) - \hat{c}^2}, & \left(\hat{u}^2 + \hat{v}^2\right) > \hat{c}^2 \end{cases}$

A suitable choice for α is $\hat{c}\big/\Delta y_{pitch}$ where Δy_{pitch} is the blade pitch.

As far as solid wall boundary conditions are concerned, for inviscid flow calculations involving the time-linearized Euler equations, the perturbations of fluxes on the blade surface are set to zero. For viscous flow calculations solving the time-linearized Navier-Stokes equations, both no slip wall and slip wall boundary conditions can be implemented. The velocity perturbations on the solid wall are set to zero for the no slip wall boundary condition and the perturbation of wall shear stress is evaluated according to the local velocity gradients. For the slip wall condition, the perturbation of shear stress is obtained by linearizing the nonlinear relationship

$$\tau_w = \frac{1}{2}c_f \rho V_2^{\;2} \tag{4.38}$$

to give

$$\tilde{\tau}_w = \frac{1}{2}\left[\hat{c}_f\,\hat{\rho}_2\,\hat{V}_2\,\tilde{V}_2\right] \qquad\qquad (4.39)$$

In this chapter, the complete three-dimensional formulation for the time-linearized method for the Reynolds averaged Navier-Stokes equations has been presented. This forms the basis for the development of three-dimensional nonlinear harmonic method for the Euler/Navier-Stokes equations. In the time-linearized method, the unsteady flow is decomposed into a steady flow and a harmonically varying small perturbation. Linearization transforms the original unsteady flow governing equation into a steady flow equation and a linear perturbation equation. A pseudo-time technique is introduced to make these two equations time dependent. The spatial discretization of these equations is achieved by a cell centred finite volume scheme and the temporal discretization is carried out by the four stage Runge-Kutta scheme. Since the original unsteady flow equation in time-domain has been converted to two equivalent steady flow equations by linearization, the time-linearized method is computationally more efficient than the nonlinear time-marching method since computations are needed to be performed only in a single passage as against multiple passage calculations in the case of nonlinear time-marching method.

Chapter 5

Nonlinear Harmonic Method

5.1   Time-Averaging and Incorporating Nonlinearity

The time-linearized approach results in solving two steady, single passage problems instead of the original unsteady problem. The main feature of the time-linearized approach is its high computational efficiency compared to the nonlinear time-marching methods. However, this approach is restricted to linear problems due to the linear assumption. Although the onset of flutter in turbomachinery is widely accepted to be a linear phenomenon, the nonlinear effects with shock oscillations and viscous flow separations can be potentially important. On the other hand, the forced response of turbomachinery blades due to non-uniformity of unsteady flow fields like an incoming wake, inlet distortion and potential interaction etc. is not necessarily a linear phenomenon. Therefore, it is highly desirable to develop a numerical method that has the high computational efficiency of time-linearized methods whilst including the nonlinear effects like the nonlinear time-marching methods. The average passage equation system formulated by Adamczyk showed that time-averaging the Navier Stokes equations resulted in the inclusion of the effect of deterministic periodic unsteadiness on the mean flow through stress terms similar to the Reynolds stresses. Extra closure models are required to work out these deterministic stress terms similar to turbulence modelling for Reynolds stress terms. Giles (1992) combined this averaging approach with the linear unsteady flow modelling by including quadratic source terms to account for the time-averaged effect. He (1996) proposed a nonlinear harmonic methodology in which the extra stress terms in the time-averaged equations are solved simultaneously with the harmonic perturbation equation using a strongly coupled approach.

In the nonlinear harmonic method, a simple but significant change from the time-linearized method is that a time-averaged flow field instead of a steady flow field is used as the basis for the harmonic perturbations. The unsteady flow field is assumed to be composed of two parts; a time-averaged flow plus an unsteady perturbation, e.g.,

$$U = \overline{U} + U'$$

(5.1)

45

where

$$\overline{U} = \begin{pmatrix} \overline{\rho} \\ \overline{(\rho u)} \\ r\overline{(\rho v)} \\ \overline{(\rho w)} \\ \overline{(\rho e)} \end{pmatrix} \qquad \text{and} \qquad U' = \begin{pmatrix} \rho' \\ (\rho u)' \\ r(\rho v)' \\ (\rho w)' \\ (\rho e)' \end{pmatrix}$$

(5.2)

and $\overline{U}$ is the vector of time-averaged conservative variables and U' is the vector of perturbation variables. Similarly, the grid moving velocities are also divided into a mean part plus a perturbation, i.e.

$$u_g = \overline{u}_g + u'_g \quad , \quad v_g = \overline{v}_g + v'_g \quad , \quad w_g = \overline{w}_g + w'_g$$

(5.3)

The computational grid can also be expressed by its steady position plus a small perturbation, i.e.

$$x = \overline{x} + x' \quad , \quad \theta = \overline{\theta} + \theta' \quad , \quad r = \overline{r} + r'$$

(5.4)

Substituting the expressions (5.1) through (5.4) into the original nonlinear integral equation (4.1), and time-averaging it, the resultant time-averaged Navier-Stokes equation can be given by

$$\oiint_A (\overline{F} - \overline{F_V})d\overline{A}_x + (\overline{G} - \overline{G_V})d\overline{A}_\theta + (\overline{H} - \overline{H_V})d\overline{A}_r + (\overline{F'dA'_x}) + (\overline{G'dA'_\theta}) + (\overline{H'dA'_r})$$
$$-(\overline{F'_V dA'_x}) - (\overline{G'_V dA'_\theta}) - (\overline{H'_V dA'_r}) = \iiint_{\Delta V} (\overline{S}d\overline{V} + \overline{S'dV'})$$

(5.5)

where

$$\overline{F} = \begin{pmatrix} \overline{\rho u} - \overline{\rho u_g} \\ (\overline{\rho u} - \overline{\rho u_g})\overline{u} + \overline{p} + \overline{(\rho u)'u'} - \overline{(\rho u_g)'u'} \\ r\left[(\overline{\rho u} - \overline{\rho u_g})\overline{v} + \overline{(\rho u)'v'} - \overline{(\rho u_g)'v'} \right] \\ (\overline{\rho u} - \overline{\rho u_g})\overline{w} + \overline{(\rho u)'w'} - \overline{(\rho u_g)'w'} \\ (\overline{\rho u} - \overline{\rho u_g})\overline{e} + \overline{pu} + \overline{p'u'} + \overline{(\rho u)'e'} - \overline{(\rho u_g)'e'} \end{pmatrix}$$

$$\overline{G} = \begin{pmatrix} \overline{\rho v} - \overline{\rho v_g} \\ (\overline{\rho v} - \overline{\rho v_g})\overline{u} + \overline{(\rho v)'u'} - \overline{(\rho v_g)'u'} \\ r\left[(\overline{\rho v} - \overline{\rho v_g})\overline{v} + \overline{p} + \overline{(\rho v)'v'} - \overline{(\rho v_g)'v'} \right] \\ (\overline{\rho v} - \overline{\rho v_g})\overline{w} + \overline{(\rho v)'w'} - \overline{(\rho v_g)'w'} \\ (\overline{\rho v} - \overline{\rho v_g})\overline{e} + \overline{pv} + \overline{p'v'} + \overline{(\rho v)'e'} - \overline{(\rho v_g)'e'} \end{pmatrix}$$

$$\overline{H} = \begin{pmatrix} \overline{\rho w} - \overline{\rho w_g} \\ (\overline{\rho w} - \overline{\rho w_g})\overline{u} + \overline{(\rho w)'u'} - \overline{(\rho w_g)'u'} \\ r\left[(\overline{\rho w} - \overline{\rho w_g})\overline{v} + \overline{(\rho w)'v'} - \overline{(\rho w_g)'v'} \right] \\ (\overline{\rho w} - \overline{\rho w_g})\overline{w} + \overline{p} + \overline{(\rho w)'w'} - \overline{(\rho w_g)'w'} \\ (\overline{\rho w} - \overline{\rho w_g})\overline{e} + \overline{pw} + \overline{p'w'} + \overline{(\rho w)'e'} - \overline{(\rho w_g)'e'} \end{pmatrix}$$

$$\overline{F_V} = \begin{pmatrix} 0 \\ \overline{\tau}_{xx} \\ r\overline{\tau}_{x\theta} \\ \overline{\tau}_{xr} \\ \overline{u}\overline{\tau}_{xx} + \overline{v}\overline{\tau}_{x\theta} + \overline{w}\overline{\tau}_{xr} + \overline{u'\tau'_{xx}} + \overline{v'\tau'_{x\theta}} + \overline{w'\tau'_{xr}} - \overline{q}_x \end{pmatrix}$$

$$\overline{G_V} = \begin{pmatrix} 0 \\ \overline{\tau}_{\theta x} \\ r\overline{\tau}_{\theta\theta} \\ \overline{\tau}_{\theta r} \\ \overline{u}\overline{\tau}_{\theta x} + \overline{v}\overline{\tau}_{\theta\theta} + \overline{w}\overline{\tau}_{\theta r} + \overline{u'\tau'_{\theta x}} + \overline{v'\tau'_{\theta\theta}} + \overline{w'\tau'_{\theta r}} - \overline{q}_\theta \end{pmatrix}$$

$$\overline{H_V} = \begin{pmatrix} 0 \\ \overline{\tau}_{rx} \\ r\overline{\tau}_{r\theta} \\ \overline{\tau}_{rr} \\ \overline{u}\overline{\tau}_{rx} + \overline{v}\overline{\tau}_{r\theta} + \overline{w}\overline{\tau}_{rr} + \overline{u'\tau'_{rx}} + \overline{v'\tau'_{r\theta}} + \overline{w'\tau'_{rr}} - \overline{q}_r \end{pmatrix}$$

47

$$\overline{S} = \begin{pmatrix} 0 \\ 0 \\ 0 \\ \left[\overline{\rho v v} + \overline{(\rho v)' v'} \right] / r \\ 0 \end{pmatrix} \qquad \text{and}$$

$$\overline{\tau}_{xx} = \frac{2}{3} \mu \left[2 \frac{\partial \overline{u}}{\partial x} - \frac{\partial \overline{w}}{\partial r} - \frac{1}{r} \frac{\partial \overline{v}}{\partial \theta} \right] \quad , \quad \overline{\tau}_{\theta\theta} = \frac{2}{3} \mu \left[2 \frac{1}{r} \frac{\partial \overline{v}}{\partial \theta} - \frac{\partial \overline{u}}{\partial x} - \frac{\partial \overline{w}}{\partial r} \right] \quad ,$$

$$\overline{\tau}_{rr} = \frac{2}{3} \mu \left[2 \frac{\partial \overline{w}}{\partial r} - \frac{1}{r} \frac{\partial \overline{v}}{\partial \theta} - \frac{\partial \overline{u}}{\partial x} \right] \quad , \quad \overline{\tau}_{x\theta} = \overline{\tau}_{\theta x} = \mu \left[\frac{\partial \overline{v}}{\partial x} + \frac{1}{r} \frac{\partial \overline{u}}{\partial \theta} \right] \quad ,$$

$$\overline{\tau}_{\theta r} = \overline{\tau}_{r\theta} = \mu \left[\frac{1}{r} \frac{\partial \overline{w}}{\partial \theta} + \frac{\partial \overline{v}}{\partial r} \right] \quad , \quad \overline{\tau}_{rx} = \overline{\tau}_{xr} = \mu \left[\frac{\partial \overline{u}}{\partial r} + \frac{\partial \overline{w}}{\partial x} \right] \quad ,$$

$$\overline{q}_{x} = -k \frac{\partial \overline{T}}{\partial x} \quad , \quad \overline{q}_{\theta} = -k \frac{1}{r} \frac{\partial \overline{T}}{\partial \theta} \quad , \quad \overline{q}_{r} = -k \frac{\partial \overline{T}}{\partial r}$$

Here again, it is assumed that the laminar and turbulent viscosity coefficients are frozen during time-averaging. As a result, the viscous terms are in a linear form except for those concerning the work done by viscous stresses in the energy equations.

The comparison between time-averaged equation and the steady form of the original unsteady equation shows that time-averaging generates extra terms. There are two kinds of extra terms, one is produced by the computational grid movement such as $\overline{F' dA'_x}$ and the other is produced due to the nonlinearity of the flow governing equations such as $\overline{(\rho u)' u'}$ which is similar to the Reynolds stress terms. The extra stress terms due to the velocity fluctuations are the result of nonlinearity of the flow governing equations and therefore serve to include the nonlinear interaction between the time-averaged equation and the perturbation equation. On the other hand, since the amplitude of the grid motion in a blade flutter analysis is normally very small, the extra terms produced by grid movement in the equation are assumed to be small quantity terms and are neglected in the present analysis. Therefore, the time-averaged form of the equation can be written as

$$\oiint_A \left[(\overline{F} - \overline{F_V})d\overline{A}_x + (\overline{G} - \overline{G_V})d\overline{A}_\theta + (\overline{H} - \overline{H_V})d\overline{A}_r \right] = \iiint_{\Delta V} \overline{S}d\overline{V}$$

(5.6)

The extra terms appear in the time-averaged momentum and energy equations. To solve the above time-averaged equation, extra relationships are required to make the equation closed. Nonconservative variables can be worked out from time-averaged conservative variables, for example,

$$\overline{u} = (\overline{\rho u} - \overline{\rho' u'})/\overline{\rho}$$

(5.7)

5.2   First Harmonic Perturbation Equation

Substituting the expressions (5.1), (5.3) and (5.4) into the original governing equation and then subtracting the time-averaged equation, the unsteady perturbation equation is given by

$$\frac{\partial}{\partial t} \iiint_{\Delta V} (\overline{U}dV' + U'd\overline{V}) + \oiint_A (F' - F_V')d\overline{A}_x + (G' - G_V')d\overline{A}_\theta + (H' - H_V')d\overline{A}_r$$

$$+ (\overline{F} - \overline{F_V})dA_x' + (\overline{G} - \overline{G_V})dA_\theta' + (\overline{H} - \overline{H_V})dA_r'] = \iiint_{\Delta V} (\overline{S}dV' + S'd\overline{V})$$

(5.8)

where

$$F' = \begin{pmatrix} (\rho u)' - (\rho u_g)' \\ (\overline{\rho u} - \overline{\rho u_g})u' + \left[(\rho u)' - (\rho u_g)' \right]\overline{u} + p' - \overline{(\rho u)'u'} + \overline{(\rho u_g)'u'} \\ r\left[(\overline{\rho u} - \overline{\rho u_g})v' + \left[(\rho u)' - (\rho u_g)' \right]\overline{v} - \overline{(\rho u)'v'} + \overline{(\rho u_g)'v'} \right] \\ (\overline{\rho u} - \overline{\rho u_g})w' + \left[(\rho u)' - (\rho u_g)' \right]\overline{w} - \overline{(\rho u)'w'} + \overline{(\rho u_g)'w'} \\ (\overline{\rho e} + \overline{p})u' + [(\rho e)' + p']\overline{u} - (\overline{\rho e})u_g' - (\rho e)'\overline{u_g} - \overline{p'u'} - \overline{(\rho e)'u'} + \overline{(\rho e)'u_g'} \end{pmatrix}$$

$$G' = \begin{pmatrix} (\rho v)' - (\rho v_g)' \\ (\overline{\rho v} - \overline{\rho v_g})u' + \left[(\rho v)' - (\rho v_g)' \right]\overline{u} - \overline{(\rho v)'u'} + \overline{(\rho v_g)'u'} \\ r\left[(\overline{\rho v} - \overline{\rho v_g})v' + \left[(\rho v)' - (\rho v_g)' \right]\overline{v} + p' - \overline{(\rho v)'v'} + \overline{(\rho v_g)'v'} \right] \\ (\overline{\rho v} - \overline{\rho v_g})w' + \left[(\rho v)' - (\rho v_g)' \right]\overline{w} - \overline{(\rho v)'w'} + \overline{(\rho v_g)'w'} \\ (\overline{\rho e} + \overline{p})v' + [(\rho e)' + p']\overline{v} - (\overline{\rho e})v_g' - (\rho e)'\overline{v_g} - \overline{p'v'} - \overline{(\rho e)'v'} + \overline{(\rho e)'v_g'} \end{pmatrix}$$

49

$$H' = \begin{pmatrix} (\rho w)' - (\rho w_g)' \\ \overline{(\rho w - \rho w_g)}u' + \left[(\rho w)' - (\rho w_g)'\right]\bar{u} - \overline{(\rho w)'u'} + \overline{(\rho w_g)'u'} \\ r\left[\overline{(\rho w - \rho w_g)}v' + \left[(\rho w)' - (\rho w_g)'\right]\bar{v} - \overline{(\rho w)'v'} + \overline{(\rho w_g)'v'}\right] \\ \overline{(\rho w - \rho w_g)}w' + \left[(\rho w)' - (\rho w_g)'\right]\bar{w} + p' - \overline{(\rho w)'w'} + \overline{(\rho w_g)'w'} \\ \overline{(\rho e + p)}w' + \left[(\rho e)' + p'\right]\bar{w} - \overline{(\rho e)}w_g' - \overline{(\rho e)'w_g} - \overline{p'w'} - \overline{(\rho e)'w'} + \overline{(\rho e)'w_g'} \end{pmatrix}$$

and

$$F_V' = \begin{pmatrix} 0 \\ \tau_{xx}' \\ r\tau_{x\theta}' \\ \tau_{xr}' \\ \overline{u}\tau_{xx}' + \overline{v}\tau_{x\theta}' + \overline{w}\tau_{xr}' + u'\overline{\tau_{xx}} + v'\overline{\tau_{x\theta}} + w'\overline{\tau_{xr}} - q_x' - \overline{u'\tau_{xx}'} - \overline{v'\tau_{x\theta}'} - \overline{w'\tau_{xr}'} \end{pmatrix}$$

$$G_V' = \begin{pmatrix} 0 \\ \tau_{\theta x}' \\ r\tau_{\theta\theta}' \\ \tau_{\theta r}' \\ \overline{u}\tau_{\theta x}' + \overline{v}\tau_{\theta\theta}' + \overline{w}\tau_{\theta r}' + u'\overline{\tau_{\theta x}} + v'\overline{\tau_{\theta\theta}} + w'\overline{\tau_{\theta r}} - q_\theta' - \overline{u'\tau_{\theta x}'} - \overline{v'\tau_{\theta\theta}'} - \overline{w'\tau_{\theta r}'} \end{pmatrix}$$

$$H_V' = \begin{pmatrix} 0 \\ \tau_{rx}' \\ r\tau_{r\theta}' \\ \tau_{rr}' \\ \overline{u}\tau_{rx}' + \overline{v}\tau_{r\theta}' + \overline{w}\tau_{rr}' + u'\overline{\tau_{rx}} + v'\overline{\tau_{r\theta}} + w'\overline{\tau_{rr}} - q_r' - \overline{u'\tau_{rx}'} - \overline{v'\tau_{r\theta}'} - \overline{w'\tau_{rr}'} \end{pmatrix}$$

$$S' = \begin{pmatrix} 0 \\ 0 \\ 0 \\ \left[\overline{\rho v}v' + (\rho v)'\overline{v} - \overline{(\rho v)'v'}\right]/r \\ 0 \end{pmatrix}$$

$$\tau_{xx}' = \frac{2}{3}\mu\left[2\frac{\partial u'}{\partial x} - \frac{\partial w'}{\partial r} - \frac{1}{r}\frac{\partial v'}{\partial \theta}\right] \; , \; \tau_{\theta\theta}' = \frac{2}{3}\mu\left[2\frac{1}{r}\frac{\partial v'}{\partial \theta} - \frac{\partial u'}{\partial x} - \frac{\partial w'}{\partial r}\right]$$

$$\tau'_{rr} = \frac{2}{3}\mu\left[2\frac{\partial w'}{\partial r} - \frac{1}{r}\frac{\partial v'}{\partial \theta} - \frac{\partial u'}{\partial x}\right] \quad,\quad \tau'_{x\theta} = \tau'_{\theta x} = \mu\left[\frac{\partial v'}{\partial x} + \frac{1}{r}\frac{\partial u'}{\partial \theta}\right]$$

$$\tau'_{\theta r} = \tau'_{r\theta} = \mu\left[\frac{1}{r}\frac{\partial w'}{\partial \theta} + \frac{\partial v'}{\partial r}\right] \quad,\quad \tau'_{rx} = \tau'_{xr} = \mu\left[\frac{\partial u'}{\partial r} + \frac{\partial w'}{\partial x}\right]$$

$$q'_x = -k\frac{\partial T'}{\partial x} \quad,\quad q'_\theta = -k\frac{1}{r}\frac{\partial T'}{\partial \theta} \quad,\quad q'_r = -k\frac{\partial T'}{\partial r}$$

The complete form of the unsteady perturbation equation is not readily solvable if a frequency domain approach is to be used. It is assumed that the unsteady perturbation is dominated by first order terms. Retaining only the first order terms, the resultant first order form of the fluxes can be rewritten as

$$F' = \begin{pmatrix} (\rho u)' - (\rho u_g)' \\ (\overline{\rho u} - \overline{\rho u_g})u' + \left[(\rho u)' - (\rho u_g)'\right]\overline{u} + p' \\ r\left[(\overline{\rho u} - \overline{\rho u_g})v' + \left[(\rho u)' - (\rho u_g)'\right]\overline{v}\right] \\ (\overline{\rho u} - \overline{\rho u_g})w' + \left[(\rho u)' - (\rho u_g)'\right]\overline{w} \\ (\overline{\rho e} + \overline{p})u' + \left[(\rho e)' + p'\right]\overline{u} - (\overline{\rho e})u'_g - (\rho e)'\overline{u_g} \end{pmatrix}$$

$$G' = \begin{pmatrix} (\rho v)' - (\rho v_g)' \\ (\overline{\rho v} - \overline{\rho v_g})u' + \left[(\rho v)' - (\rho v_g)'\right]\overline{u} \\ r\left[(\overline{\rho v} - \overline{\rho v_g})v' + \left[(\rho v)' - (\rho v_g)'\right]\overline{v} + p'\right] \\ (\overline{\rho v} - \overline{\rho v_g})w' + \left[(\rho v)' - (\rho v_g)'\right]\overline{w} \\ (\overline{\rho e} + \overline{p})v' + \left[(\rho e)' + p'\right]\overline{v} - (\overline{\rho e})v'_g - (\rho e)'\overline{v_g} \end{pmatrix}$$

$$H' = \begin{pmatrix} (\rho w)' - (\rho w_g)' \\ (\overline{\rho w} - \overline{\rho w_g})u' + \left[(\rho w)' - (\rho w_g)'\right]\overline{u} \\ r\left[(\overline{\rho w} - \overline{\rho w_g})v' + \left[(\rho w)' - (\rho w_g)'\right]\overline{v}\right] \\ (\overline{\rho w} - \overline{\rho w_g})w' + \left[(\rho w)' - (\rho w_g)'\right]\overline{w} + p' \\ (\overline{\rho e} + \overline{p})w' + \left[(\rho e)' + p'\right]\overline{w} - (\overline{\rho e})w'_g - (\rho e)'\overline{w_g} \end{pmatrix}$$

$$F_V' = \begin{pmatrix} 0 \\ \tau'_{xx} \\ r\tau'_{x\theta} \\ \tau'_{xr} \\ \overline{u\tau'_{xx}} + \overline{v\tau'_{x\theta}} + \overline{w\tau'_{xr}} + \overline{u'\tau_{xx}} + \overline{v'\tau_{x\theta}} + \overline{w'\tau_{xr}} - q'_x \end{pmatrix}$$

$$G_V' = \begin{pmatrix} 0 \\ \tau'_{\theta x} \\ r\tau'_{\theta\theta} \\ \tau'_{\theta r} \\ \overline{u\tau'_{\theta x}} + \overline{v\tau'_{\theta\theta}} + \overline{w\tau'_{\theta r}} + \overline{u'\tau_{\theta x}} + \overline{v'\tau_{\theta\theta}} + \overline{w'\tau_{\theta r}} - q'_\theta \end{pmatrix}$$

$$H_V' = \begin{pmatrix} 0 \\ \tau'_{rx} \\ r\tau'_{r\theta} \\ \tau'_{rr} \\ \overline{u\tau'_{rx}} + \overline{v\tau'_{r\theta}} + \overline{w\tau'_{rr}} + \overline{u'\tau_{rx}} + \overline{v'\tau_{r\theta}} + \overline{w'\tau_{rr}} - q'_r \end{pmatrix}$$

$$S' = \begin{pmatrix} 0 \\ 0 \\ 0 \\ \left[\overline{\rho v v'} + \overline{(\rho v)' v} \right] / r \\ 0 \end{pmatrix}$$

The present work considers only one periodic disturbance with the assumption that the unsteady perturbation varies in a harmonic mode in time, i.e.

$$U' = \widetilde{U} e^{i\omega t} + \widetilde{U}_- e^{-i\omega t} \tag{5.9}$$

where $\widetilde{U}$ is the vector of complex amplitudes of perturbations in the conservation variables and $\widetilde{U}_-$ is the complex conjugate of $\widetilde{U}$. The computational grid and the grid moving velocities also have similar harmonic forms.

Substituting all the harmonic expressions into the unsteady perturbation equation, the first order harmonic perturbation equation becomes

$$\oiint_A [(\tilde{F}-\tilde{F_V})d\bar{A}_x + (\tilde{G}-\tilde{G_V})d\bar{A}_\theta + (\tilde{H}-\tilde{H_V})d\bar{A}_r + (\bar{F}-\bar{F_V})d\tilde{A}_x + (\bar{G}-\bar{G_V})d\tilde{A}_\theta$$

$$+ (\bar{H}-\bar{H_V})d\tilde{A}_r] = \iiint_{\Delta V}(\bar{S}d\tilde{V}+\tilde{S}d\bar{V}) - i\omega\iiint_{\Delta V}(\bar{U}d\tilde{V}+\tilde{U}d\bar{V}) \qquad (5.10)$$

where

$$\tilde{F} = \begin{pmatrix} \widetilde{(\rho u)} - \widetilde{(\rho u_g)} \\[4pt] \overline{(\rho u - \rho u_g)}\tilde{u} + \left[\widetilde{(\rho u)} - \widetilde{(\rho u_g)}\right]\bar{u} + \tilde{p} \\[4pt] r\left[\overline{(\rho u - \rho u_g)}\tilde{v} + \left[\widetilde{(\rho u)} - \widetilde{(\rho u_g)}\right]\bar{v}\right] \\[4pt] \overline{(\rho u - \rho u_g)}\tilde{w} + \left[\widetilde{(\rho u)} - \widetilde{(\rho u_g)}\right]\bar{w} \\[4pt] \overline{(\rho e + p)}\tilde{u} + \left[\widetilde{(\rho e)} + \tilde{p}\right]\bar{u} - \overline{\rho e u_g} - \widetilde{(\rho e)u_g} \end{pmatrix}$$

$$\tilde{G} = \begin{pmatrix} \widetilde{(\rho v)} - \widetilde{(\rho v_g)} \\[4pt] \overline{(\rho v - \rho v_g)}\tilde{u} + \left[\widetilde{(\rho v)} - \widetilde{(\rho v_g)}\right]\bar{u} \\[4pt] r\left[\overline{(\rho v - \rho v_g)}\tilde{v} + \left[\widetilde{(\rho v)} - \widetilde{(\rho v_g)}\right]\bar{v} + \tilde{p}\right] \\[4pt] \overline{(\rho v - \rho v_g)}\tilde{w} + \left[\widetilde{(\rho v)} - \widetilde{(\rho v_g)}\right]\bar{w} \\[4pt] \overline{(\rho e + p)}\tilde{v} + \left[\widetilde{(\rho e)} + \tilde{p}\right]\bar{v} - \overline{\rho e v_g} - \widetilde{(\rho e)v_g} \end{pmatrix}$$

$$\tilde{H} = \begin{pmatrix} \widetilde{(\rho w)} - \widetilde{(\rho w_g)} \\[4pt] \overline{(\rho w - \rho w_g)}\tilde{u} + \left[\widetilde{(\rho w)} - \widetilde{(\rho w_g)}\right]\bar{u} \\[4pt] r\left[\overline{(\rho w - \rho w_g)}\tilde{v} + \left[\widetilde{(\rho w)} - \widetilde{(\rho w_g)}\right]\bar{v}\right] \\[4pt] \overline{(\rho w - \rho w_g)}\tilde{w} + \left[\widetilde{(\rho w)} - \widetilde{(\rho w_g)}\right]\bar{w} + \tilde{p} \\[4pt] \overline{(\rho e + p)}\tilde{w} + \left[\widetilde{(\rho e)} + \tilde{p}\right]\bar{w} - \overline{\rho e w_g} - \widetilde{(\rho e)w_g} \end{pmatrix}$$

$$\tilde{F_V} = \begin{pmatrix} 0 \\[4pt] \widetilde{\tau_{xx}} \\[4pt] r\widetilde{\tau_{x\theta}} \\[4pt] \widetilde{\tau_{xr}} \\[4pt] \bar{u}\widetilde{\tau_{xx}} + \bar{v}\widetilde{\tau_{x\theta}} + \bar{w}\widetilde{\tau_{xr}} + \tilde{u}\overline{\tau_{xx}} + \tilde{v}\overline{\tau_{x\theta}} + \tilde{w}\overline{\tau_{xr}} - \widetilde{q_x} \end{pmatrix}$$

$$\widetilde{G_V} = \begin{pmatrix} 0 \\ \widetilde{\tau_{\theta x}} \\ r\widetilde{\tau_{\theta \theta}} \\ \widetilde{\tau_{\theta r}} \\ \overline{u}\widetilde{\tau_{\theta x}} + \overline{v}\widetilde{\tau_{\theta \theta}} + \overline{w}\widetilde{\tau_{\theta r}} + \widetilde{u}\overline{\tau_{\theta x}} + \widetilde{v}\overline{\tau_{\theta \theta}} + \widetilde{w}\overline{\tau_{\theta r}} - \widetilde{q_\theta} \end{pmatrix}$$

$$\widetilde{H_V} = \begin{pmatrix} 0 \\ \widetilde{\tau_{rx}} \\ r\widetilde{\tau_{r\theta}} \\ \widetilde{\tau_{rr}} \\ \overline{u}\widetilde{\tau_{rx}} + \overline{v}\widetilde{\tau_{r\theta}} + \overline{w}\widetilde{\tau_{rr}} + \widetilde{u}\overline{\tau_{rx}} + \widetilde{v}\overline{\tau_{r\theta}} + \widetilde{w}\overline{\tau_{rr}} - \widetilde{q_r} \end{pmatrix}$$

$$\widetilde{S} = \begin{pmatrix} 0 \\ 0 \\ 0 \\ [(\widetilde{\rho v})\overline{v} + (\overline{\rho v})\widetilde{v}]/r \\ 0 \end{pmatrix}$$

The first order harmonic perturbation equation has the same form as the unsteady perturbation equation in the time-linearized method. However, the equation is quasi-linear, i.e. the perturbations are linear for a given time-averaged flow field. If the time-averaged flow is the same as the steady flow, the above first harmonic perturbation equation reduces to the conventional time-linearized perturbation equation.

5.3   Inclusion of Higher Order Harmonic Perturbations

The nonlinear harmonic approach has resulted in a first order harmonic perturbation equation that is efficient in solving cases where the extent of nonlinearity is not high. However, cases with highly nonlinear behaviour would be better predicted if the accuracy of the unsteady deterministic stress terms in the time-averaged equation could be improved. Since the unsteady deterministic stress terms in the time-averaged equation get their constituent terms updated through the interaction with the harmonic perturbation equation due to the coupled solution approach, the desired improvement can be achieved if the first harmonic perturbation conservative variables of the

54

harmonic perturbation equation are made more accurate by including higher order harmonic perturbations through a cross coupling of perturbation terms in the harmonic perturbation equation itself. This higher order cross coupling in turn improves the first harmonic perturbation conservative variables that form the unsteady stress terms in the time-averaged equation. This is achieved by a harmonic balance technique that has its origins in the field of structural dynamics.

5.3.1   Harmonic Balance Method

For simplicity, the details are first expressed in a formulation of one dimension and later extended to three dimensions.

Considering the one dimensional momentum equation,

$$\frac{\partial}{\partial t}(\rho u) + \frac{\partial}{\partial x}(\rho u \cdot u + p) - \frac{\partial}{\partial x}(\tau) = 0 \tag{5.11}$$

and assuming that the flow is composed of a time-averaged part and a harmonic perturbation part, the flow variables can be expressed as

$$u = \overline{u} + u' \tag{5.12}$$

and

$$\rho u = \overline{\rho u} + (\rho u)' \tag{5.13}$$

The pressure is also similarly decomposed. Substituting (5.12) and (5.13) into the one dimensional momentum equation (5.11) and time averaging it, we get the time-averaged equation as

$$\frac{\partial}{\partial x}(\overline{\rho u \cdot u} + \overline{(\rho u)'u'} + \overline{p}) - \frac{\partial}{\partial x}(\overline{\tau}) = 0 \tag{5.14}$$

The above time-averaged equation is the same as in nonlinear harmonic approach. Since the unsteadiness in the flow is assumed to be harmonic in time, the perturbation variable u' in equation (5.12) can be expressed as a complex Fourier series to give,

$$u' = \sum_{n=1}^{N}(\tilde{u}_n e^{in\omega t} + \tilde{u}_{-n} e^{-in\omega t}) = \tilde{u}_{-1} e^{-i\omega t} + \tilde{u}_1 e^{i\omega t} + \tilde{u}_{-2} e^{-i2\omega t} + \tilde{u}_2 e^{i2\omega t} + \ldots \tag{5.15}$$

where n is the order of harmonics, $\tilde{u}_{-n}$ is the complex conjugate of $\tilde{u}_n$ and N is the total number of perturbations to be included. Since conservation variables are real quantities, we only need to have Fourier coefficients for non-negative n. Similarly, $(\rho u)'$ in Eq. (5.13) can be expressed as

$$(\rho u)' = \sum_{n=1}^{N}((\widetilde{\rho u})_n e^{in\omega t} + (\widetilde{\rho u})_{-n} e^{-in\omega t}) = (\widetilde{\rho u})_{-1} e^{-i\omega t} + (\widetilde{\rho u})_1 e^{i\omega t} + \dots$$

$$(5.16)$$

Substituting (5.12), (5.13), (5.15) and (5.16) into the momentum equation (5.11) and collecting only the first order harmonic terms, we get the first order harmonic perturbation equation as

$$i\omega(\widetilde{\rho u})_1 + \frac{\partial}{\partial x}[(\overline{\rho u})\tilde{u}_1 + \bar{u}(\widetilde{\rho u})_1 + (\widetilde{\rho u})_2 \tilde{u}_{-1} + \tilde{u}_2(\widetilde{\rho u})_{-1} + (\widetilde{\rho u})_3 \tilde{u}_{-2}$$

$$+\tilde{u}_3(\widetilde{\rho u})_{-2} + \dots] + \frac{\partial}{\partial x}(\tilde{p}_1) - \frac{\partial}{\partial x}(\tilde{\tau}_1) = 0 \qquad (5.17)$$

The order of harmonics of each term in (5.17) is one. In the case of terms involving the product of fluctuations, the sum of the harmonics should be equal to one (e.g., $(\rho u)_3 e^{i3\omega t} \cdot u_{-2} e^{-i2\omega t}$). In this way, the harmonic balance is achieved for the entire equation. Therefore, the general form (e.g. for ω_n) of harmonic perturbation equation can be expressed as

$$i\omega(\widetilde{\rho u})_n + \frac{\partial}{\partial x}\left\{(\overline{\rho u})\tilde{u}_n + \bar{u}(\widetilde{\rho u})_n + \sum_{i+j=n}\left[(\widetilde{\rho u})_i \tilde{u}_j\right]\right\} + \frac{\partial}{\partial x}(\tilde{p}_n) - \frac{\partial}{\partial x}(\tilde{\tau}_n) = 0$$

$$(5.18)$$

where $i, j = \pm 1, 2, 3, \dots$ and n could be of any order of harmonics subject to the condition that $i + j = n$. The zeroth harmonic, $n = 0$, corresponds to the mean flow. In principle, the summation of harmonics i and j can be taken over all integer values of n. In practice, however, they are truncated to a finite number of harmonics. The equation (5.18) has a cross coupling term $\sum_{i+j=n}(\widetilde{\rho u})_i \tilde{u}_j$ that has resulted from the inclusion of higher order harmonics, which differentiates this equation from the one obtained through the nonlinear harmonic formulation. Also, the deterministic stress term in (5.14) can now be expressed as $\overline{(\rho u)'u'} = \sum_{n=1}^{N}\left[\overline{(\widetilde{\rho u})_n \tilde{u}_{-n}} + \overline{(\widetilde{\rho u})_{-n} \tilde{u}_n}\right]$. It is clear from the above that with the inclusion of higher order harmonics the accuracy of deterministic stress terms will improve as the cross coupling term in the harmonic perturbation equation helps to refine the fundamental harmonic terms in a coupled solution approach. If no higher order harmonics are considered, the first order

harmonic balance equation is essentially the same as that of the nonlinear harmonic formulation.

Extending the one-dimensional formulation to three-dimensions, the time-averaged equation is the same as equation (5.5) and the harmonic perturbation equation becomes

$$\oiint_A [(\overline{F}-\overline{F_V})d\tilde{A}_x + (\overline{G}-\overline{G_V})d\tilde{A}_\theta + (\overline{H}-\overline{H_V})d\tilde{A}_r + (\tilde{F}-\widetilde{F_V})d\overline{A}_x + (\tilde{G}-\widetilde{G_V})d\overline{A}_\theta$$

$$+ (\tilde{H}-\widetilde{H_V})d\overline{A}_r + (\tilde{F}-\widetilde{F_V})d\tilde{A}_x + (\tilde{G}-\widetilde{G_V})d\tilde{A}_\theta + (\tilde{H}-\widetilde{H_V})d\tilde{A}_r$$

$$= \iiint_{\Delta V} (\tilde{S}d\overline{V} + \overline{S}d\tilde{V} + \tilde{S}d\tilde{V}) - i\omega \iiint_{\Delta V} (\overline{U}d\tilde{V} + \tilde{U}d\overline{V} + \tilde{U}d\tilde{V}) \qquad (5.19)$$

where

$$\tilde{F} = \begin{pmatrix} \widetilde{(\rho u)}_n - \widetilde{(\rho u_g)}_n \\[2mm] (\overline{\rho u} - \overline{\rho u_g})\tilde{u}_n + \left[\widetilde{(\rho u)}_n - \widetilde{(\rho u_g)}_n \right]\overline{u} + \tilde{p}_n + \sum_{i+j=n} \left[\widetilde{(\rho u)}_i \tilde{u}_j - \widetilde{(\rho u_g)}_i \tilde{u}_j \right] \\[2mm] r\left[\widetilde{(\rho u)} - \overline{\rho u_g})\tilde{v}_n + \left[\widetilde{(\rho u)}_n - \widetilde{(\rho u_g)}_n \right]\overline{v} + \sum_{i+j=n} \left[\widetilde{(\rho u)}_i \tilde{v}_j - \widetilde{(\rho u_g)}_i \tilde{v}_j \right] \right] \\[2mm] (\overline{\rho u} - \overline{\rho u_g})\tilde{w}_n + \left[\widetilde{(\rho u)}_n - \widetilde{(\rho u_g)}_n \right]\overline{w} + \sum_{i+j=n} \left[\widetilde{(\rho u)}_i \tilde{w}_j - \widetilde{(\rho u_g)}_i \tilde{w}_j \right] \\[2mm] (\overline{\rho e} + \overline{p})\tilde{u}_n + \left[\widetilde{(\rho e)}_n + \tilde{p}_n \right]\overline{u} + \sum_{i+j=n} \left[\widetilde{(\rho e)}_i \tilde{u}_j + \tilde{p}_i \tilde{u}_j - \widetilde{(\rho e)}_i (\tilde{u}_g)_j \right] - \overline{\rho e}\widetilde{(u_g)}_n - \widetilde{(\rho e)}_n \overline{u_g} \end{pmatrix}$$

$$\tilde{G} = \begin{pmatrix} \widetilde{(\rho v)}_n - \widetilde{(\rho v_g)}_n \\[2mm] (\overline{\rho v} - \overline{\rho v_g})\tilde{u}_n + \left[\widetilde{(\rho v)}_n - \widetilde{(\rho v_g)}_n \right]\overline{u} + \sum_{i+j=n} \left[\widetilde{(\rho v)}_i \tilde{u}_j - \widetilde{(\rho v_g)}_i \tilde{u}_j \right] \\[2mm] r\left[\widetilde{(\rho v)} - \overline{\rho v_g})\tilde{v}_n + \left[\widetilde{(\rho v)}_n - \widetilde{(\rho v_g)}_n \right]\overline{v} + \tilde{p}_n + \sum_{i+j=n} \left[\widetilde{(\rho v)}_i \tilde{v}_j - \widetilde{(\rho v_g)}_i \tilde{v}_j \right] \right] \\[2mm] (\overline{\rho v} - \overline{\rho v_g})\tilde{w}_n + \left[\widetilde{(\rho v)}_n - \widetilde{(\rho v_g)}_n \right]\overline{w} + \sum_{i+j=n} \left[\widetilde{(\rho v)}_i \tilde{w}_j - \widetilde{(\rho v_g)}_i \tilde{w}_j \right] \\[2mm] (\overline{\rho e} + \overline{p})\tilde{v}_n + \left[\widetilde{(\rho e)}_n + \tilde{p}_n \right]\overline{v} + \sum_{i+j=n} \left[\widetilde{(\rho e)}_i \tilde{v}_j + \tilde{p}_i \tilde{v}_j - \widetilde{(\rho e)}_i (\tilde{v}_g)_j \right] - \overline{\rho e}\widetilde{(v_g)}_n - \widetilde{(\rho e)}_n \overline{v_g} \end{pmatrix}$$

57

$$\widetilde{H} = \begin{pmatrix} (\widetilde{\rho w})_n - (\widetilde{\rho w_g})_n \\[4pt] (\overline{\rho w} - \overline{\rho w_g})\widetilde{u}_n + \left[(\widetilde{\rho w})_n - (\widetilde{\rho w_g})_n\right]\overline{u} + \sum_{i+j=n}\left[(\widetilde{\rho w})_i \widetilde{u}_j - (\widetilde{\rho w_g})_i \widetilde{u}_j\right] \\[4pt] r\left[(\overline{\rho w}) - \overline{\rho w_g})\widetilde{v}_n + \left[(\widetilde{\rho w})_n - (\widetilde{\rho w_g})_n\right]\overline{v} + \sum_{i+j=n}\left[(\widetilde{\rho w})_i \widetilde{v}_j - (\widetilde{\rho w_g})_i \widetilde{v}_j\right]\right] \\[4pt] (\overline{\rho w} - \overline{\rho w_g})\widetilde{w}_n + \left[(\widetilde{\rho w})_n - (\widetilde{\rho w_g})_n\right]\overline{w} + \widetilde{p}_n + \sum_{i+j=n}\left[(\widetilde{\rho w})_i \widetilde{w}_j - (\widetilde{\rho w_g})_i \widetilde{w}_j\right] \\[4pt] (\overline{\rho e} + \overline{p})\widetilde{w}_n + \left[(\widetilde{\rho e})_n + \widetilde{p}_n\right]\overline{u} + \sum_{i+j=n}\left[(\widetilde{\rho e})_i \widetilde{w}_j + \widetilde{p}_i \widetilde{w}_j - (\widetilde{\rho e})_i (\widetilde{w_g})_j\right] - \overline{\rho e}(\widetilde{w_g})_n - (\widetilde{\rho e})_n \overline{w_g} \end{pmatrix}$$

$$\widetilde{F_V} = \begin{pmatrix} 0 \\[4pt] (\widetilde{\tau_{xx}})_n \\[4pt] r(\widetilde{\tau_{x\theta}})_n \\[4pt] (\widetilde{\tau_{xr}})_n \\[4pt] \overline{u}(\widetilde{\tau_{xx}})_n + \overline{v}(\widetilde{\tau_{x\theta}})_n + \overline{w}(\widetilde{\tau_{xr}})_n + \widetilde{u}_n\overline{\tau_{xx}} + \widetilde{v}_n\overline{\tau_{x\theta}} + \widetilde{w}_n\overline{\tau_{xr}} \\[4pt] + \sum_{i+j=n}\left[\widetilde{u}_i(\widetilde{\tau_{xx}})_j + \widetilde{v}_i(\widetilde{\tau_{x\theta}})_j + \widetilde{w}_i(\widetilde{\tau_{xr}})_j\right] - (\widetilde{q_x})_n \end{pmatrix}$$

$$\widetilde{G_V} = \begin{pmatrix} 0 \\[4pt] (\widetilde{\tau_{\theta x}})_n \\[4pt] r(\widetilde{\tau_{\theta\theta}})_n \\[4pt] (\widetilde{\tau_{\theta r}})_n \\[4pt] \overline{u}(\widetilde{\tau_{\theta x}})_n + \overline{v}(\widetilde{\tau_{\theta\theta}})_n + \overline{w}(\widetilde{\tau_{\theta r}})_n + \widetilde{u}_n\overline{\tau_{\theta x}} + \widetilde{v}_n\overline{\tau_{\theta\theta}} + \widetilde{w}_n\overline{\tau_{\theta r}} \\[4pt] + \sum_{i+j=n}\left[\widetilde{u}_i(\widetilde{\tau_{\theta x}})_j + \widetilde{v}_i(\widetilde{\tau_{\theta\theta}})_j + \widetilde{w}_i(\widetilde{\tau_{\theta r}})_j\right] - (\widetilde{q_\theta})_n \end{pmatrix}$$

$$\widetilde{H_V} = \begin{pmatrix} 0 \\[4pt] (\widetilde{\tau_{rx}})_n \\[4pt] r(\widetilde{\tau_{r\theta}})_n \\[4pt] (\widetilde{\tau_{rr}})_n \\[4pt] \overline{u}(\widetilde{\tau_{rx}})_n + \overline{v}(\widetilde{\tau_{r\theta}})_n + \overline{w}(\widetilde{\tau_{rr}})_n + \widetilde{u}_n\overline{\tau_{rx}} + \widetilde{v}_n\overline{\tau_{r\theta}} + \widetilde{w}_n\overline{\tau_{rr}} \\[4pt] + \sum_{i+j=n}\left[\widetilde{u}_i(\widetilde{\tau_{rx}})_j + \widetilde{v}_i(\widetilde{\tau_{r\theta}})_j + \widetilde{w}_i(\widetilde{\tau_{rr}})_j\right] - (\widetilde{q_r})_n \end{pmatrix}$$

$$\tilde{S} = \begin{pmatrix} 0 \\ 0 \\ 0 \\ \left[\overline{(\rho v)}\tilde{v}_n + \widetilde{(\rho v)}_n \bar{v} + \sum_{i+j=n} \widetilde{(\rho v)}_i \tilde{v}_j \right] \Big/ r \\ 0 \end{pmatrix}$$

The subscript n in the above fluxes denotes the order of harmonic perturbation. An examination of the fluxes indicates that in the case of inviscid fluxes, the cross coupling terms like $\sum_{i+j=n} \widetilde{(\rho u)}_i \tilde{u}_j$ appear in the momentum and energy equations while the viscous fluxes contain them only in the energy equations.

5.4 Numerical Discretization

Similar to the time-linearized method, a pseudo time (t') is introduced to make both the time-averaged equation and the harmonic perturbation equation time dependent. The modified time-averaged equation and the harmonic perturbation equation are given by

$$\frac{\partial}{\partial t'} \iiint_{\Delta V} (\bar{U} d\bar{V}) + \oiint_A [(\bar{F} - \bar{F}_V) d\bar{A}_x + (\bar{G} - \bar{G}_V) d\bar{A}_\theta + (\bar{H} - \bar{H}_V) d\bar{A}_r] = \iiint_{\Delta V} \bar{S} d\bar{V}$$

(5.20)

$$\frac{\partial}{\partial t'} \iiint_{\Delta V} (\tilde{U} d\bar{V}) + \oiint_A [(\bar{F} - \bar{F}_V) d\tilde{A}_x + (\bar{G} - \bar{G}_V) d\tilde{A}_\theta + (\bar{H} - \bar{H}_V) d\tilde{A}_r + (\tilde{F} - \tilde{F}_V) d\bar{A}_x$$
$$+ (\tilde{G} - \tilde{G}_V) d\bar{A}_\theta + (\tilde{H} - \tilde{H}_V) d\bar{A}_r + (\tilde{F} - \tilde{F}_V) d\tilde{A}_x + (\tilde{G} - \tilde{G}_V) d\tilde{A}_\theta + (\tilde{H} - \tilde{H}_V) d\tilde{A}_r$$
$$= \iiint_{\Delta V} (\tilde{S} d\bar{V} + \bar{S} d\tilde{V} + \tilde{S} d\tilde{V}) - i\omega \iiint_{\Delta V} (\bar{U} d\tilde{V} + \tilde{U} d\bar{V} + \tilde{U} d\tilde{V})$$

(5.21)

Now both the time-averaged equation and the harmonic perturbation equation are hyperbolic in a pseudo time domain. They can be solved by any time-marching integration schemes. The cell centred finite volume scheme is used again to discretize both the time-averaged and harmonic perturbation equations spatially. A second and fourth order adaptive smoothing is used to suppress numerical oscillation. The semi-discrete forms of the time-averaged equation and the harmonic perturbation equation are in similar forms as equations (4.10) and (4.11) in the time-linearized method. However, the pressure sensor in the artificial smoothing terms as shown in (4.19) is a

59

nonlinear term and its nonlinearity cannot be ignored in cases with strong nonlinear effects. Therefore, it is desirable to linearize the pressure sensor. Since an accurate way to linearize the pressure sensor is not easy to achieve, an approximate approach is used to partially linearize the pressure sensor (He and Ning, 1998). The modified form of the pressure sensor is given by

$$\theta_{ijk} = \left| \frac{\overline{p}_{i-1,j,k} - 2\overline{p}_{i,j,k} + \overline{p}_{i+1,j,k}}{\overline{p}_{i-1,j,k} + 2\overline{p}_{i,j,k} + \overline{p}_{i+1,j,k}} \right| + 0.5 \left| \frac{\tilde{p}_{i+1,j,k} - 2\tilde{p}_{i,j,k} + \tilde{p}_{i-1,j,k}}{\overline{p}_{i+1,j,k} + 2\overline{p}_{i,j,k} + \overline{p}_{i+1,j,k}} \right| \qquad (5.22)$$

The modified pressure sensor is proportional to the local unsteadiness and the time-averaged effects of the nonlinear behaviour of pressure sensor can be included.

5.5   Coupling Between Time-Averaged Flow and Unsteady Perturbation

In order to close the time-averaged equation, extra relationships are needed. For a periodically unsteady flow, these terms can be directly evaluated in terms of the unsteady perturbations. For example, u' and v' are two unsteady quantities changing in the harmonic form, i.e.

$$u' = \sum_{n=1}^{N} (\tilde{u}_n e^{in\omega t} + \tilde{u}_{-n} e^{-in\omega t}) \qquad (5.23)$$

and

$$v' = \sum_{n=1}^{N} (\tilde{v}_n e^{in\omega t} + \tilde{v}_{-n} e^{-in\omega t}) \qquad (5.24)$$

Time-averaging the product $u'v'$ gives the deterministic stress

$$\overline{u'v'} = 2 \sum_{n=1}^{N} \left[\overline{\tilde{u}_n \tilde{v}_{-n}} + \overline{\tilde{u}_{-n} \tilde{v}_n} \right] \qquad (5.25)$$

By using the relationship (5.25), the extra terms in the time-averaged equation (5.20) can be worked out if the unsteady perturbations are already known. The unsteady perturbations are obtained by solving the harmonic perturbation equation whose coefficients are formed from the solution of the time-averaged equation. Therefore, the time-averaged equation and the harmonic perturbation equation interact with each other. Because of this interaction, these two equations cannot be solved separately and a coupling procedure has to be used. The time-averaged equation and the harmonic

perturbation equation have to be solved simultaneously. A strong coupling technique proposed by He (1994) is used to time-march the time-averaged flow field and the unsteady perturbations. This strong coupling procedure is illustrated in Fig. 5.1. This strong coupling procedure provides high stability that is particularly useful when the interaction between time-averaged flow and unsteady perturbations becomes strong.

For the pseudo-time time integration of both the time-averaged equation and the harmonic perturbation equation, the four-stage Runge-Kutta time-marching scheme is used. The boundary conditions are the same as those applied in the time-linearized method and the only difference is that the steady flow variables in the boundary conditions are replaced by time-averaged variables.

In this chapter, the complete three-dimensional formulation for the nonlinear harmonic method for the Reynolds averaged Navier-Stokes equations is presented. In addition, the inclusion of higher order harmonics to the basic nonlinear harmonic method through harmonic balancing has also been presented for the three-dimensional Reynolds-averaged Navier-Stokes equations. When compared to the time-linearized method there are some distinctive features of the nonlinear harmonic method that needs to be mentioned. In this method, the unsteady flow is divided into a time-averaged part and a perturbation part and the time-averaging brings in extra stress terms that account for the nonlinear behaviour. Then the time-averaged equation and the harmonic perturbation equation are solved using a strong coupling method that facilitates the updating of the unsteady stress terms. Also, the pressure sensor in the smoothing terms is suitably linearized to include the time-averaged effects of the nonlinear behaviour of the pressure sensor. Though the coupling procedure solves both the time-averaged and the first order perturbation equations simultaneously, the scheme is computationally more efficient compared to the nonlinear time-marching method while including nonlinear effects. The inclusion of higher order harmonics through cross coupling raises the computational effort compared to the solution of the first order perturbation equation alone but the computational efficiency is still considerably higher than the nonlinear time-marching method.

Chapter 6

Two-Dimensional Results and Discussion

A three-dimensional Navier-Stokes solver incorporating the time-linearized method and nonlinear harmonic method has been developed for unsteady flows in turbomachinery. This has to be validated against a series of test cases to demonstrate the efficiency of the frequency domain approach. However, since validation of three dimensional unsteady flows is particularly difficult due to lack of experimental data, the basic methods are first validated by computing two-dimensional inviscid and viscous test cases. The validation consists of linear test cases for blade flutter and forced response problems and nonlinear test cases for transonic flow in a diverging channel and transonic flow through an axial flow fan. Depending on the test case considered, the calculated results will be compared with results from any one of these three sources; numerical results produced by well-developed linear theories, nonlinear time-marching method and experimental data.

6.1   Oscillating Flat Plate Cascade

The basic time-linearized method is validated by computing the unsteady inviscid flows around an oscillating flat plate cascade. The specifications of this cascade is

    Chord   = 0.1 m

    Solidity (Chord/Pitch) = 1.0

    Stagger angle   = 45°

The flow has a Mach number of 0.7 at zero incidence.

The unsteady flows are introduced by the blade oscillation in a bending mode normal to the chord with an amplitude equivalent to 1% of the chord for four inter-blade phase angles of 90^{0}, 180^{0}, -90^{0} and 0^{0}. The unsteady flows are also computed for blade oscillation in torsion mode around the blade leading edge with 1 degree amplitude for the four above-mentioned inter-blade phase angles. The calculations for both the bending and torsion modes were carried out for a reduced frequency, based on blade chord and flow inlet velocity, of 1.0.

The unsteady pressure jump coefficient is defined by

$$\widetilde{c}_p = \frac{\Delta \widetilde{p}}{0.5 \widehat{\rho}_{inl} \widehat{u}_{rel}^2 A_m} = \frac{(\widetilde{p})^l - (\widetilde{p})^u}{0.5 \widehat{\rho}_{inl} \widehat{u}_{rel}^2 A_m} \qquad (6.1)$$

where A_m is the non-dimensionalized amplitude of blade motion, and the superscript "u" represents the upper surface of a reference blade and "l" refers to the blade lower surface.

Fig. 6.1 through Fig. 6.4 show the real (in-phase) and imaginary (out-of-phase) parts of the calculated unsteady pressure jump coefficient plotted against nondimensionalised blade chord. The calculated values are compared to those generated by the linear analytical solver LINSUB. The programme LINSUB was developed by Whitehead (1987) based on a semi-analytical linear method and it can handle several kinds of turbomachinery unsteady flows in a flat plate cascade induced by blade oscillation, incoming wakes and inlet or outlet pressure disturbances. The comparison between the calculated values obtained by the present solver and those obtained by LINSUB is good.

Figs. 6.5 and 6.6 show the real and imaginary parts of the calculated force and moment coefficients at different inter-blade phase angles for bending and torsion modes of oscillation. Also shown are the corresponding values obtained from LINSUB. For the bending mode, the imaginary parts of force and moment coefficients agree well with the values from LINSUB while the real parts show some discrepancy for the phase 180°. On the other hand, in the case of torsion, the imaginary parts of force and moment coefficients show a higher value for 180°. The solution from LINSUB is based upon the distribution of a vorticity sheet along the flat plate cascade that satisfies the inviscid boundary condition that there is no relative flow normal to the flat plate. The resulting integral equation is solved computationally in LINSUB, but the solution can be obtained so accurately that for test purposes it may be considered to be an exact analytic solution. The present calculation, on the other hand, uses unsteady boundary conditions in different ways. For unsteadiness due to blade vibration, the grid nodes on the blade move with the blade, and this produces extra flux terms due to grid movement that is taken account of in the formulation. In the case of wake/blade row interaction, the velocity profile of the wake coming into the blade row is specified. In the case of unsteadiness due to static

pressure fluctuations at the exit, a sinusoidal variation is assumed. In all these cases, the boundary conditions are formulated in a non-reflecting manner, to ensure that outgoing pressure and vorticity waves do not produce artificial reflections at the inlet and outlet boundaries. This difference in the treatment between the analytical method and the present numerical method could be the reason for the discrepancies observed. A reasonably good comparison for the force and moment coefficients is an indication that any computation of aerodynamic damping based on these parameters is reliable. This information is useful to the turbomachine designer for judging the aeroelastic behaviour of a specific cascade.

6.2   High Frequency Incoming Wakes

In order to assess the ability of the present time-linearized method to handle forced response problems in turbomachinery, the unsteady inviscid flows around a flat plate cascade induced by high frequency unsteady incoming wakes have been calculated. In this case, the geometrical parameters of the cascade are:

Chord $= 0.1 \text{m}$

Solidity $= 2.0$

Stagger angle $= 30°$

The inlet flow has a Mach number of 0.7 and flow angle of 30°. The unsteady incoming wake has a pitch that is 90% of the blade pitch and the corresponding reduced frequency, based on axial velocity and axial chord, is 13.96 for an inter-blade phase angle of -400°, corresponding to an incident wake to blade count ratio of 10/9.

The wake in this calculation is prescribed by assuming a uniform static pressure, uniform total enthalpy and a simple sinusoidal form of velocity defect across the wake, so the unsteady perturbation amplitude of the incoming wake can be given by

$$\tilde{p} = 0.0$$

$$\tilde{u} = A_m \sqrt{\hat{u}_{inl}^2 + \hat{v}_{inl}^2} \, \cos(\beta_{wake})$$

$$\tilde{v} = A_m \sqrt{\hat{u}_{inl}^2 + \hat{v}_{inl}^2} \, \sin(\beta_{wake})$$

where β_{wake} is the angle of the incoming wake and has a value of -30° in this calculation. A_m is the amplitude of the wake velocity defect and has a value of 1%.

The amplitude of the wake density, $\tilde{\rho}_{inl}$, can be worked out by linearizing the following nonlinear relationship

$$\tilde{\rho}_{inl} = \frac{\gamma}{\gamma-1} \frac{p_{inl}}{\left(C_p T^*_{inl} - \frac{1}{2}u^2_{inl} + v^2_{inl}\right)} \tag{6.2}$$

where T^*_{inl} is the inlet total temperature and is constant in the wake frame. For the wake in this calculation, $\tilde{\rho}_{inl}$ is given by

$$\tilde{\rho}_{inl} = \frac{\gamma}{\gamma-1} \frac{\hat{p}_{inl}}{C_p \hat{T}_{inl}} (\hat{u}_{inl}\tilde{u}_{inl} + \hat{v}_{inl}\tilde{v}_{inl}) \tag{6.3}$$

where C_p is the gas constant and γ is the ratio of specific heats.

The unsteady pressure coefficient jump in this case is defined by

$$\tilde{c}_p = \frac{\Delta\tilde{p}}{\hat{\rho}\hat{u}_{rel}\tilde{u}_{ref}} \tag{6.4}$$

where $\tilde{u}_{ref}$ is the velocity perturbation which would be induced at the leading edge of the blade by inlet wakes, if the cascade were removed.

In order to resolve the high frequency (short wave length) unsteadiness, a fine mesh with a size of 400×50 is used in this calculation. Fig. 6.7 provides the comparison of unsteady pressure coefficient jump between values calculated by the present code and those obtained by LINSUB. For an unsteady flow with a very high frequency, the comparison is good. A contour map of the first harmonic entropy is presented in Fig. 6.8 clearly indicating the propagation of the incoming wake downstream. Fig. 6.9 shows the contour map of first harmonic pressure. There are no obvious indications of reflections from the outgoing pressure waves at the inlet boundary and this shows the effectiveness of the non-reflecting boundary conditions. There are however a few reflections at the exit boundary but they are not of a serious nature to affect the numerical solution. The computation was repeated by doubling the mesh size to 800×100 in order to ensure that the calculation was not mesh dependent and the results obtained were identical to those obtained with the original mesh.

6.3 Oscillating Turbine Cascade (Fourth Standard Configuration)

The fourth standard configuration represents a typical section of the modern free standing turbine blades. This type of aerofoil has relatively high blade thickness and camber and operates under high subsonic flow conditions. This configuration was presented as part of a series of unsteady aeroelastic experimental results at the Aeroelasticity Workshop (Bolcs and Fransson, 1986). A total of ten standard configurations along with their experimental data have so far been made available as part of an aeroelastic experimental project at the Lausanne Institute of Technology. For each configuration, different numerical methods were used to calculate the unsteady flows and the numerical results were compared with the experimental data.

In this case, the turbine cascade is oscillated in a bending mode with a vibration frequency of 150Hz for different inter-blade phase angles. The cascade in this experiment is an annular turbine cascade facility that did not rotate. Instead, inlet guide vanes were used to introduce swirl in the flow to produce the required inlet flow angles. The cascade configuration consists of 20 prismatic blades with the following specifications:

Chord	= 0.0744m
Span	= 0.040m
Stagger angle	= 56.6°
Hub-tip ratio	= 0.8
Thickness-to-chord ratio	= 0.17
Pitch-to-chord ratio	= 0.76 (midspan)

In order to produce two-dimensional results, the blade profile is treated as same from hub to tip as that of the midspan section. The test case considered for the present numerical study has the following flow conditions:

Inlet flow angle	$\beta_1 = 45.0°$
Inlet Mach number	$M_1 = 0.28$
Outlet flow angle	$\beta_2 = -71.0°$
Outlet Mach number	$M_{2is} = 0.90$

The computation of inviscid flow through the cascade is performed by first calculating the steady flow and Fig. 6.10 shows a good comparison of isentropic Mach number distribution between the calculated and the experimental data. The steady flow results are seen to be in good agreement with the experimental data. Having calculated the steady flow, the unsteady flow due to blade bending in a direction nearly perpendicular to the chord is computed by solving the time-linearized perturbation equations. The reduced frequency for the blade oscillation is 0.12 and the unsteady flow was calculated for four different inter-blade phase angles, -90°, 90°, 180° and 0°.

The predicted amplitudes and phase angles of unsteady pressure coefficients on the blade surface for the four inter-blade phase angles are compared with the experimental data in Fig. 6.11 to Fig.6.14. Towards the trailing edge both experiment and calculation show an increase in the unsteady pressure amplitude on the pressure surface for all the inter-blade phase angles except for 0°. Also, the calculation predicts higher pressure values for the forward 30% of the blade for all the inter-blade phase angles except for 0°. However, the phase predictions are reasonable except for the case of 0° inter-blade phase angle in Fig. 6.14 where the amplitude of the unsteady pressure is very small leading to the large degree of uncertainty in the phase angle predictions. The agreement between the present calculations and experimental results, while not exact, shows the correct trends. There are no apparent three-dimensional effects, and this should not be surprising since the experiment was designed to produce essentially two-dimensional results. The predicted results by the time-linearized method are however very similar to those produced by a nonlinear time-marching method (He, 1990).

Fig. 6.15 presents the computed values of aerodynamic damping coefficients compared with the experimentally obtained data plotted against inter-blade phase angle. It is seen that the shape of the aerodynamic damping coefficient versus the interblade phase angle is similar for both calculation and experiment. The maximum damping value has been reached by the calculation at the same inter-blade phase angle as that of the experiment. A negative value for the aerodynamic damping is an indication of instability and the cascade configuration shows instability at the inter-blade phase angle of $-90^{\circ}$and the computation captures this well. The calculation

predicts higher values of the damping coefficient than the experiment for all the inter-blade phase angles and this is consistent with the over prediction of surface pressures seen in Figs. 6.11 through 6.13.

6.4   Inviscid Transonic Unsteady Channel Flow

The test cases presented so far have been predicted using the time-linearized method as all these cases are linear in nature and do not show any nonlinear behaviour. However, the linear harmonic method is not sufficient to validate cases exhibiting nonlinearity and for such cases the nonlinear harmonic method is used for validation. Where nonlinearity is appreciable, higher order harmonics are included in the computation of nonlinear harmonic method. The test case of unsteady inviscid transonic flow through a diverging channel demonstrates the applicability of the nonlinear harmonic method in predicting nonlinearity associated with large amplitudes of shock oscillation. The unsteady flow in this case is computed using all three methods viz. the time-linearized method, the nonlinear harmonic method and the nonlinear time-marching method. Since among all the computational approaches available for predicting unsteady nonlinear flows the nonlinear time-marching method is known for its accuracy, calculations performed using the nonlinear time-marching method are taken as the benchmark to compare the performances of the time-linearized and nonlinear harmonic methods.

The test case considered is a diverging channel of height A, and its distribution along the axial direction is given by

$$A(x) = A_{inlet} \left\{ 1.10313 + 0.10313 \tanh\left[10\left(x - \frac{1}{2} \right)\right] \right\} \tag{6.5}$$

where $0 \leq x \leq 1$ for any consistent set of units.

The flow at the beginning of the diverging section is supersonic with a Mach number of 1.093. The ratio between the exit back pressure, p_{exit}, and the inlet total pressure, P_0, is 0.7422, so that the supersonic flow is terminated by a normal shock around the location of $x = 0.5$. The computational mesh has 250×20 nodes. The unsteady flow is introduced by a fluctuation of the back pressure at the channel exit in a harmonic form given by

$$p_{exit} = \overline{p}_{exit}(1 + A_m \sin \omega t) \qquad\qquad (6.6)$$

where A_m is the amplitude of the back pressure fluctuation and $\overline{p}_{exit}$ is the steady value of back pressure in the time-linearized analysis and time-averaged value in the nonlinear harmonic analysis. In order to demonstrate increasing levels of nonlinearity, three different values of 7%, 10% and 15% of the back pressure amplitude A_m , are considered for all the calculations. The reduced frequency based on the inlet velocity and the channel inlet height is 0.63.

With the amplitude of back pressure fluctuation kept at 7%, first the unsteady flow is calculated by the nonlinear time-marching method and the unsteady pressure is time-averaged. The nonlinear effect in the unsteady flow is represented by the difference between the steady flow and time-averaged flow. Fig. 6.16 gives the comparison of pressure distribution along the channel wall for steady flow and time-averaged flow. The nonlinear effect in this case is significant and this is evident from the difference in the time-averaged flow around the shock position. The time-averaged shock is smeared due to the large amplitude of shock oscillation.

The unsteady flow calculation is then performed using the nonlinear harmonic method. The time-averaged pressure distribution from the nonlinear harmonic method is also plotted in Fig. 6.16 and it shows this method is able to capture the nonlinearity associated with the shock oscillation well. However, with just a single harmonic, the time-averaged shock from nonlinear harmonic method is excessively smeared compared to the distribution obtained from the nonlinear time-marching method. In order to improve the accuracy and bring the nonlinear harmonic method on a par with the nonlinear time-marching method, higher order harmonics are included and the calculation performed with three orders of harmonics. This inclusion of higher order harmonics provides a cross coupling as explained in chapter 5, and this in turn improves the fundamental harmonic of the basic nonlinear harmonic method resulting in the improved accuracy of the time-averaged value. It is clear from Fig. 6.16 that with just three orders of harmonics the prediction by nonlinear harmonic method matches very well with that of the nonlinear time-marching method. The upper and lower limit of the x-axis scale in Fig. 6.16 is kept as close as possible to demonstrate the extent of nonlinearity in this case and the ability of the nonlinear harmonic method

to capture this effect. The calculations are repeated with five orders of harmonics to ensure that the results are consistent. As expected, there is hardly any difference in the results between three and five orders of harmonics.

Fig. 6.17 shows the real and imaginary parts of the first harmonic unsteady pressure coefficient produced by the nonlinear harmonic method compared with that of the linear harmonic method. The unsteady pressure coefficient is defined by

$$\widetilde{c}_p = \frac{\widetilde{p}}{p_{exit} A_m} \qquad (6.7)$$

In the case of the nonlinear time-marching method, the unsteady results are Fourier transformed to get the first harmonic complex amplitudes of unsteady pressure coefficients. This comparison proves that because the unsteady perturbation in the linear harmonic method is based on the steady flow field, the predicted unsteady shock impulse by the linear analysis is much higher and narrower than that predicted by the nonlinear time-marching and nonlinear harmonic methods. On the other hand, the predicted value from the nonlinear harmonic method matches very closely to that of the nonlinear time-marching method. While the artificial smoothing is mainly responsible for smearing of the shock in the case of linear harmonic method (Lindquist and Giles, 1994), the unsteadiness due to the shock oscillation is the reason for the smearing of the shock in nonlinear harmonic method. That the nonlinear effects are substantial can be further confirmed by looking at the magnitude of second harmonic unsteady pressures, and Fig. 6.18 gives the plot of second harmonic unsteady pressure for the nonlinear time-marching and the nonlinear harmonic methods. The magnitude of the second harmonic unsteady pressure is nearly half that of the first harmonic values and this confirms the extent of nonlinear effects. Also, the good comparison between the predicted values validates the inclusion of cross coupling for higher harmonics in the nonlinear harmonic method.

Next, the amplitude of the back pressure fluctuation is increased to 10% and the calculations are carried out for all the three methods. Fig. 6.19 shows the comparison of pressure distribution for steady and time-averaged flow. In this case, the shock is oscillating at much larger amplitude along the channel compared to the case of 7% and this is evident from the time-averaged pressure distribution of nonlinear time-

marching method. As far as the nonlinear harmonic method is concerned, with such higher amplitudes, even three orders of harmonics are not sufficient to predict the correct trend and it takes five orders of harmonics to match the prediction of nonlinear time-marching method. The computation is performed with seven orders to make sure that the higher order cross coupling is still robust and the solution converges, even though there is no difference in the solutions between five and seven orders of harmonics.

Fig. 6.20 gives the first harmonic unsteady pressure coefficient distribution for 10% amplitude. As expected, the shock impulse is wider than the case of 7% and the prediction from the time-linearized method is still narrower compared to the nonlinear time-marching method. Here again the nonlinear harmonic method matches closely with the prediction of the nonlinear time-marching method. The second harmonic unsteady pressure coefficients plotted in Fig. 6.21 confirm that the nonlinear effects are significant at this amplitude of downstream disturbances.

The back pressure fluctuation is now increased to 15% and the calculations are again performed for all the three methods. The time-averaged flow values from the nonlinear time-marching method plotted in Fig. 6.22 show that the shock oscillation now covers 15% of the entire channel length. In this case, the nonlinear harmonic method requires at least seven harmonics to predict a similar behaviour and three or five orders of harmonics fail to give any reasonable prediction. Fig. 6.23 and Fig. 6.24 give the first and second harmonic unsteady pressure coefficients and the width of the shock impulse to the extent of 15% of the channel length is very evident from these values.

This test case of transonic unsteady flows in a diverging channel has shown that the nonlinear harmonic method can predict unsteady nonlinear effects remarkably well if the nonlinear effects are not too high. Compared to the time-linearized method, the prediction by the nonlinear harmonic method is a significant improvement for cases involving nonlinear effects. The basic nonlinear harmonic method itself is able to predict moderate nonlinear effects as seen in the case of 7% back pressure amplitude and the inclusion of cross coupling of higher order perturbations further improves the prediction capability significantly.

6.5 Inlet Distortion Through a Transonic Axial Flow Fan Rotor

In order to validate the effectiveness of the nonlinear harmonic method for unsteady viscous flows, a test case of NASA-67 transonic axial flow fan rotor subjected to forced response at the inlet in the form of total pressure variations is considered here. The rotor has 22 blades and an aspect ratio of 1.56 (based on average span/root axial chord). The rotor solidity varies from 3.114 at the hub to 1.29 at the tip. The design rotational speed is 16043 rpm, which yields a tip speed of 429 m/sec and an inlet tip relative Mach number of 1.38. The rotor design pressure ratio is 1.63 at a mass flow of 33.25 kg/sec. The configuration and other specifications of the rotor are given in the AGARD report by Wood et.al. (1990). The steady flow calculations for the solver for this case have already been validated by three-dimensional calculations performed by Li and He (2002).

The computations are performed for a rotational speed of 16043 rpm. The representative blade section used in this computation is at 70% from the hub. Inlet total pressure distortions stationary in the absolute frame of reference are introduced. The circumferential length scale (and therefore frequency) considered here is that of 267.38Hz with an inter-blade phase angle of -16.37°. The case of total pressure distortion with 10% of the mean value is considered here. A computational grid of 110×25 is used for the present calculations. The computed values from the nonlinear time-marching method are used as the benchmark in this case for comparing the predictions from the nonlinear harmonic method and the linear harmonic method.

First, the computation is performed the using the nonlinear time-marching method with 10% distortion amplitude of inlet total pressure for a frequency of 267.38Hz and inter-blade phase angle of -16.37°. At this frequency, the distortion pattern covers the entire annulus, and all 22 blade passages encompass one period of the inlet distortion. Therefore, the nonlinear time-marching solution has to be performed for 22 passages. The unsteady results are then Fourier transformed to get the amplitude and phase of the unsteady pressure and velocity components at the inlet. These values are then used as input for the nonlinear harmonic and linear harmonic methods. For the nonlinear harmonic and linear harmonic methods the computation can however be performed over a single passage domain.

72

Fig. 6.25 gives the comparison of blade surface pressure distribution for steady flow and time-averaged flow. The static pressures are normalized with inlet mean stagnation pressure. In this case, the nonlinear time-marching method shows a slight forward shift around the mean shock position for both suction and pressure surfaces indicating some nonlinear effect. The nonlinear harmonic method, while showing the correct trend, predicts larger shift around the mean shock position.

The amplitude and phase of unsteady pressure fluctuations on suction and pressure surfaces are compared in Fig. 6.26 and 6.27. The unsteady pressure is normalized by the product of inlet mean dynamic pressure and the distortion amplitude. The amplitude of unsteady pressures on suction and pressure surfaces in Fig. 6.26 shows that the nonlinear time-marching method gives an indication of viscous displacement effects tending to weaken and distribute impulsive unsteady loads associated with shock motion. However, both linear and nonlinear harmonic methods predict higher loads than the nonlinear time-marching method and do not exhibit any significant viscous displacement effects. It can also be seen that the phase angles from the numerical prediction by nonlinear harmonic method and linear harmonic method in Fig. 6.27 do not really show the correct trend. Any attempt to improve the solution by including higher order harmonics in the nonlinear harmonic method results in the solution diverging.

The over prediction of nonlinear effect by the nonlinear harmonic method is not due to the severity of the long wavelength distortion pattern considered above and this is confirmed by performing the computation for a short wavelength, high frequency distortion pattern covering only 5 passages of the total 22 passages. In this case, the distortion frequency is 1069.5 Hz with an inter-blade phase angle of -72.0° and the amplitude of distortion is 10%. The nonlinear time-marching calculations are carried out for 5 passages. Here the time-averaged pressure distribution from nonlinear time-marching method in Fig. 6.28 is only very slightly different from the steady flow on suction and pressure surfaces indicating that the nonlinear effects in this case are not appreciable. But the nonlinear harmonic method gives considerably different time-averaged values especially on the suction surface. The amplitudes of the unsteady pressures shown in Fig. 6.29 are higher for the nonlinear harmonic and linear

73

harmonic methods compared to the nonlinear time-marching method and this is similar to what has been observed for the long wavelength, low frequency distortion case. The phase angle predictions in Fig. 6.30 once again do not show the correct trend.

The above analysis indicates that the nonlinear harmonic method tries to pick up nonlinear effects but as the solution progresses the nonlinearity seems to get amplified through the interaction between the time-averaged equations and the harmonic perturbation equations. The wrong trend in the phase angle predictions seem to suggest that the solution behaviour is not reliable. Considerable length of time was spent on this particular test case trying out several options, in an attempt to understand the solution behaviour. It should be noted that the nonlinear harmonic method including the higher order cross coupling performed very well in the inviscid transonic channel case described in section 6.4, picking up nonlinearity associated with large amplitude shock oscillations. This indicates that in the case of viscous unsteady flows, as in the present case, the viscous stresses in the energy equation that contain time-averaged extra terms might be the reason for this amplification of nonlinearity as the nonlinear effect is conveyed through these time-averaged terms. Linearizing the turbulence model may remove this problem. Also, the numerical smoothing seems to affect the solution in a way since the pressure sensor has been linearized only in an approximate way.

Finally, even though not much significance can be attached to details of computational efficiency in a test case like this, a comparison among the methods provides an approximate measure of the computational cost involved in a practical unsteady problem. The nonlinear harmonic method takes 3.5 times the CPU time per iteration of the steady flow solver while linear harmonic method takes 2 times that of the steady flow solver. As far as the nonlinear time-marching method is concerned, since multiple passage solutions are required for a problem of this nature, even though a single iteration for a single passage takes only 1.4 times the CPU time per iteration of the steady flow solver, for a 22 passage solution that amounts to 31 times the cost per iteration of the steady flow solver. This is approximately 9 times more expensive than the nonlinear harmonic method.

Chapter 7

Three-Dimensional Results and Discussion

Predictions of three-dimensional unsteady flows in turbomachinery in the frequency domain have so far been restricted to only inviscid Euler solutions. The present work, therefore, focuses on the calculation of three-dimensional unsteady viscous flows in turbomachinery, with specific attention to blade flutter predictions. When it comes to validation of three-dimensional unsteady flows, the task is made particularly difficult since three-dimensional unsteady experimental data are currently hardly available in the published literature. Therefore, comparisons between numerical predictions and solutions from analytical or semi-analytical linear theories for simple cascade geometries for inviscid flow condition play an essential part in validations of three-dimensional unsteady solution methods. The present validation programme considers two test cases, an inviscid case to validate the three-dimensional Euler solution where the results are compared with solutions from a semi-analytical theory and a viscous case to validate the three-dimensional Navier-Stokes solution where the results compared with measurements from an ongoing experimental investigation at the University of Durham.

7.1   Validation of Three-Dimensional Euler Solution

This test case was originally proposed by He and Denton (1994). The geometry is of a simple linear flat plate cascade placed between two parallel solid walls. The cascade geometry has the following specifications:

Chord	C=0.1m
Stagger angle	$\gamma = 45^{\circ}$
Pitch/Chord ratio	P/C=1.0
Span/Chord ratio	S/C=3.0

The inlet flow Mach number is 0.7 and the incidence is zero. Hence, the mean flow through the cascade is uniform. The blades are oscillated in a three-dimensional mode. Each two-dimensional section is subject to torsion mode around its leading edge. The torsion amplitude is linearly varied along the span. At the hub section the amplitude is

0 and at the tip, the amplitude is 1°. The blades vibrate with a reduced frequency of 1.0, based on chord and upstream velocity. Two inter-blade phase angles, 0° and 180° are considered.

For flat plate cascade geometries at zero incidence flow condition, time-linearized semi analytical theories are known to provide accurate solutions. The results of the present calculations are compared with the solutions from the three-dimensional semi-analytical lifting surface method developed by Namba (1977,1983), who provided his results for this case (Namba, 1991).

The mesh size for the present calculations is $161 \times 41 \times 41$ in the streamwise, pitchwise and radial directions, respectively. Computed unsteady pressure difference across the blade surface at each two-dimensional section is presented in the form of unsteady pressure jump coefficient defined by

$$\tilde{c}_p = \frac{\Delta \tilde{p}}{0.5 \hat{\rho}_{inlet} \hat{U}_{inlet}^2 A_m} \quad (7.1)$$

where $\Delta \tilde{p}$ is the first harmonic pressure jump across the blade and A_m is the torsion amplitude at the tip in radians. The results are presented for spanwise positions of 0%, 20%, 40%, 60%, 80% and 100%. Fig. 7.1 and Fig. 7.2 show the real and imaginary parts of the unsteady pressure jump coefficients at six spanwise sections (R/S, where R is the radial distance measured form the hub) in comparison with Namba's semi-analytical results for inter-blade phase angle 0°. Fig. 7.3 and Fig. 7.4 show the corresponding results for inter-blade phase angle 180°. In order to make sure that the computations were mesh independent, the calculations were repeated by halving the mesh size to $81 \times 21 \times 21$ in the streamwise, pitchwise and radial directions and the results were found to be nearly identical. Fig. 7.4a and Fig. 7.4b show results for inter-blade phase angle of 180° for both fine and coarse meshes for all spanwise positions.

The computed results for both inter-blade phase angles show in general, a good agreement with Namba's results. There are some discrepancies at the leading edge and this stems from the numerical diffusion associated with the central difference spatial discretization of the present solver. Also, total moment coefficients for these

two phase angles are also calculated and the computed values are shown along with those provided by Namba in Fig. 7.5. The agreement between real parts is good for both phase angles and while the imaginary parts match well for $0°$, the calculation over predicts for $180°$. The reason for this difference is not known as the pressure jump predictions are reasonably good. In Namba's method based on lifting surface theory, the upwash velocity is expressed by integrating the linearized equation of motion and the flow tangency condition is obtained through an integral equation for the lifting pressure. As explained in section 6.1, the difference in the treatment of boundary conditions between the present numerical method and that of Namba could be the reason for the discrepancies. These results demonstrate the capability of the three-dimensional time-linearized Euler analysis in the frequency domain to model unsteady flows due to three-dimensional vibratory motions.

7.2   Unsteady Viscous Flow Through an Oscillating Compressor Cascade

As mentioned earlier, there are hardly any three-dimensional experimental data currently available in the published literature. This lacuna is being addressed by the unsteady aerodynamics research programme at the University of Durham in the form of an experimental investigation in a low speed linear oscillating compressor cascade test facility with three-dimensional blade oscillation. The complete description of the test setup and the experimental programme are given in a report submitted to the School of Engineering, University of Durham (Yang, 2000). The results from the experimental work have since been communicated for publication (Yang and He, 2002).

This is a low speed, open flow facility built especially for this experimental work. The test section is designed to provide a uniform rectilinear flow. The linear cascade comprises of seven controlled-diffusion airfoils with the middle blade subjected to oscillation in the bending mode. The influence coefficient method has been used for obtaining values for different inter-blade phase angles. This method assumes linear behaviour which was checked (see p 79). The details of cascade airfoil blade profile specifications and operating conditions of the test facility are listed below:

Blade chord   C   =150mm

77

Aspect ratio	H/C	$=1.27$
Solidity	C/S	$=1.67$
Airfoil spacing	S	$=90$mm
Blade inlet angle	α	$=39.0^\circ$
Blade exit angle	β	$=3.5^\circ$
Stagger angle	γ	$=14.2^\circ$
Amplitude of oscillation	A_m	$=9$mm (6% of C)
Inlet flow angle range		$=37^\circ - 45^\circ$
Reynolds number		$=1.95 \times 10^5$
Typical exit velocity		$=19.5$ m/s
Bending mode direction		$=75.8^\circ$

The blade profile along with the computational mesh is shown in Fig. 7.6. For the present computations, an inlet flow angle of 38.0° is specified and the exit static pressure is set to obtain an exit velocity of 66 m/s. The exit velocity is chosen in such a way to ensure that the flow remains incompressible while the present solver, based on compressible flow equations, can still handle the flow. The mesh size for the present computations is $135 \times 41 \times 51$ in the streamwise, pitchwise and radial directions, respectively.

First, the steady flow through the cascade is computed and the static pressure coefficients are plotted in Fig. 7.7 against blade axial chord for four spanwise locations of 20%, 50%, 70% and 90%. The pressure coefficient is defined by

$$c_p = \frac{p - p_{exit}}{P_{01} - p_{exit}} \tag{7.2}$$

where P_{01} is the inlet total pressure. Also shown in Fig. 7.7 are the experimental values. It is seen that at 50% and 70% spanwise locations, the experiment indicates the presence of a separation bubble on the suction surface around 55% of the chord which the computation is not able to capture in the absence of a transition model. Also, at 90% span, the experimental values clearly show blade unloading towards the tip and the presence of secondary flow while the computation does not show this trend very clearly especially on the suction surface. The computation was performed without the inclusion of tip clearance while the experimental test configuration had a

tip gap of 0.5 percent chord to accommodate the blade motion. The inlet total pressure specification was based on the measured inlet total pressure profile which indicated the presence of inlet boundary layer. The computed pressure coefficient for all spanwise locations shows a somewhat jagged appearance on the suction surface, and the reason for this is not clear. However, the overall agreement between the calculated and the experimental values is good.

Having calculated the steady flow, the unsteady computation is performed for two reduced frequencies of 0.4 and 0.6 (based on blade chord and isentropic exit velocity). The amplitude specified at the tip is 6% of the blade chord. The bending amplitude is varied linearly along the span from hub to tip. In order to confirm the linear behaviour of the test configuration, the experimental tests were performed at two different bending amplitudes, 6% and 3.3% of the blade chord. Fig. 7.7a shows the amplitude and phase values of the unsteady pressure coefficient for these measurements and it shows a nearly identical response for both amplitudes, thereby confirming the linear behaviour. The unsteady results are presented at four spanwise locations of 20%, 50%, 70% and 90% for three inter-blade phase angles of $90°$, $180°$ and $-90°$. The unsteady pressure coefficient is defined by

$$\tilde{C}_p = \frac{\tilde{p}}{(P_{01} - p_{exit})A_m} \tag{7.3}$$

where A_m is the vibration amplitude at the tip. Fig. 7.8 to Fig. 7.11 show the amplitude and phase of unsteady pressure coefficient for the reduced frequency of 0.4 and inter-blade phase angle of $90°$. Also shown are the corresponding values from the experiment. The calculation slightly under predicts the unsteady pressure load for the forward 30% of the blade chord on both suction and pressure surfaces but this gradually improves towards 90% of the span as the vibration amplitude increases. The phase angle prediction shows a good agreement on the pressure surface while there is a slight under prediction on the suction surface for all the span locations.

The amplitude and phase of unsteady pressure for inter-blade phase angle of $180°$ are shown in Fig. 7.12 to Fig. 7.15. The calculation shows lower values for the amplitude than that experimentally observed till 70% span, particularly on the suction surface, indicating that the computation under predicts the effect of unsteadiness. The phase

predictions show a good agreement on the pressure surface and on the suction surface the calculation is unable to predict the change in sign in the phase distribution due to the separation bubble at 70% of the span.

For the inter-blade phase angle of -90°, the calculated unsteady pressure amplitude and phase along with the experimental values are shown in Fig. 7.16 to Fig. 7.19. In this case, the calculated values for the amplitude are slightly low compared to the experimental values on the suction surface for up to 70% of the span. At the same time, the pressure surface shows an over prediction between 20% and 40% of the chord for all the spanwise sections. The phase angle predictions show reasonably good agreement on the pressure surface for all the span locations while lower values are predicted for the suction surface for 70% and 90% of the span locations. This trend has been observed for all the three inter-blade phase angles. At 70% of the span, for all three phase angles, the experimental values show a clear change in sign in the phase distribution on the suction surface at around 55% of the chord due to the presence of separation bubble and the numerical prediction is unable to capture this.

Having computed the unsteady pressure, how this affects the stability of the cascade configuration should naturally be of interest and to determine this, the aerodynamic damping coefficients are calculated for different inter-blade phase angles for the reduced frequency 0.4. Fig. 7.20 shows the calculated damping values along with experimentally determined values. It is seen the cascade configuration is stable for the entire range of phase angles and the computation is able to predict this trend correctly. Also, the values are slightly under predicted for all the phase angles except for -90°. This is consistent with the under prediction of unsteady pressure loads. For the phase angle -90°, while there is only a slight under prediction on the suction surface, the over prediction on the pressure surface between 20% and 40% of the chord seems to be contributing to a net amplitude that is higher than experimental value. Since the phase angle prediction in this case is similar to that of other inter-blade phase angles, the increase in damping can be attributed to the difference in pressure amplitude.

Next, the computational process is repeated for a reduced frequency of 0.6 and the entire trend as regards the amplitude and phase of unsteady pressure is found to be similar to that observed for reduced frequency 0.4. Therefore, for the sake of brevity,

those figures are not shown. However, the aerodynamic damping calculation is shown in Fig. 7.21 and this shows that the stability margins have increased as expected at a higher reduced frequency and the overall trend is similar to that observed for 0.4.

This entire exercise shows that the three-dimensional time-linearized Euler/Navier-Stokes code is able to predict three-dimensional unsteady flows associated with blade oscillations. Flutter is widely accepted as a linear phenomenon and the three-dimensional test cases considered for the present computation are also of linear nature. However, transonic unsteady flows involving shocks and their motions cause significant nonlinear contributions to the local unsteady response associated with blade flutter. As three-dimensional test data for such cases are not readily available, the present work has not included any nonlinear flutter problems.

Chapter 8

Conclusions and Suggestions

The present work is concerned with the development of efficient frequency domain methods for the prediction of three-dimensional unsteady turbomachinery flows. A three-dimensional Navier-Stokes solver has been developed incorporating the time-linearized method and nonlinear harmonic method. Some numerical investigations have been carried out towards understanding and predicting unsteady flows in turbomachinery with specific attention to flows around oscillating blades. These investigations have revealed the relative merits of the time-linearized method and the nonlinear harmonic method in addressing linear and nonlinear unsteady flows. Since three-dimensional numerical investigations are constrained by the lack of corresponding experimental data to validate them, those investigations have been carried out to the extent possible and in all the other cases two-dimensional investigations have been made necessary to validate the underlying methods. The following sections summarise the conclusions drawn from the present work and offer some suggestions for future work.

8.1   Linear Harmonic Method

In the area of frequency domain methods, the time-linearized method is widely used in two-dimensional inviscid and viscous calculations for unsteady flows in turbomachinery. In addition, three-dimensional inviscid Euler calculations are also performed wherever necessary. However, so far there has been no three-dimensional Navier-Stokes calculation involving the time-linearized method. The present work approached and implemented the development of three-dimensional time-linearized method for Euler/Navier-Stokes equations as a baseline method for the development of three-dimensional nonlinear harmonic method for Euler/Navier-Stokes equations.

In Chapter 4, a detailed description of the development of three-dimensional time-linearized method has been presented. In this method, the unsteady flow is decomposed into a steady flow plus a harmonically varying unsteady perturbation. The process of linearization transforms the original unsteady Euler/Navier-Stokes

equations into two equations, a steady flow equation and a time-linearized perturbation equation. A pseudotime time-marching technique is introduced to take advantage of well-developed time-marching schemes. The numerical solution technique involved a cell centred finite volume scheme for spatial discretization and a four stage Runge-Kutta scheme for time integration. Nonreflecting boundary conditions are applied for far-field boundaries and a slip wall boundary condition is used for Navier-Stokes equations.

The validation of the time-linearized Euler/Navier-Stokes method has been carried out in two steps. First, a set of two-dimensional cases comprising an oscillating flat plate cascade, a high frequency forced response case induced by incoming wakes for a flat plate cascade and an oscillating turbine cascade has been considered. For the oscillating flat plate cascade and the high frequency incoming wakes, a good comparison with LINSUB has been obtained. For the oscillating turbine cascade of Fourth Standard Configuration, the calculated results compared reasonably well with the experimental data. Secondly, a set of three-dimensional cases comprising an oscillating flat plate cascade and an oscillating linear compressor cascade has been considered. The agreement between the calculated Euler solution for the oscillating flat plate cascade and the solutions from Namba's semi-analytical method has been good. For the experimental case of oscillating linear compressor cascade, the calculated Navier-Stokes solutions agree reasonably well with the experimental data. The aerodynamic damping calculations show good agreement with experimental data indicating a reasonable prediction of stability margins. Therefore, the three-dimensional Euler/Navier-Stokes time-linearized method has been shown to predict unsteady flows around oscillating blades reasonably well.

8.2   Nonlinear Harmonic Method

The nonlinear harmonic method to predict nonlinear unsteady flows, was proposed by He (1996) and the two-dimensional prediction of nonlinear unsteady flows have been carried out successfully by Ning (Ning, 1998, He and Ning, 1998). The present work has extended the nonlinear harmonic Euler/Navier-Stokes method to three-dimensional unsteady flows. Also, inclusion of higher order harmonic perturbations through the harmonic balance technique has also been implemented. In order to

compute blade oscillation, the present work uses moving computational grid in three-dimensions. The need to extrapolate the flow variables from the boundary of the grid to the instantaneous location of the airfoil as done in the case of fixed grid solutions is thereby eliminated. In the nonlinear harmonic method, the unsteady flow is decomposed into a time-averaged flow and an unsteady perturbation. Due to the nonlinearity of the unsteady equations, time-averaging produces extra unsteady stress terms in the time-averaged equations which are evaluated from unsteady perturbations. While the unsteady perturbations are obtained by solving the harmonic perturbation equations, the coefficients of perturbation equations come from the solution of time-averaged equation. The time-averaged equations and harmonic perturbation equations interact with each other and this interaction is achieved through a strong coupling procedure. The nonlinear effects are included in the coupled solution approach between the time-averaged equation and the unsteady perturbation equation. The numerical solution method for the nonlinear harmonic method is very similar to that used in the time-linearized method.

In order to handle strong nonlinearity in the flow, the present work also includes a harmonic balancing technique, as proposed by He (2001), to include higher order perturbations in the solution of nonlinear flows as the original nonlinear harmonic method could handle only first order perturbations. This harmonic balancing technique introduces cross coupling of higher order perturbations which in turn improves the accuracy of the fundamental harmonic through interaction with the time-averaged equation. In the absence of higher order perturbations, the harmonic balancing technique reduces to that of the first order perturbation equation of the basic nonlinear harmonic method.

The validation of the nonlinear harmonic method has been carried out by calculating transonic unsteady flows in a diverging channel and transonic flows through an axial flow fan rotor subjected to inlet flow distortion. The calculation for the inviscid transonic unsteady flows in a diverging channel has shown that the nonlinear harmonic method can handle very strong levels of nonlinearity resulting from large amplitude shock oscillation. The calculated values have been compared with solutions from nonlinear time-marching method and time-linearized method. These comparisons have shown that the validity of the time-linearized method for unsteady

flows is based on the strength of nonlinearity in the flow field. The nonlinear harmonic method considerably improves the solution over the time-linearized method in the presence of nonlinear effects. In addition, the inclusion of higher order perturbations has enabled the nonlinear harmonic method to predict the strong nonlinearity on a par with the nonlinear time-marching method. On the other hand, the limitation of the nonlinear harmonic method has been observed from the calculated results for inlet distortion through a transonic axial flow fan rotor. These calculations have shown that the nonlinear harmonic method has a tendency to amplify the nonlinearity in situations like oscillating shock interacting with the boundary layer.

In terms of computational cost, the nonlinear harmonic method consumes 75% of CPU time more than the time-linearized analysis, but it is still more efficient than the nonlinear time-marching method for a similar calculation even after the inclusion of cross coupling of higher order perturbations.

8.3   Suggestions for Future Work

Based on the limitations observed for the nonlinear harmonic method, it is imperative to address the linearization of the turbulence viscosity in the perturbation equations. The present practice of freezing the viscosity to its steady value seems to pose problems in cases of strong viscous displacement effects. Also, the current form of linearization of the pressure sensor in the numerical smoothing needs to be refined, to handle flows with strong nonlinearity.

As far as unsteady predictions are concerned, the three-dimensional blade flutter analysis problem can be approached to address nonlinear effects by including large amplitude oscillations or by considering transonic flows with strong shock motions. Since nonlinear harmonic method can handle perturbation from multiple sources of unsteadiness, the blade flutter analysis could also include other sources of unsteadiness such as inlet distortions, bladerow interactions etc. In addition, some more cases of three-dimensional blade flutter and forced response problems can be considered for validation. The three-dimensional unsteady flow prediction will have a

number of applications in the area of flutter and forced response prediction and analysis in the future.

References

Abhari, R.S. and Giles, M., 1997, "A Navier-Stokes Analysis of Airfoils in Oscillating Transonic Cascades for the Prediction of Aerodynamic Damping," ASME Journal of Turbomachinery, Vol. 199, pp. 77-84

Adamczyk, J.J., 1985, "Model Equations for Simulating Flows in Multistage Turbomachinery," ASME Paper 85-GT-226

Adamczyk, J.J., 2000, "Aerodynamic Analysis of Multistage Turbomachinery Flows in Support of Aerodynamic Design," ASME Journal of Turbomachinery, Vol. 122, pp. 189-217

Arnone, A., and Pacciani, R., 1998, "IGV-Rotor Interaction Analysis in a Transonic Compresor Using the Navier-Stokes Equations," ASME Journal of Turbomachinery, Vol. 120, pp. 147-155

Ayer, T.C., and Verdon, J.M., 1998, "Validation of a Nonlinear Unsteady Aerodynamic Simulator for Vibrating Blade Rows," ASME Journal of Turbomachinery, Vol. 120, pp. 112-121

Baldwin, B.S., and Lomax, H., 1978, "Thin-Layer Approximation and Algebraic Model for Separated Turbulent Flow," AIAA Paper 78-257

Bell, D.L. and He, L., 2000, "Three-Dimensional Unsteady Flow for an Oscillating Turbine Blade and the Influence of Tip Leakage," ASME Journal of Turbomachinery, Vol. 122, pp. 93-101

Bolcs, A., and Fransson, T.H., 1986, "Aeroelasticity in Turbomachines, Comparison of Theoretical and Experimental Cascade Results," Communication du Laboratoire de Thermique Appliquee et de Turbomachines, No. 13, Lausanne, EPFL

Carstens, V., and Belz, J., 2000, "Investigation of Fluid-Structure Interaction in Vibrating Cascades Using a Time-Domain Method," Proceedings of the 9th International symposium on Unsteady Aerodynamics, Aeroacoustics and Aeroelasticity, eds, P. Ferrand and S. Aubert, pp.678-694

Carta, F.O., 1967, "Coupled Blade-Disc-Shroud Flutter Instabilities in Turbojet Engine Rotors," ASME Journal of Engineering for Power, Vol. 89, pp. 419-426

Carta, F.O., and St.Hilaire, A.O., 1980, Effect of Inter-blade Phase Angle and Incidence Angle on Cascade Pitching Stability," ASME Journal of Engineering for Power, Vol. 102, pp. 391-396

Carta, F.O., 1983, "Unsteady Aerodynamics and Gapwise Periodicity of Oscillating Cascaded Airfoils," ASME Journal of Engineering for Power, Vol. 105, pp. 565-574

Chassaing, J.C., and Gerolymos, G.A., 2000, "Compressor Flutter Analysis Using Time-Nonlinear and Time-Linearized 3-D Navier-Stokes Methods," Proceedings of the 9th International symposium on Unsteady Aerodynamics, Aeroacoustics and Aeroelasticity, eds, P. Ferrand and S. Aubert, pp. 666-677

Chen, T., Vasanthakumar, P. and He, L., 2000, "Analysis of Unsteady Blade Row Interaction Using Nonlinear Harmonic Approach," AIAA Journal of Propulsion and Power, Vol. 17, No.3, pp. 601-608

Clark, W.S., and Hall, K.C., 2000, "A Time-Linearized Navier-Stokes Analysis of Stall Flutter," ASME Journal of Turbomachinery, Vol. 122, pp. 467-476

Dawes, W.N., 1988, "Development of a 3D Navier-Stokes Solver for Application to All Types of Turbomachinery," ASME Paper 88-GT-70

Denton, J.D., 1983, An Improved Time-Marching Method for Turbomachinery Flow Calculation," ASME, Journal of Engineering for Power, Vol. 105, pp. 514-524

Denton, J.D., 1992, "The Calculation of Three-Dimensional Viscous Flow Through Multistage Turbomachine", ASME Journal of Turbomachinery, Vol. 114, No. 1, pp. 18-26

Dorney, D.J., and Sharma, O.P., 1997, "Evaluation of Flow Field Approximations for Transonic Compressor Stages", ASME Journal of Turbomachinery, Vol. 119, pp. 445-451

Erdos, J.I., Alzner, E., and McNally, W., 1977, "Numerical Solution of Periodic Transonic Flow Through a Fan Stage," AIAA Journal, Vol. 15, No.11, pp. 1559-1568

Gerolymos, G.A., 1988, "Numerical Integration of the Blade-to-Blade Surface Euler Equations in Vibrating Cascades," AIAA Journal, Vol. 26, No. 12, pp. 1483-1492

Gerolymos, G.A., 1993, "Advances in the Numerical Integration of the Three-Dimensional Euler Equations in Vibrating Cascades," ASME Journal of Turbomachinery, Vol. 115, pp. 781-790

Giles, M.B., 1988, "Calculation of Unsteady Wake/Rotor Interaction", AIAA Journal of Propulsion and Power, Vol. 4, pp.356-362

Giles, M.B., 1990a, "Stator/Rotor Interaction in A Transonic Turbine", Journal of Propulsion and Power, Vol.6, No.5, pp.621-627

Giles, M.B, 1992, "An Approach for Multi-stage Calculations Incorporating Unsteadiness", ASME Paper 92-GT-282

Giles, M.B., 1993, "Validation of a Numarical Method for Unsteady Flow Calculations," ASME Journal of Turbomachinery, Vol. 115, pp. 110-117

Gruber, B, and Carstens, V., 1998, "Computation of the Unsteady Transonic Flow in Harmonically Oscillating Turbine Cascades Taking into Account Viscous Effects," ASME Journal of Turbomachinery, Vol. 120, pp. 104-111

Hah, C., Rabe, D.C., Sullivan, T.J., and Wadia, A.R., 1998, "Effects of Inlet Distortion on the Flow Field in a Transoinic Compressor Rotor," ASME Journal of Turbomachinery, Vol. 120, pp. 233-246

Hall, E.J., 1997, "Aerodynamic Modeling of Multistage Compressor Flowfields – Part 2; Modelling Deterministic Stresses," ASME Paper 97-GT-345

Hall, K.C., and Crawley, E.F., 1989, "Calculation of Unsteady Flows in Turbomachinery Using the Linearized Euler Euqations," AIAA Journal, Vol.27, No.6, pp.777-787

Hall, K.C. and Lorence, C.B., 1993, "Calculation of Three-Dimensional Unsteady Flows in turbomachinery Using the Linearized Harmonic Euler Equations," ASME.Journal of Turbomachinery, Vol. 115, pp. 800-809

Hall, K.C., Clark, W.S., and Lorence, C.B., 1994, "A Linearized Euler Analysis of Unsteady Transonic Flows in Turbomachinery," ASME Journal of Turbomachinery, Vol. 116, pp. 477-488

Hall, K.C., Thomas, J.P. and Clark, W.S., 2002, "Computation of Unsteady Nonlinear Flows in Cascades Using a Harmonic Balance Technique," AIAA Journal, Vol. 40, No. 5, pp. 879-886.

He, L., 1990, "An Euler Solution for Unsteady Flows Around Oscillating Blades," ASME Journal of Turbomachinery, Vol. 112, pp. 714-722

He, L., 1992, "A Method of Simulating Unsteady Turbomachinery Flows With Multiple Perturbations," AIAA Journal, Vol. 30, No. 12, pp. 2730-2735

He, L., 1993, "A New Two Grid Acceleration Method for Unsteady Navier-Stokes Calculations, AIAA Journal of Propulsion and Power, Vol. 9, No. 2

He, L., 1994, "Integration of Two-Dimensional Fluid/Structure Coupled System for Calculations of Turbomachinery Aerodynamic/Aeroelastic Instabilities," Intl. Jl. of Computational. Fluid Dynamics, Vol. 3, pp. 217-231

He, L. and Denton, J.D., 1994, "Three-Dimensional Time-Marching Inviscid and Viscous Solutions for Unsteady Flows Around Vibrating Blades," ASME Journal of Turbomachinery, Vol. 116, pp. 469-476

He, L., 1996, "Modelling Issues for Computation of Unsteady Turbomachinery Flows," Unsteady Flows in Turbomachines, VKI Lecture Series 1996-05, von Karman Institute for Fluid Dynamics.

He, L., and Ning, W., 1998, "Efficient Approach for Analysis of Unsteady Viscous Flows in Turbomachines," AIAA Journal, Vol.36, No.11, pp. 2005-2012

He, L., 1999, "Nonlinear Time-Domain Aerodynamic Solutions," Aeroelasticity in Axial-Flow Turbomachines, VKI Lecture Series 1999-05, von Karman Institute for Fluid Dynamics.

He, L., 2001, University of Durham, Private Communication

Holmes, D.G., and Lorence, C.B., 1997, "Three-Dimensional Linearized Navier-Stokes Calculation for Flutter and Forced Response," Proceedings of the 8th International Symposium on Unsteady Aerodynamics and Aeroelasticity of Turbomachines, ed. T.H. Fransson, Kluwer Academic Publishers, pp. 211-224

Isomura, K., and Giles, M.B., 1998, "A Numarical Study of Flutter in a Transonic Fan,""ASME Journal of Turbomachinery, Vol. 120, pp. 500-507

Jameson, A., Schmidt, W., and Turkel, E., 1981, "Numerical Solutions of the Euler Equation by Finite Volume Method Using Runge-Kutta Time-stepping Scheme," AIAA Paper No. 81-1259

Jameson, A., 1991, "Time Dependent Calculations Using Multigrid With application to Unsteady Flows Past Airfoils and Wings," AIAA Paper No. 91-1596

Kielb, R.E., 1999, "Flutter Design Analysis," Aeroelasticity in Axial Flow Turbomachines, VKI Lecture Series, 1999-05, von Karman Institute of Fluid Dymanics.

Koya, M. and Kotake, S., 1985, "Numerical Analysis of Fully Three-Dimensional periodic Flows Through a Turbine Stage," ASME Journal of Engineering for Gas Turbine and Power, Vol. 107, pp. 945-952

Lane, F., 1956, "System Mode Shapes in the Flutter of Compressor Blade Rows," Journal of the Aeronautical Sciences, Vol. 23, No.1, pp. 54-66

Li, H.D., and He, L., 2002, "Single Passage Analysis of Unsteady Flows around Vibrating Blades of a Transonic Fan under Inlet Distortion," ASME Journal of Turbomachinery, Vol. 124, pp. 285-292

Lindquist and Giles, M.B., 1994, "Validity of Linearized Unsteady Euler Equations With Shock Capturing," AIAA Journal, Vol. 32, No. 1, pp. 46-53

Marshall, J.G., and Imregun, M., 1996, "An Analysis of the Aeroelastic Behaviour of a Typical Fan Blade with Emphasis on the Flutter Mechanism," ASME Paper 96-GT-78

Marshall, J.G., and Giles, M.B., 1997, "Some Applications of a Time-Linearized Euler Method to Flutter & Forced Response in turbomachinery," Proceedings of the 8th International Symposium on Unsteady Aerodynamics and Aeroelasticity of Turbomachines, ed. T.H. Fransson, Kluwer Academic Publishers, pp. 225-240

Morreti, G., and Abbett, M., 1966, "A Time-Dependent Computational Method for Blunt Body Flows," AIAA Journal, Vol. 4, No. 12, pp. 2136-2141 Ni, R.H., and Sisto, F., 1976, "Numerical Computation of Nonstationary Aerodynamics of Flat Plate Cascades in Compressible Flows," ASME Journal of Engineering for Power, Vol. 98, pp. 165-170

Namba, M., 1977, "Three-Dimensional Analysis of Blade Force and Sound Generation for an Annular Cascade in Distorted Flows," Journal of sound and Vibration, Vol. 50, pp. 479-508

Namba, M., and Ishikawa, A., 1983, "Three-Dimensional Aerodynamic Characteristics of Oscillating Supersonic and Transonic Annular Cascades," ASME Journal of Engineering for Power, Vol. 105, pp. 138-146

Namba, M., 1991, Kyushu University, Private Communication

Ni, R.H., 1982, A Multiple Grid Scheme for solving Euler Equations," AIAA Journal, Vol. 20, No. 11, pp. 1565-1571

Ni, R.H., 1989, "Prediction of Multistage Turbine Flow Filed Using a Multiple Grid Euler Solver, AIAA Paper No. 89-0203

Ning, W., 1998, "Computation of Unsteady Flow in Turbomachinery," Ph.D. Thesis, University of Durham

Ning, W. and He, L., 1998, "Computation of Unsteady Flows Around Oscillating Blades Using Linear and Non-Linear Harmonic Euler Methods," ASME Journal of Turbomachinery, Vol.120, pp.508-514

Platzer, M.F., and Carta, F.O., eds., 1988, "AGARD Manual on Aeroelasticity in Axial Flow Turbomachines, Vol.2 – Structural Dynamics and Aeroelaticity

Rai, M.M., 1987, "Navier-Stokes Simulations of Rotor-Stator Interaction Using Patched and Overlaid Grids," AIAA Journal of Propulsion and Power, Vol. 3, No. 5, pp. 387-396

Rai, M.M., 1989, "Three-Dimensional Navier-Stokes Simulations of Turbine Rotor-Stator Interaction", AIAA Journal of Propulsion and Power, Vol.5, No.3, pp.305-319

Rhie, C.M., Gleixner, A.J., Spear, D.A., Fischberg, C.J. and Zacharias, R.M., 1998, "Development and Application of a Multistage Navier-Stokes Solver, Part 1: Multistage Modelling Using Bodyforces and Deterministic Stresses", ASME Journal of Turbomachinery, Vol. 120, pp. 205-214

Saxer, A.P., and Giles, M.B., 1993, "Quasi-Three-Dimensional Nonreflecting Boundary Conditions for Euler Equation Calculations," AIAA Journal of Propulsion and Power, Vol. 9, No. 2, pp. 263-271

Sisto, F., 1977, "A Review of Fluid Mechanics of Aeroelasticity in Turbomachines," ASME Journal of Fluids Engineering, Vol. 99, pp. 40-44

Silkowski, P.D., and Hall, K.C., 1998, "A Coupled Mode Analysis of Unsteady Multistage Flows in Turbomachinery," ASME Journal of Turbomachinery, Vol. 120, pp. 410-421

Srinivasan, A.V., 1997, "Flutter and Resonant Vibration Characteristics of Engine Blades," ASME IGTI Scholar Paper 97-GT-533

Verdon, J.M., and Casper, J.R., 1982, "Development of a Linear Unsteady Aerodynamic Analysis for Finite-Deflection Subsonic Cascades," AIAA Journal, Vol. 20, N0. 9, pp. 1259-1267

Verdon, J.M., and Caspar, J.R., 1984, "A Linearized Unsteady Aerodynamic Ananlysis for Transonic Cascades," Journal of Fluid Mechanics, Vol. 149, pp. 403-429

Verdon, J.M., 1993, "Review of Unsteady Aerodynamic Methods for Turbomachinery Aeroelastic and Aeroacoustic Applications," AIAA Journal, Vol. 31, No. 2, pp. 235-250

Whitehead, D.S., 1987, "Classical Two-Dimensional Methods," AGARD Manual on Aeroelasticity in Axial Flow Turbomachines, Unsteady Turbomachinery Aerodynamics, Vol. 1, AGARD-AG-298

Wood, J.R., Strazisar, A.J., and Hathaway, M.D., 1990, "Test cases for Computation of Internal Flows in Aero Engine Components, Test Case – E/CO-2: Single Transonic Fan Rotor," AGARD-AR-275

Yang, H., 2000, "An Experiment on 3D Unsteady Flow in a Linear Oscillating Compressor Cascade," First Year Report, School of Engineering, University of Durham

Yang, H., and He, L., 2002, "Experiment on Linear Compressor Cascade with 3-D Blade Oscillation," ASME03-GT2003-38484, Communicated.
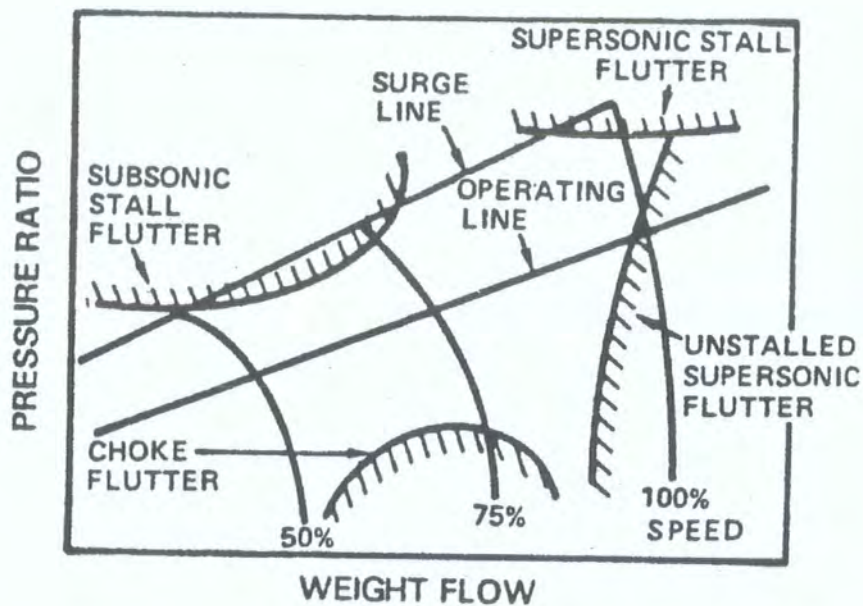
Fig. 1.1   Compressor operating map showing types of flutter
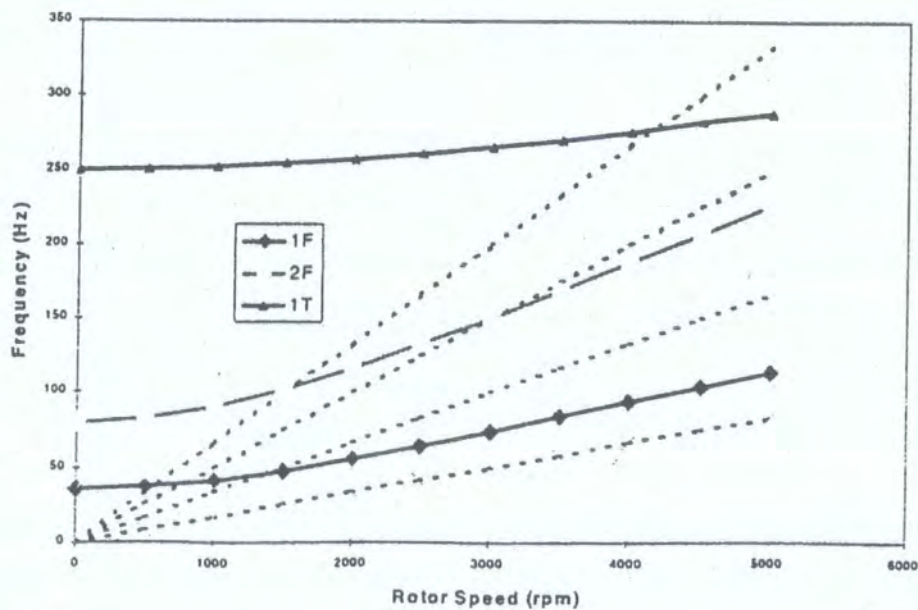
Fig. 1.2   Campbell diagram for a fan rotor blade
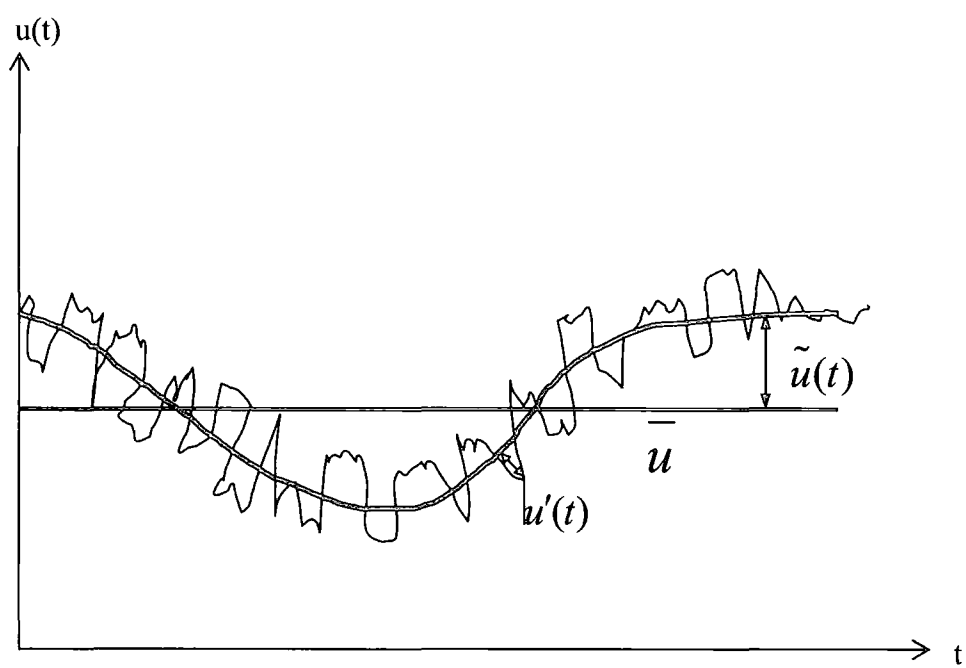
Figure 3.1   Distribution of unsteady velocity

$u'(t)$ Random unsteadiness

$\tilde{u}(t)$ Periodic (deterministic) unsteadiness

$\overline{u}$ Time mean velocity
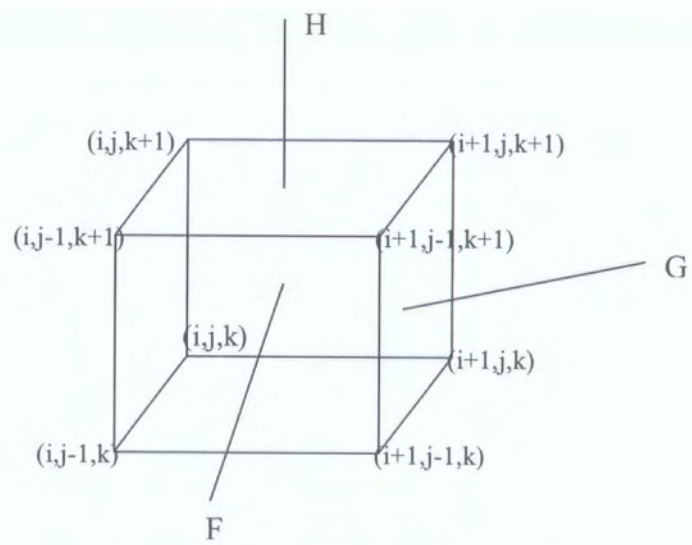
Fig. 4.1 Schematic of a three-dimensional finite volume computational cell
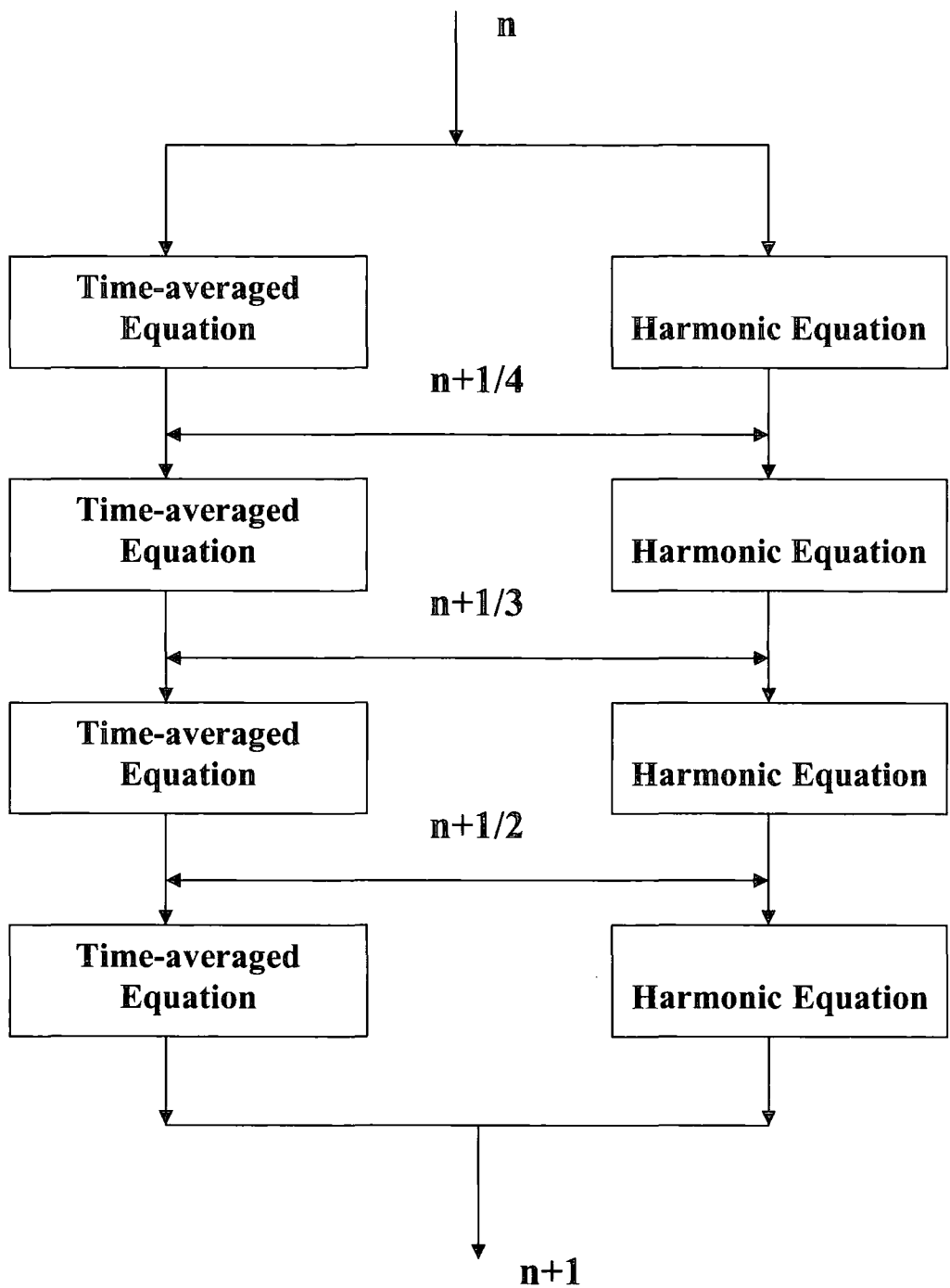
Fig. 5.1 Coupling procedure for nonlinear harmonic method in a four stage
Runge-Kutta scheme
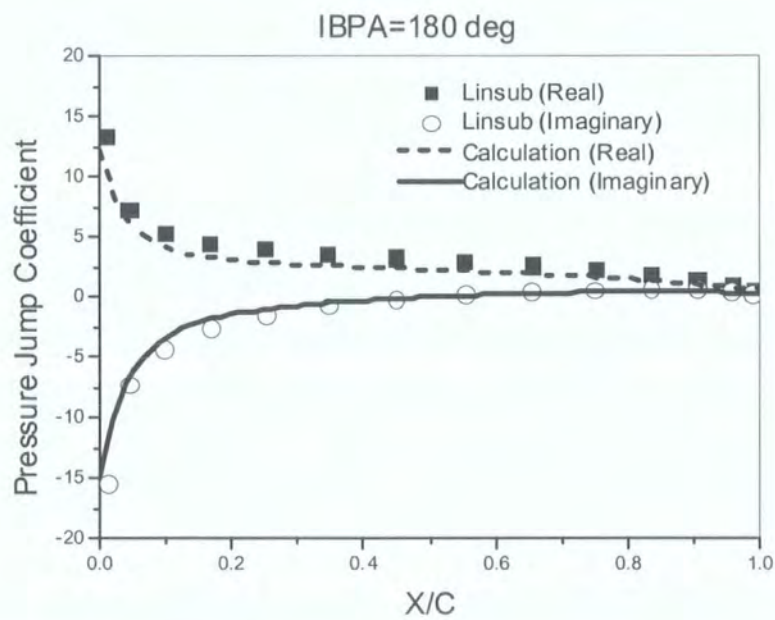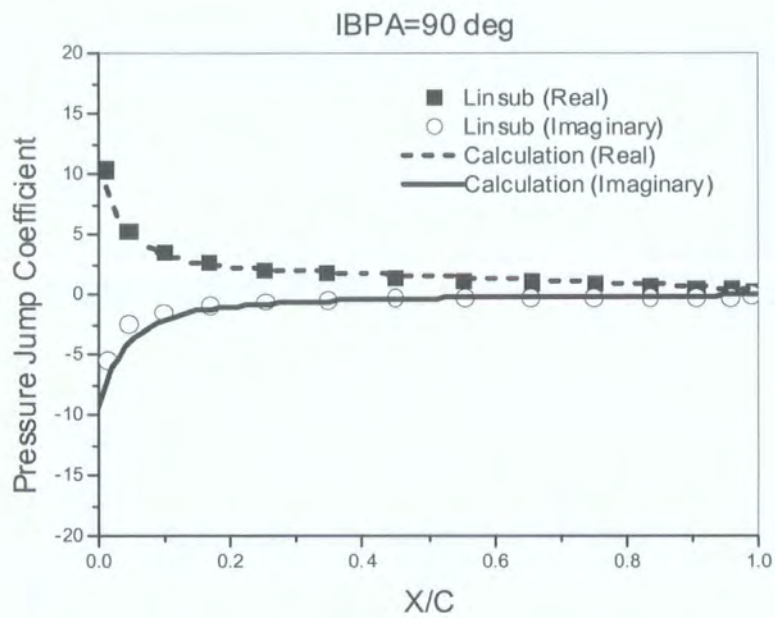
Fig 6.1 Real and imaginary parts of unsteady pressure jump coefficient for a
flat plate cascade (Bending; Reduced frequency=1.0)
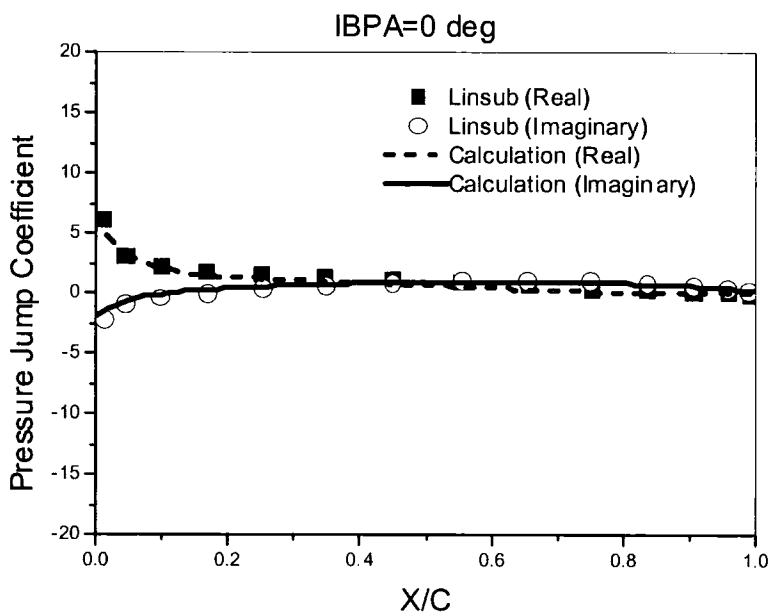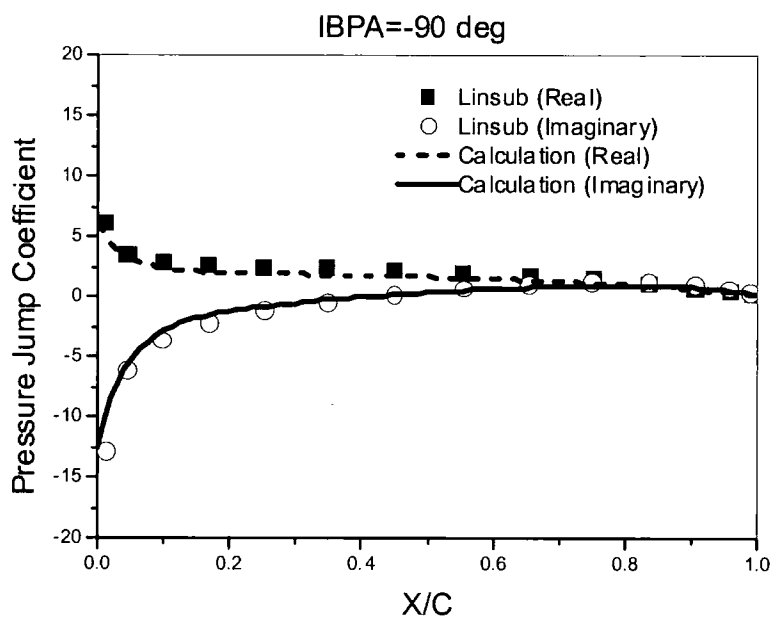
Fig 6.2 Real and imaginary parts of unsteady pressure jump coefficient for a
flat plate cascade (Bending; Reduced frequency=1.0)
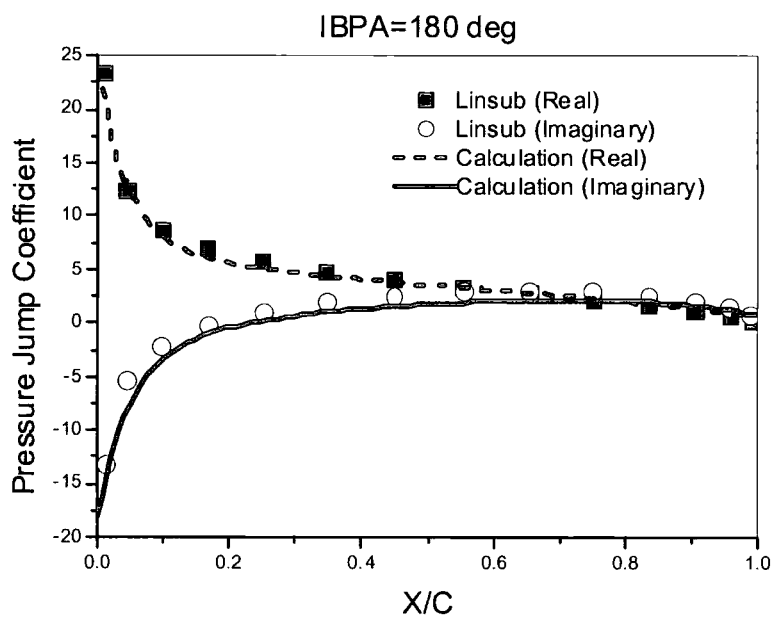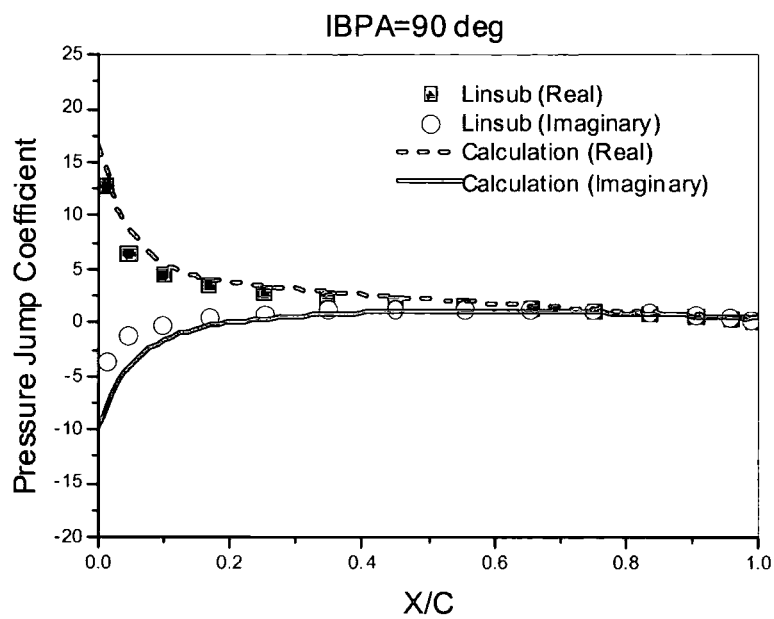
Fig 6.3 Real and imaginary parts of unsteady pressure jump coefficient for a flat plate cascade (Torsion; Reduced frequency=1.0)

IBPA=-90 deg

IBPA=0deg
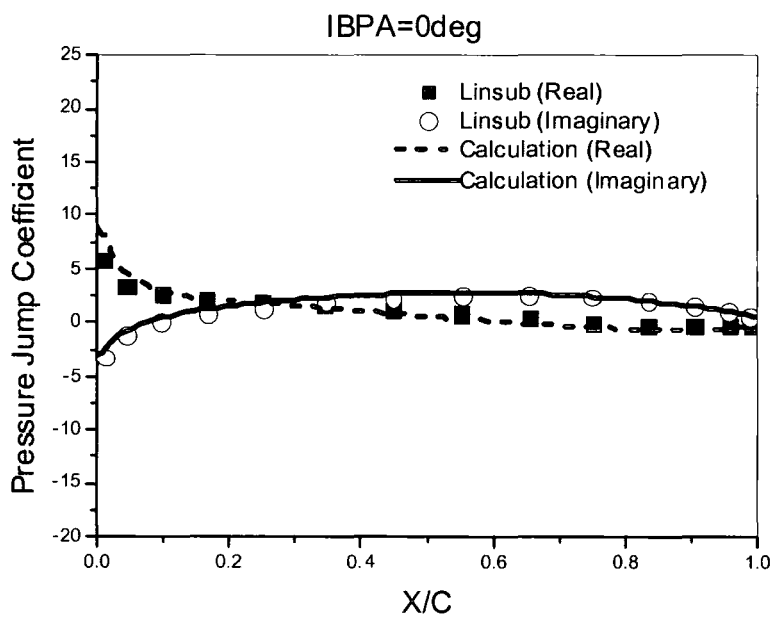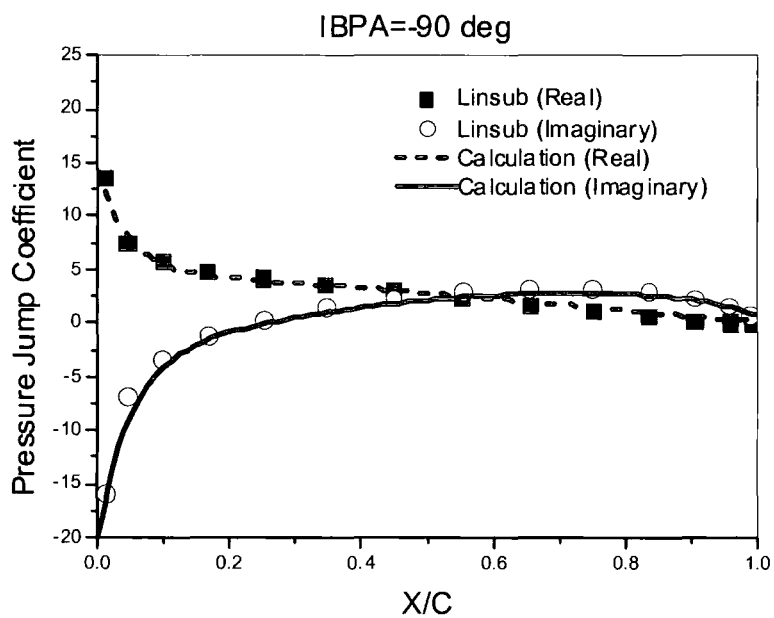
Fig 6.4 Real and imaginary parts of unsteady pressure jump coefficient for a flat plate cascade (Torsion; Reduced frequency=1.0)
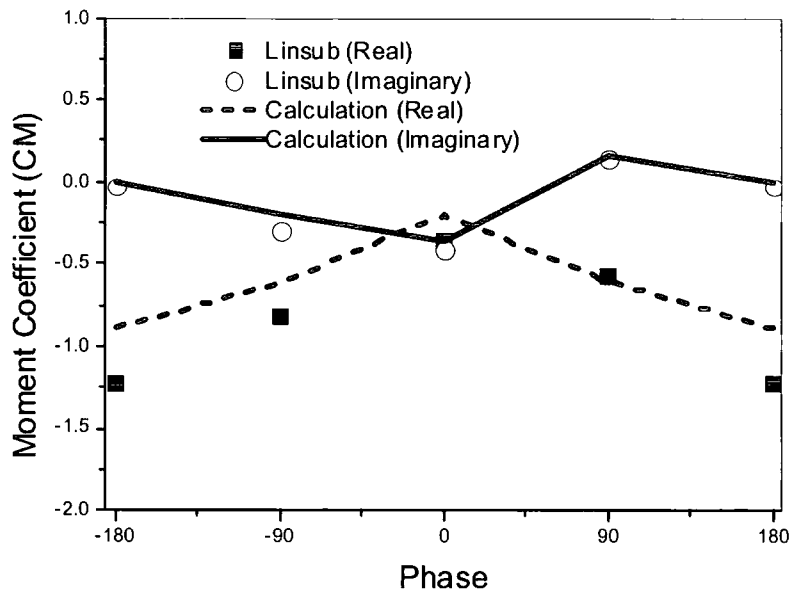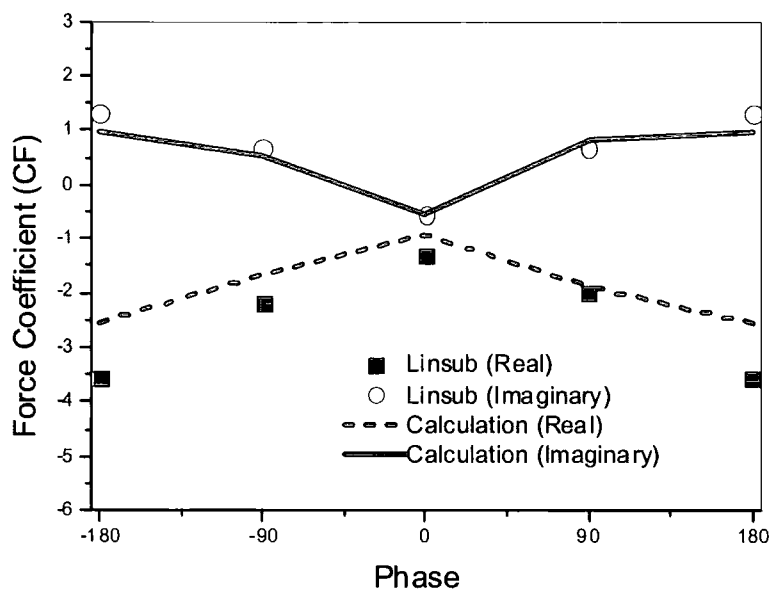
Fig 6.5 Force and moment coefficients for a flat plate cascade
(Bending; Reduced frequency=1.0)
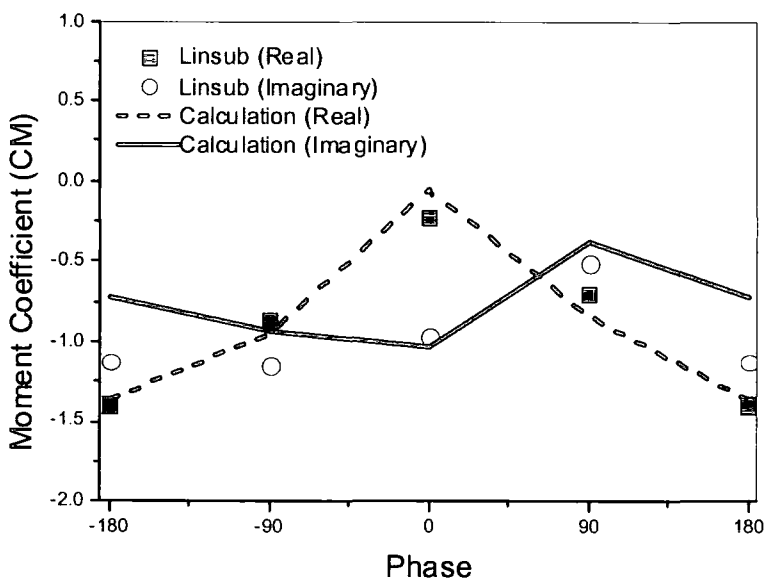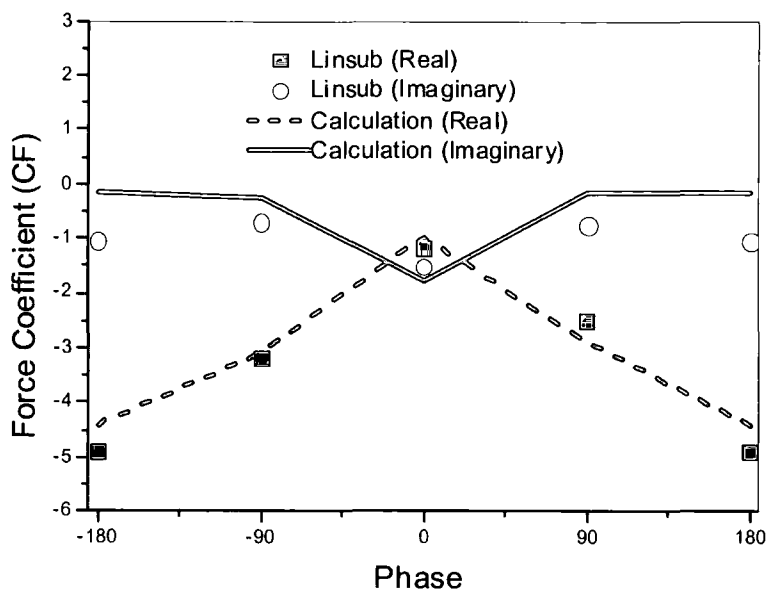
Fig 6.6 Force and moment coefficients for a flat plate cascade
(Torsion; Reduced frequency=1.0)
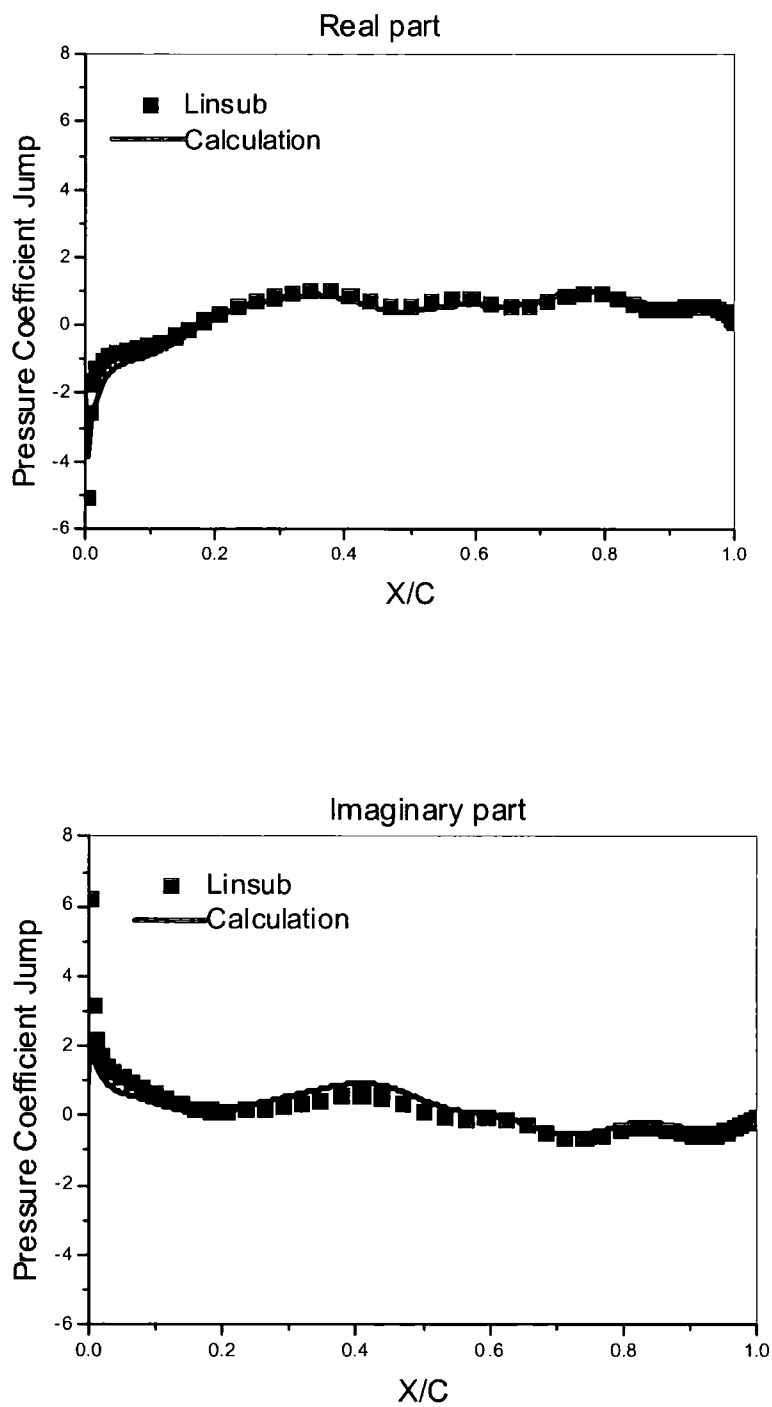
Fig 6.7 Unsteady pressure jump coefficient for a flat plate cascade
(Incoming wake angle = -30 deg; Reduced frequency=13.96)
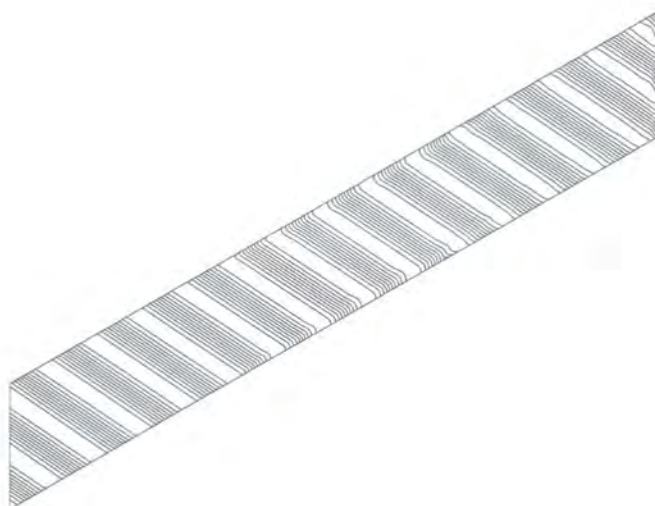
Fig 6.8 Instantaneous first harmonic entropy contour map for the
high frequency incoming wake
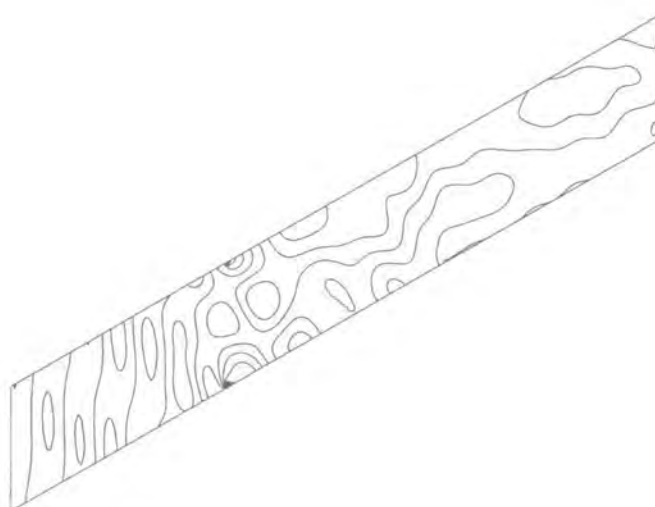
Fig 6.9 Instantaneous first harmonic pressure contour map for the
high frequency incoming wake
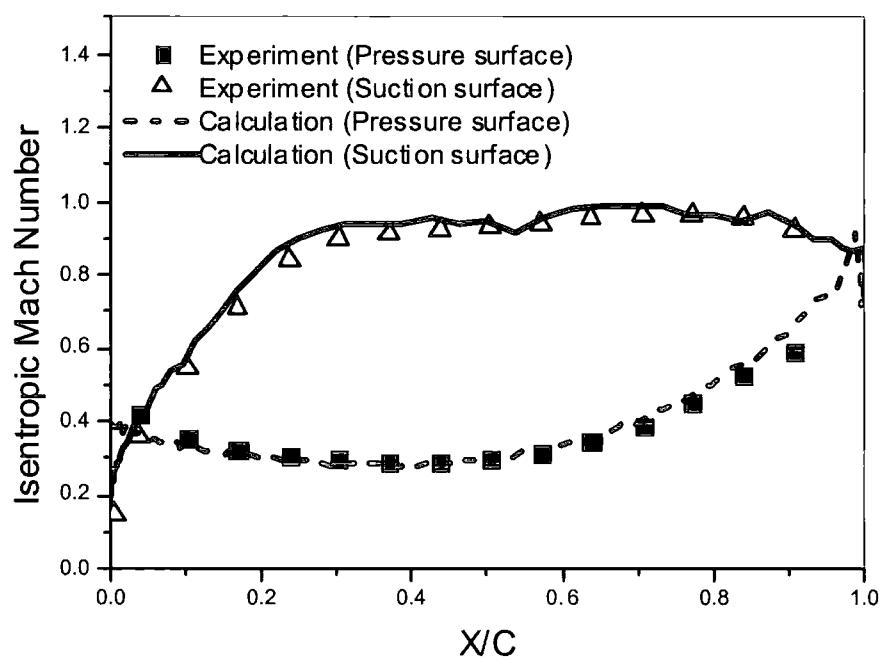
Fig. 6.10 Isentropic Mach number distribution for a turbine cascade
(Fourth Standard Configuration)
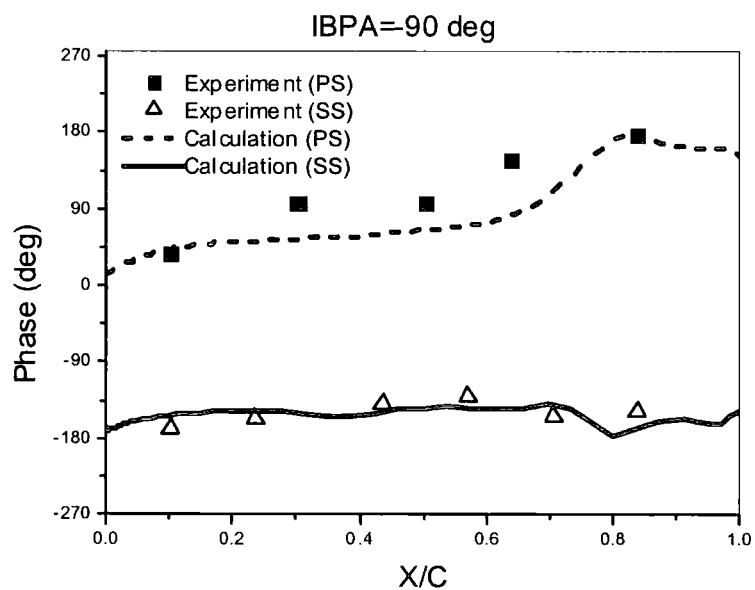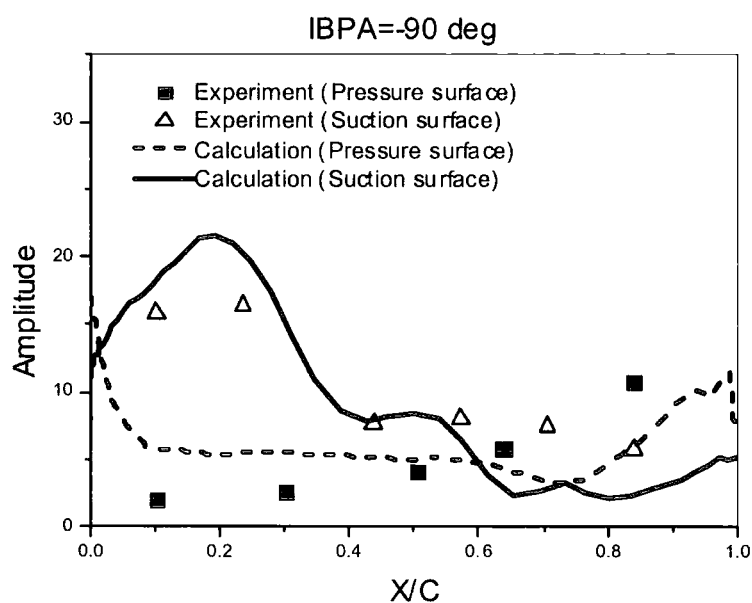
Fig. 6.11 Amplitude and phase of unsteady blade surface pressure
coefficient for a turbine blade (IBPA = -90 deg)
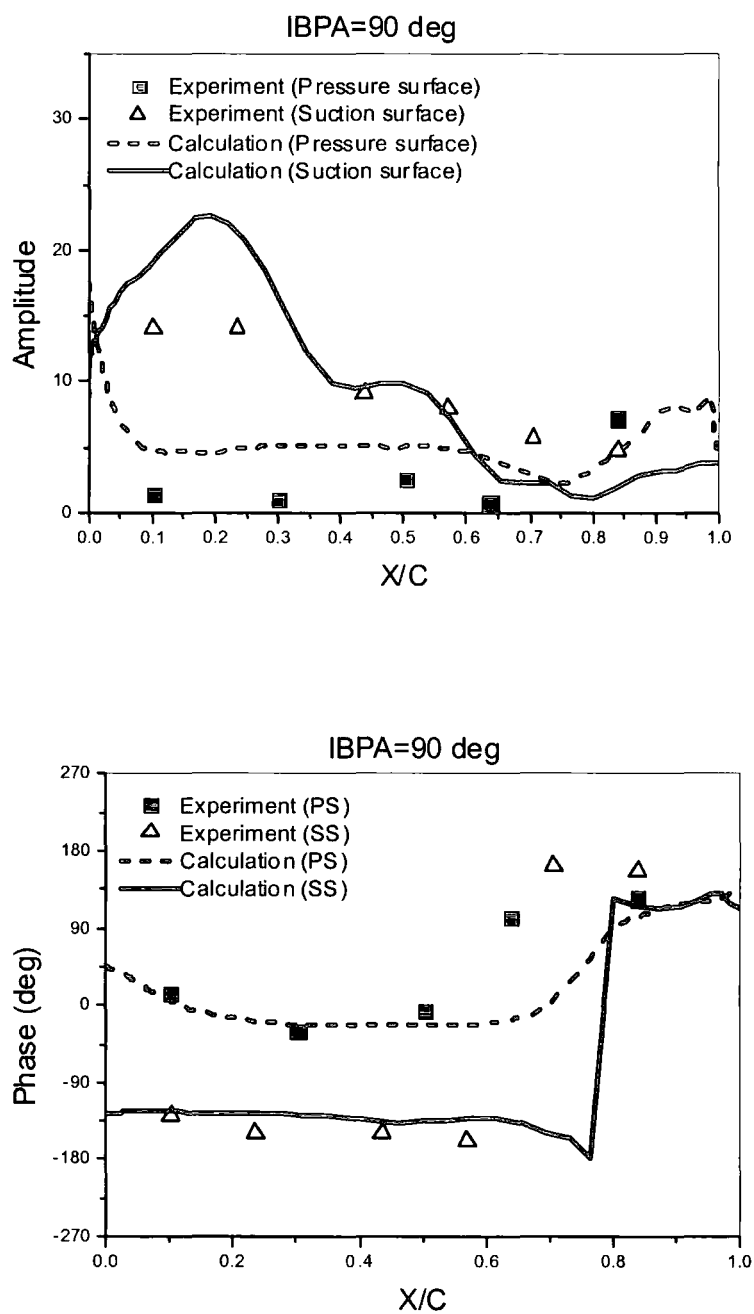
Fig. 6.12 Amplitude and phase of unsteady blade surface pressure
coefficient for a turbine blade (IBPA = 90 deg)
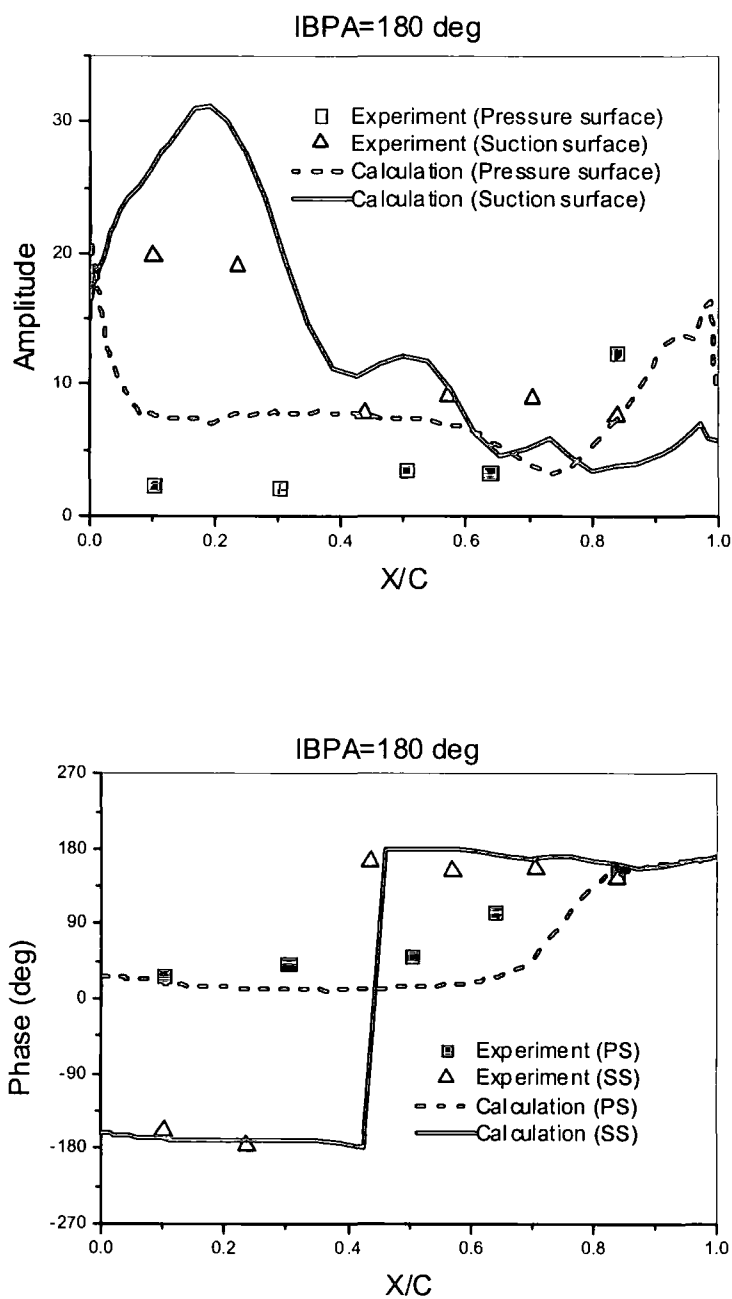
Fig. 6.13 Amplitude and phase of unsteady blade surface pressure
coefficient for a turbine blade (IBPA = 180 deg)
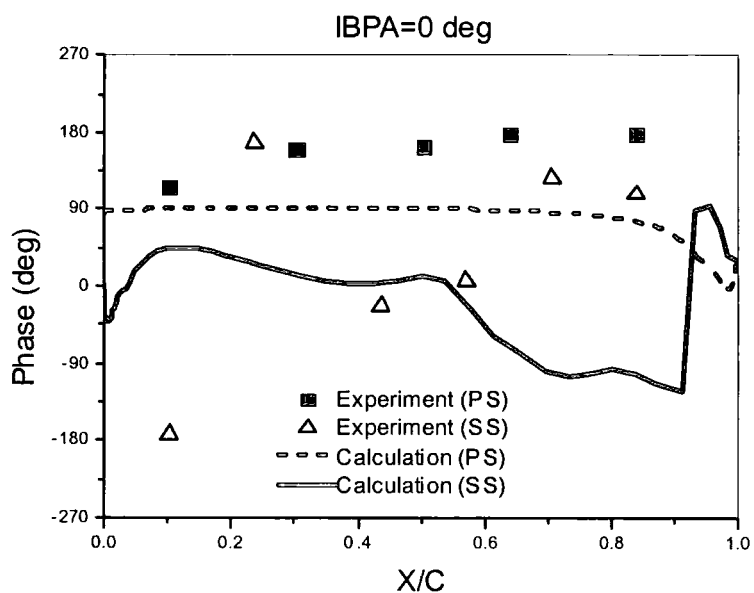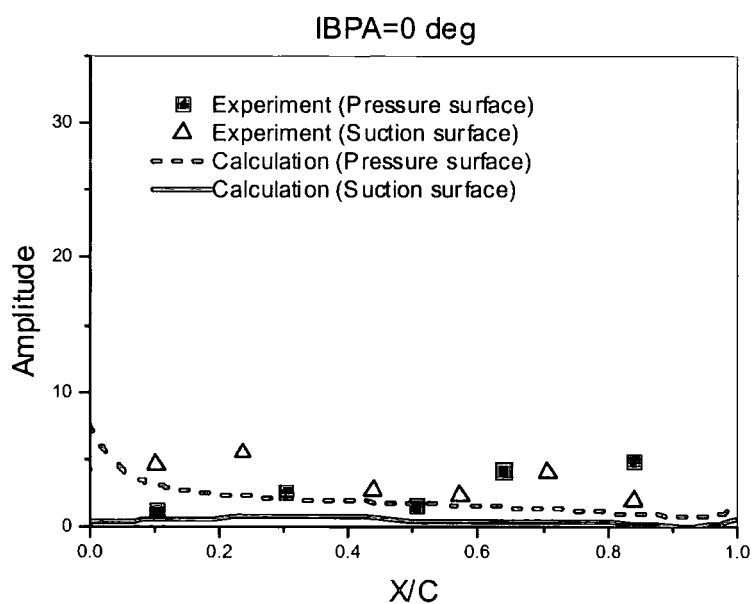
Fig. 6.14 Amplitude and phase of unsteady blade surface pressure
coefficient for a turbine blade (IBPA = 0 deg)
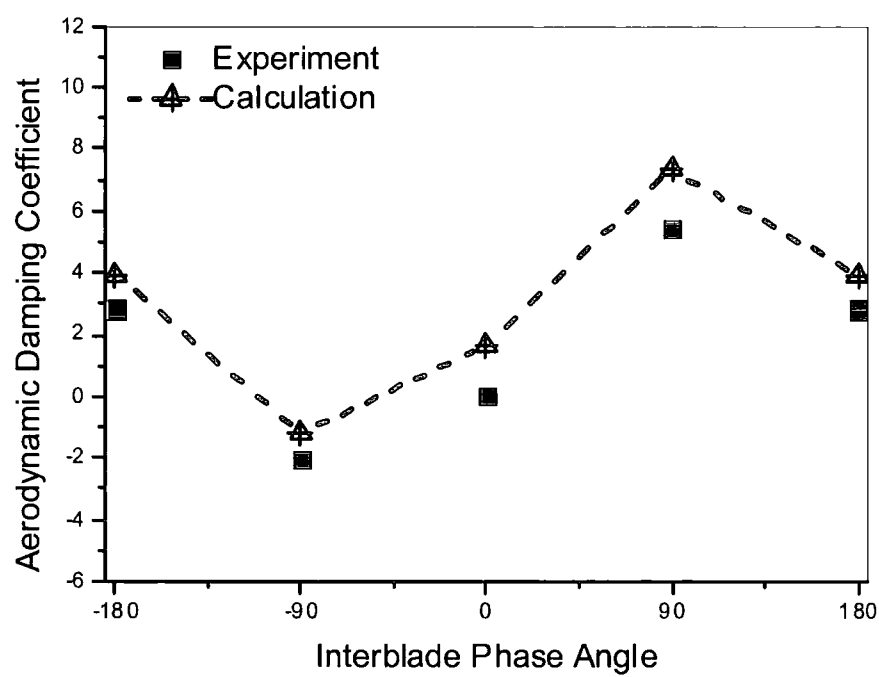
Fig. 6.15 Aerodynamic damping coefficients in dependence of
interblade phase angle (Fourth standard configuration)
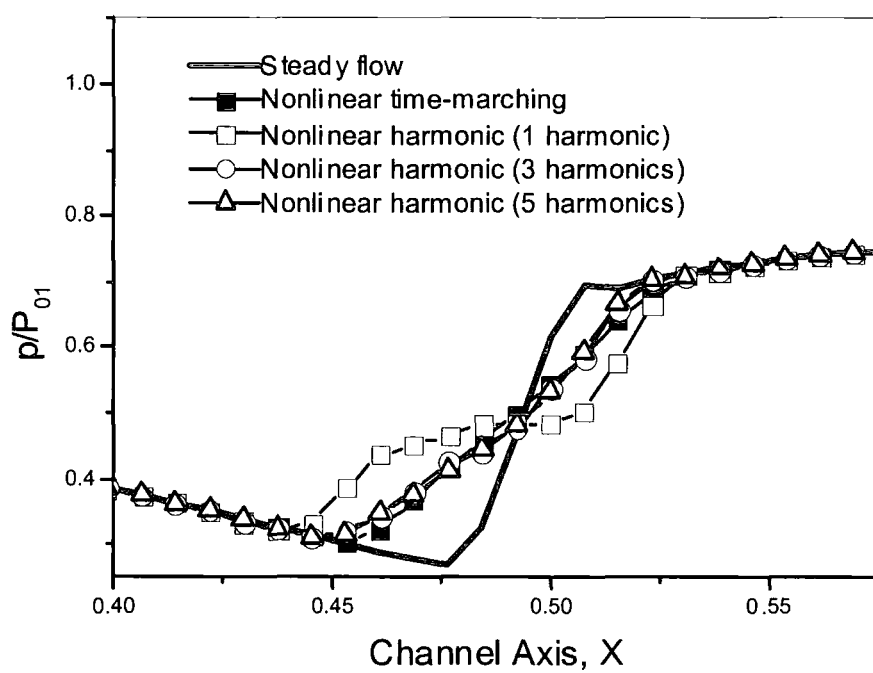
Fig. 6.16 Static pressure distribution for time-averaged flow and steady flow
for a diverging channel (Amplitude of disturbance: 7%)

Real part

Imaginary part
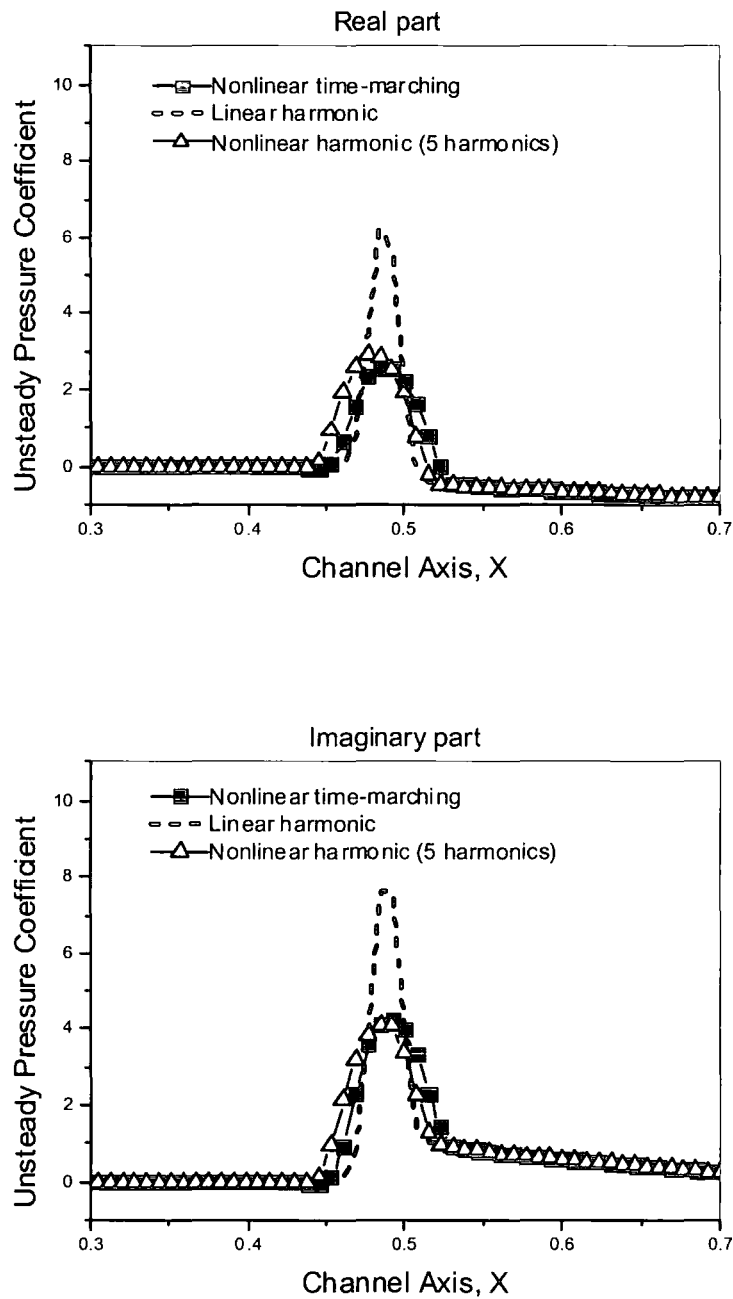
Fig. 6.17 First harmonic unsteady pressure coefficient for a diverging
channel (Amplitude of disturbance: 7%)

Real part

Unsteady Pressure Coefficient vs *Channel Axis, X*

Legend:
- Nonlinear time-marching
- Nonlinear harmonic (5 harmonics)

Imaginary part

Unsteady Pressure Coefficient vs *Channel Axis, X*

Legend:
- Nonlinear time-marching
- Nonlinear harmonic (5 harmonics)
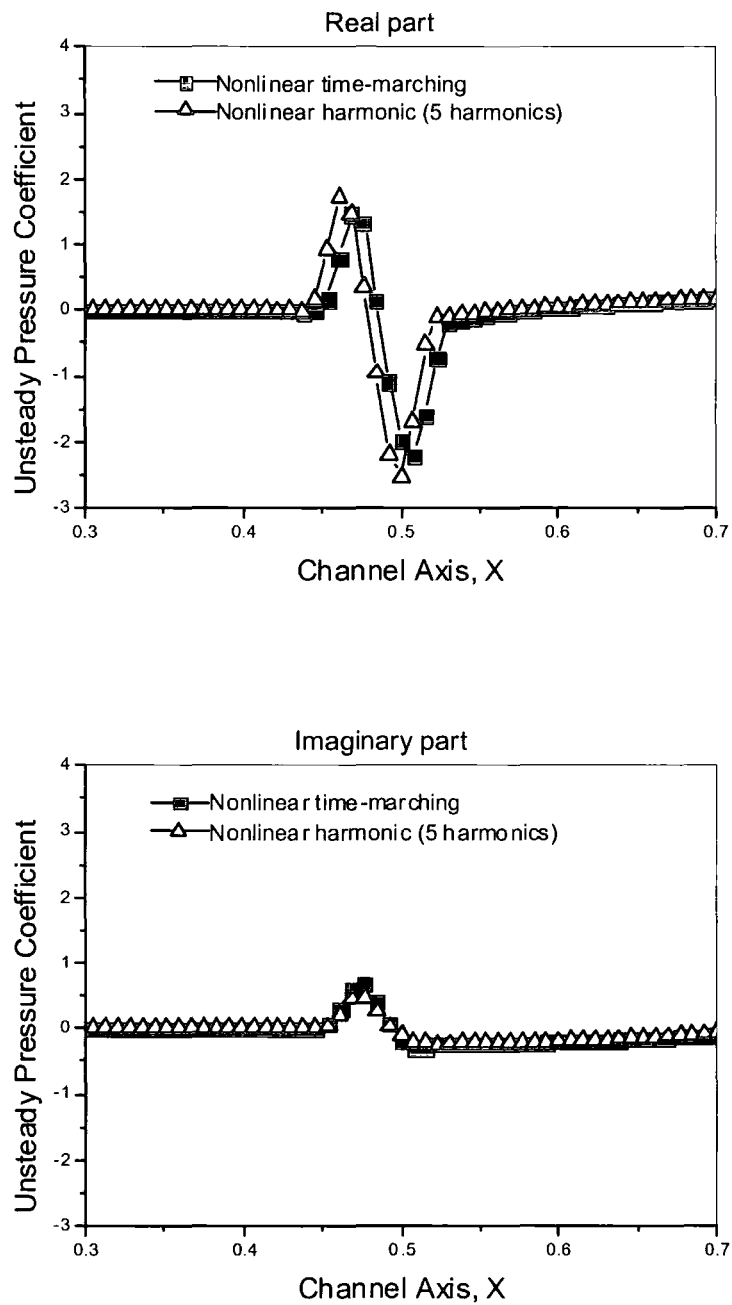
Fig. 6.18 Second harmonic unsteady pressure coefficient for a diverging channel (Amplitude of disturbance: 7%)
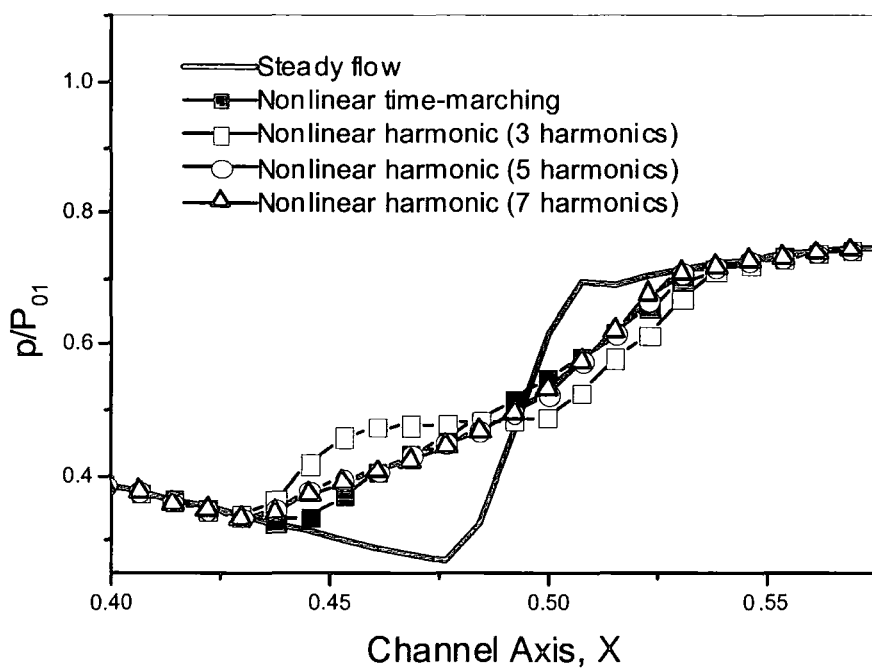
Fig. 6.19 Static pressure distribution for time-averaged flow and steady flow
for a diverging channel (Amplitude of disturbance 10%)

Real part

Imaginary part
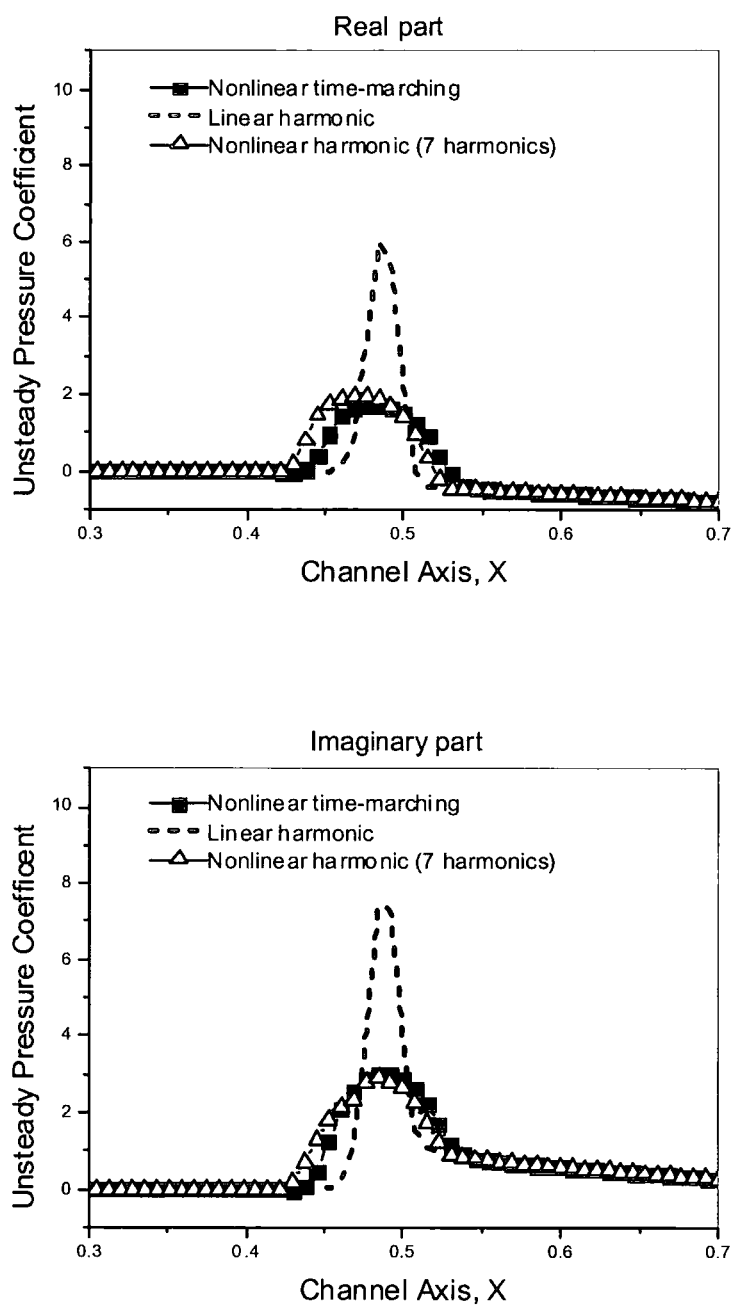
Fig. 6.20 First harmonic unsteady pressure coefficient for a diverging channel (Amplitude of disturbance: 10%)
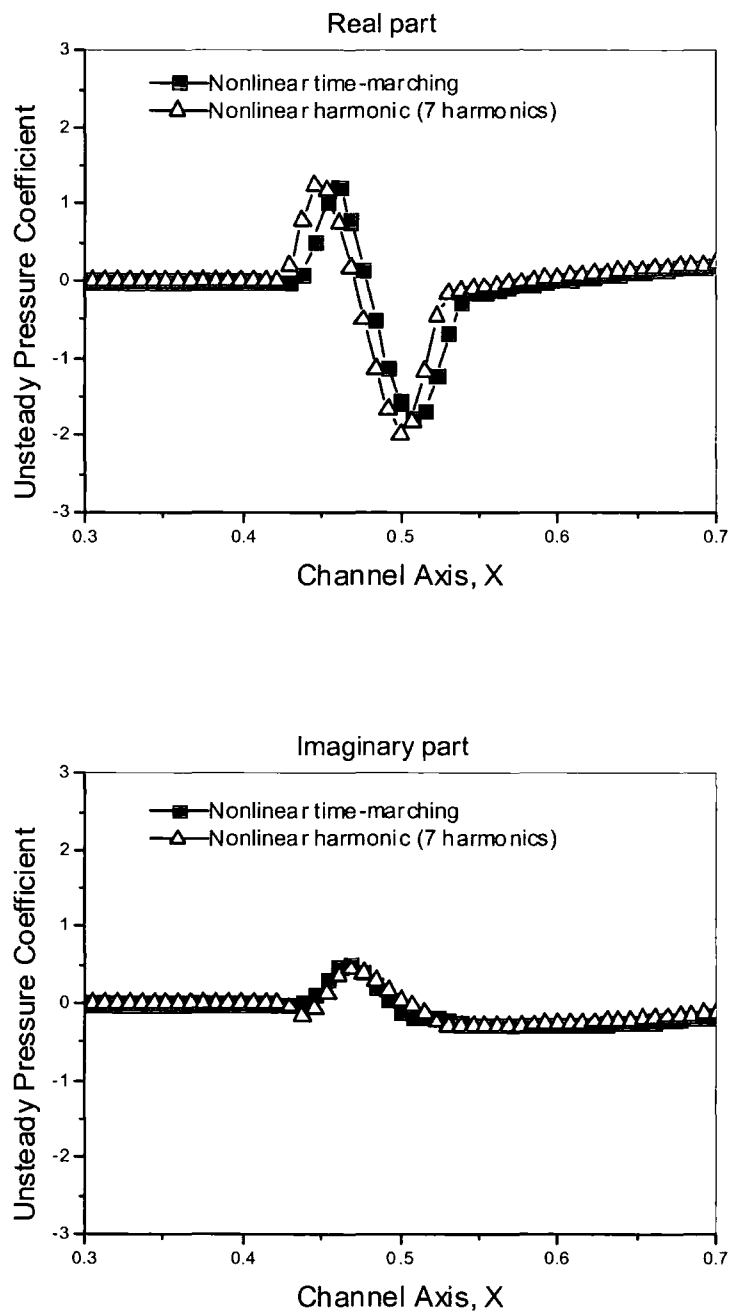
Fig. 6.21 Second harmonic unsteady pressure coefficient for a diverging
channel (Amplitude of disturbance: 10%)
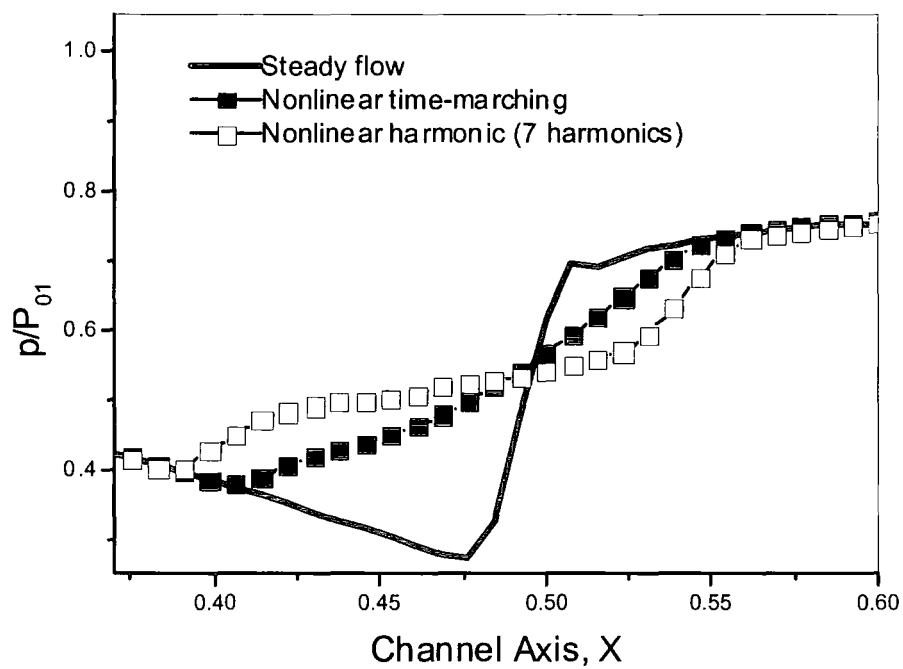
Fig. 6.22 Static pressure distribution for time-averaged flow and steady flow
for a diverging channel (Amplitude of disturbance 15%)

Real part

Imaginary part
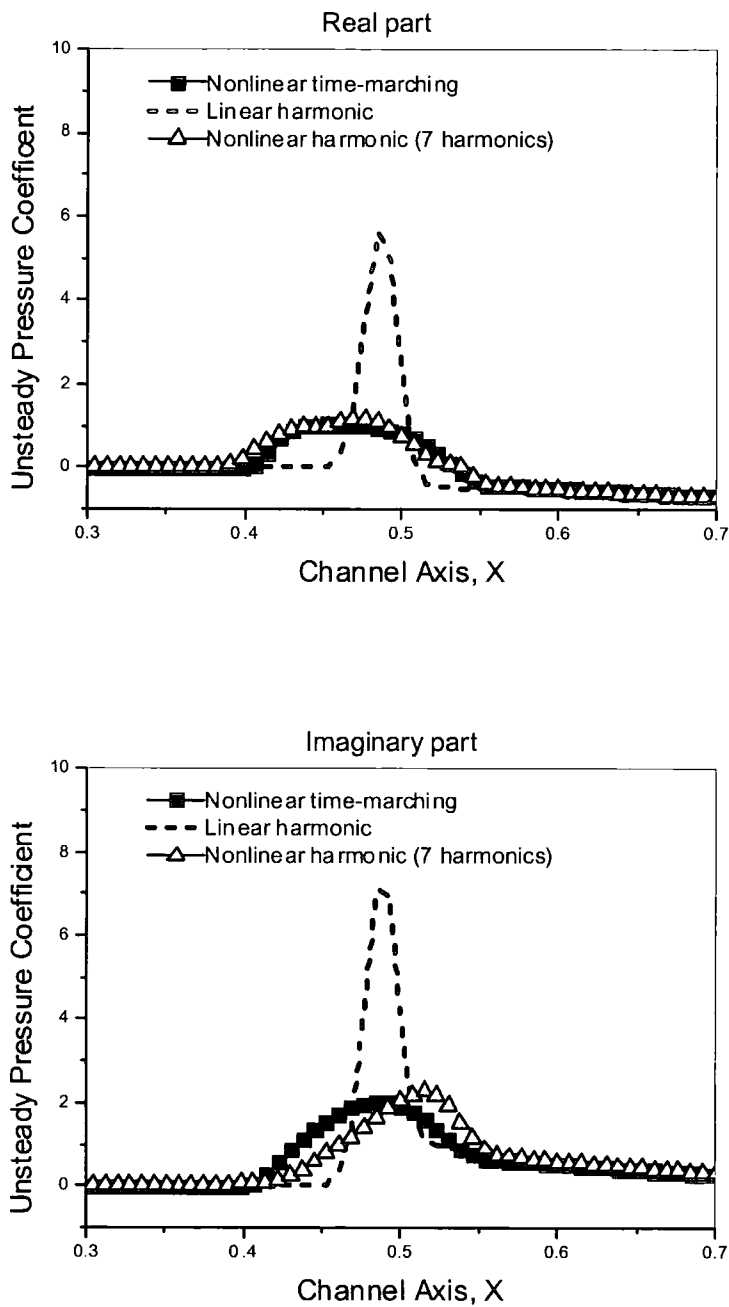
Fig. 6.23 First harmonic unsteady pressure coefficient for a diverging channel (Amplitude of disturbance: 15%)

Real part

Imaginary part
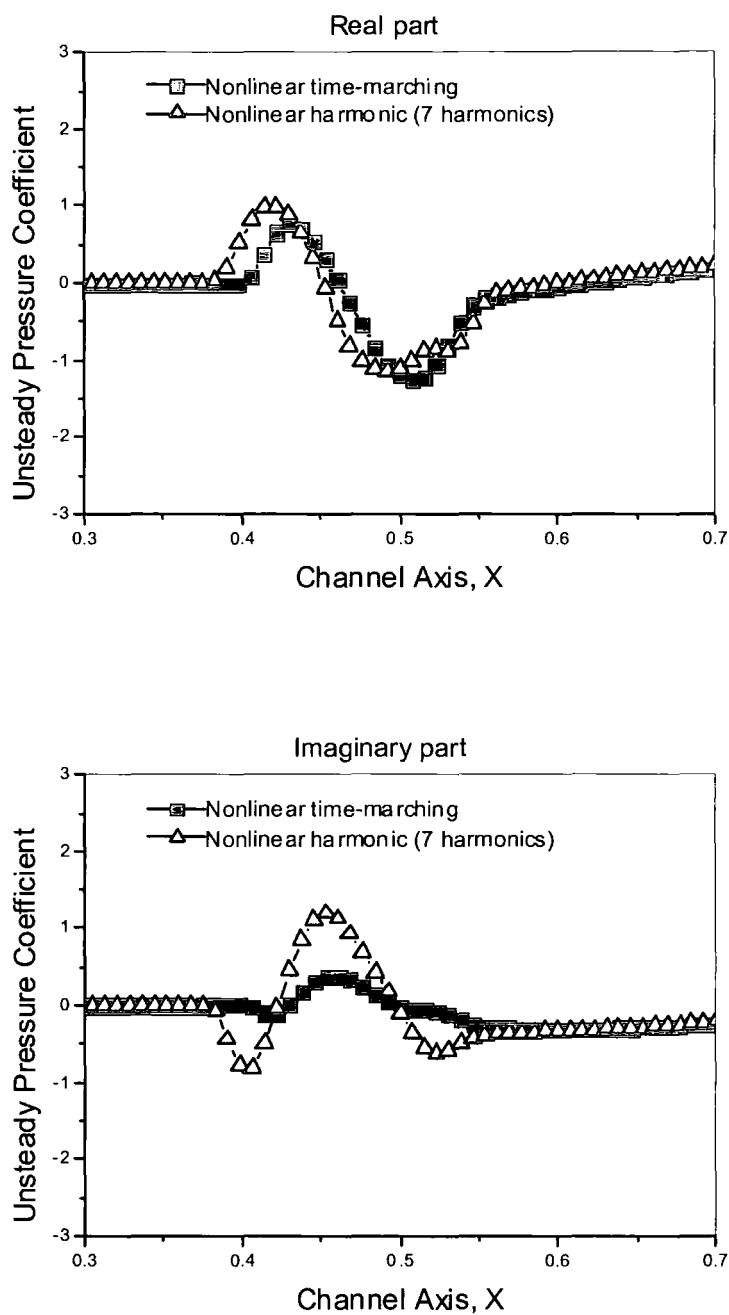
Fig. 6.24 Second harmonic unsteady pressure coefficient for a diverging
channel (Amplitude of disturbance: 15%)
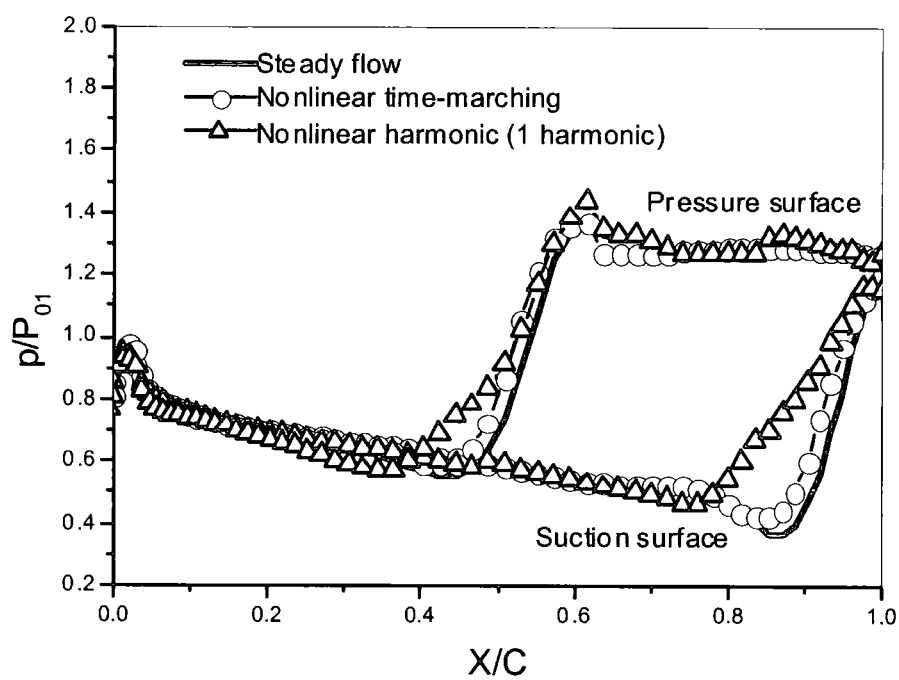
Fig. 6.25 Comparison of blade surface pressure distribution between time-averaged
flow and steady flow for inlet flow distortion.
(Frequency = 267Hz, Amplitude = 10%)

Suction surface

40 ┬──────────────────────────────────

─○─ Nonlinear time-marching
══ Linear harmonic
─△─ Nonlinear harmonic (1 harmonic)

Amplitude

(plot)

0.0   0.2   0.4   0.6   0.8   1.0

X/C

Pressure surface

40 ┬──────────────────────────────────

─○─ Nonlinear time-marching
══ Linear harmonic
─△─ Nonlinear harmonic (1 harmonic)

Amplitude

(plot)

0.0   0.2   0.4   0.6   0.8   1.0

X/C
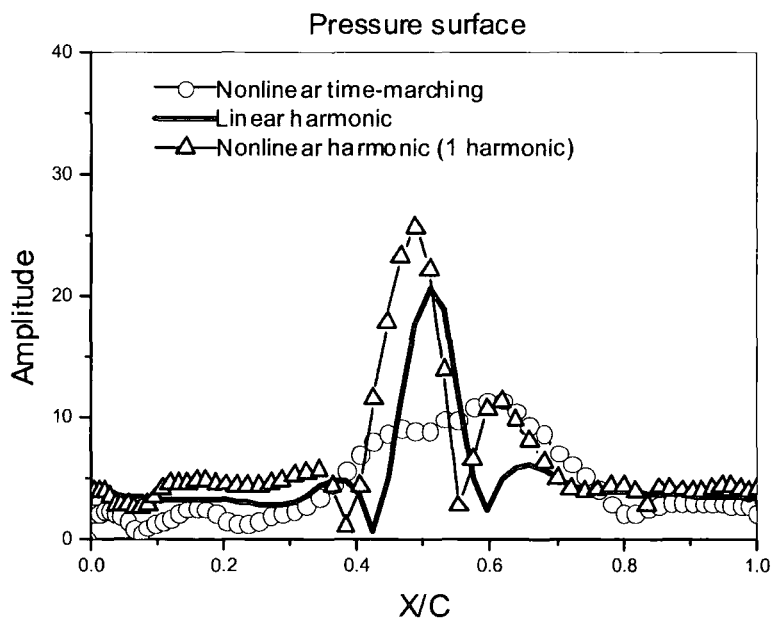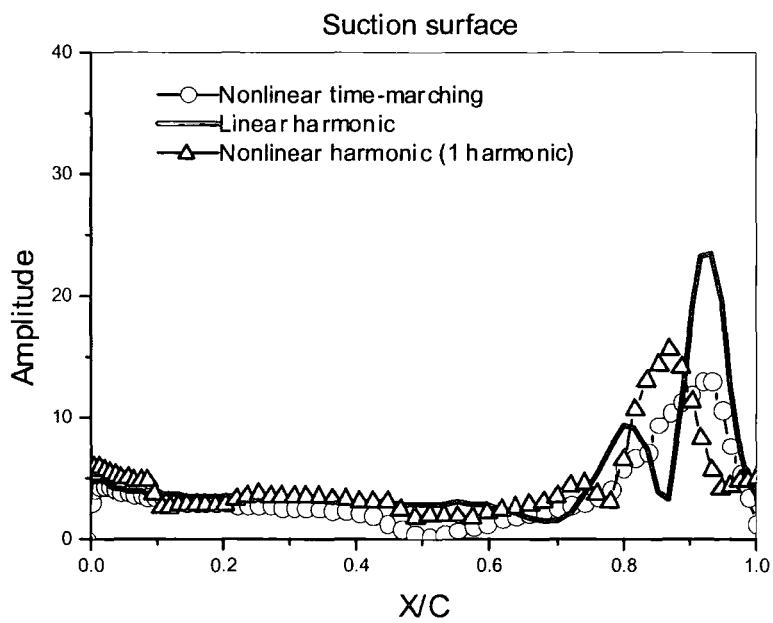
Fig. 6.26 Amplitude of unsteady blade surface pressure coefficient for inlet flow
distortion. (Frequency = 267Hz, Amplitude = 10%)
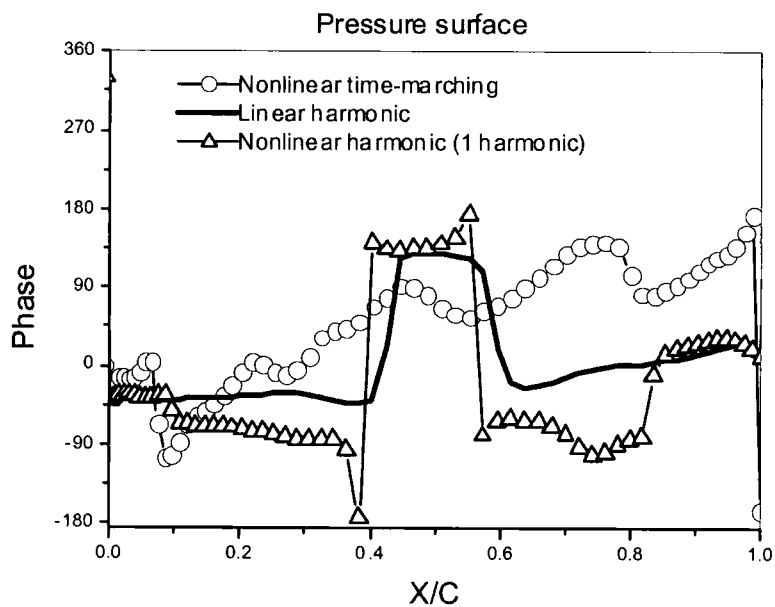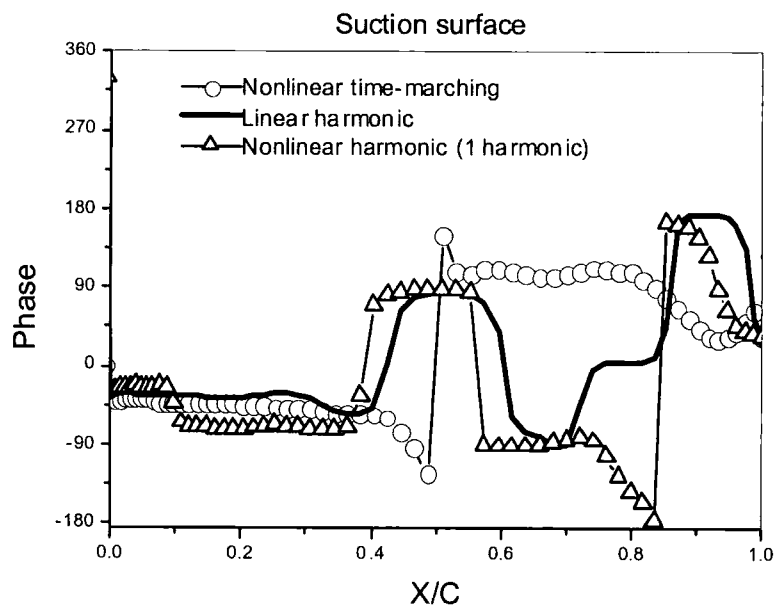
Fig. 6.27 Phase of unsteady blade surface pressure coefficient for inlet flow distortion. (Frequency = 267Hz, Amplitude = 10%)
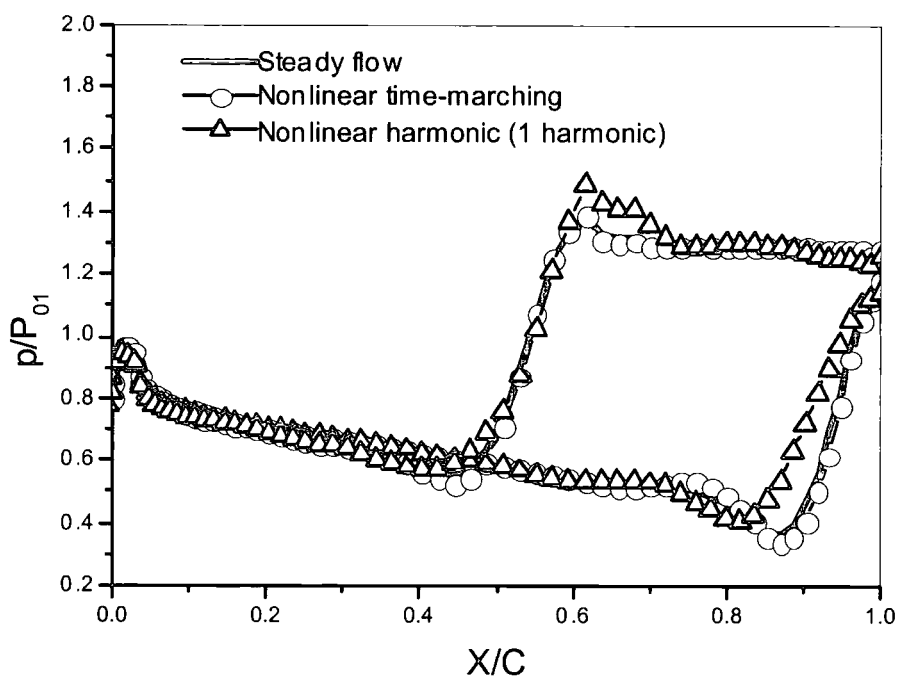
Fig. 6.28 Comparison of blade surface pressure distribution between time-averaged
flow and steady flow for inlet flow distortion.
(Frequency = 1069Hz, Amplitude = 10%)
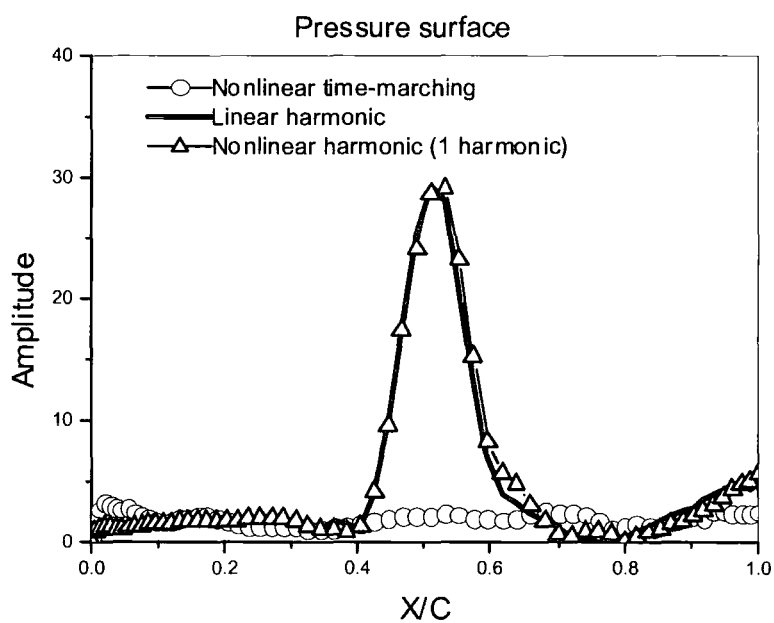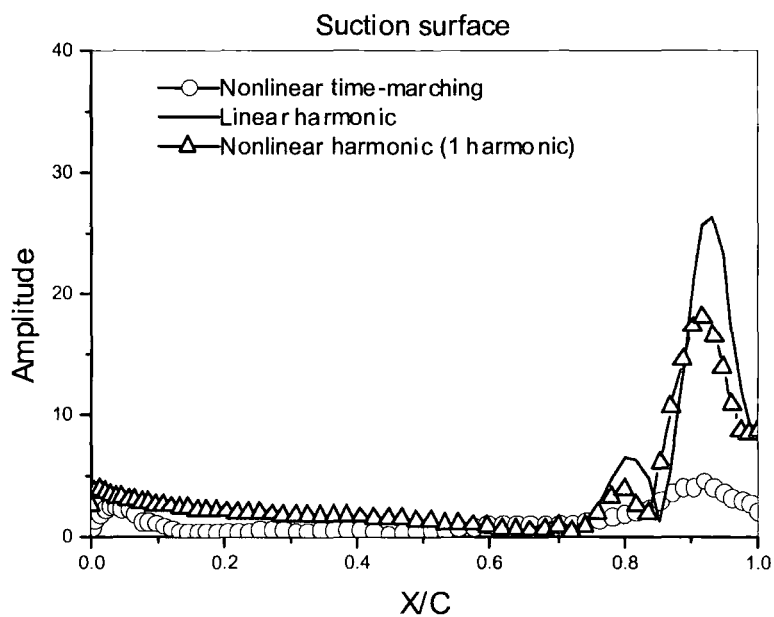
Fig. 6.29 Amplitude of unsteady blade surface pressure coefficient for inlet flow
distortion. (Frequency = 1069Hz, Amplitude = 10%)
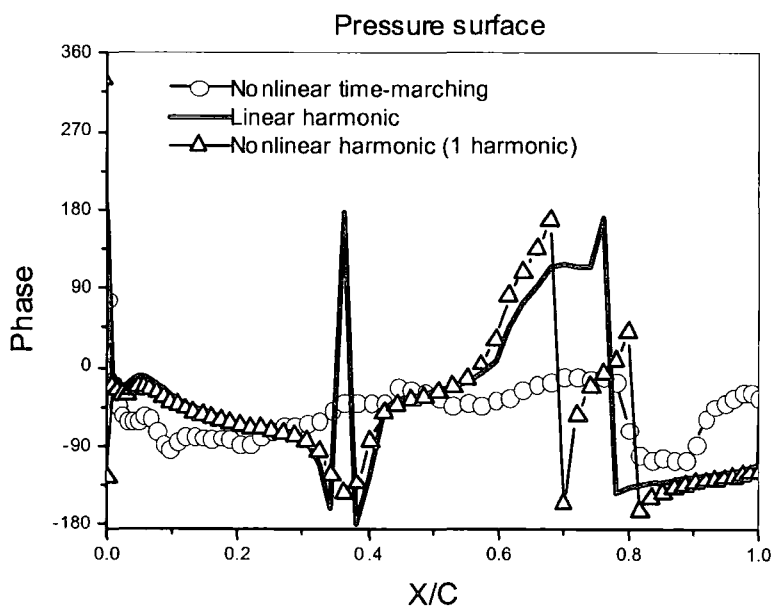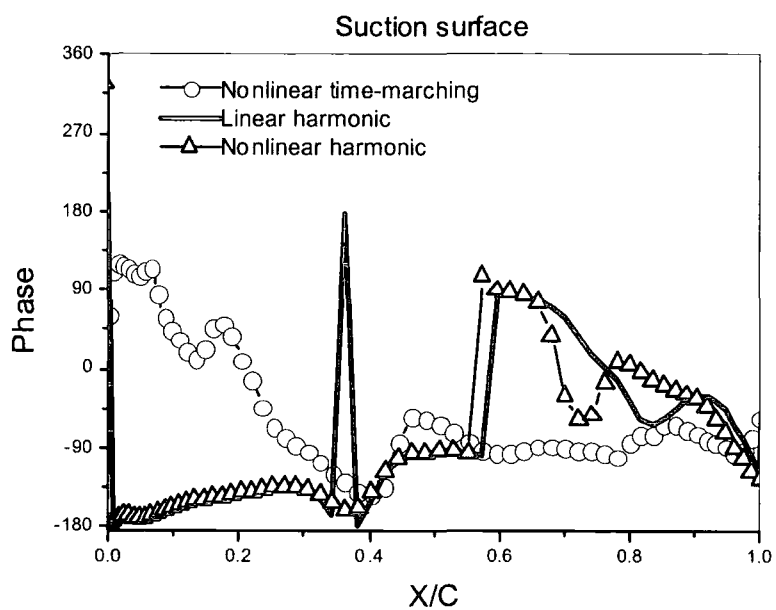
Fig. 6.30 Phase of unsteady blade surface pressure coefficient for inlet flow
distortion. (Frequency = 1069Hz, Amplitude = 10%)
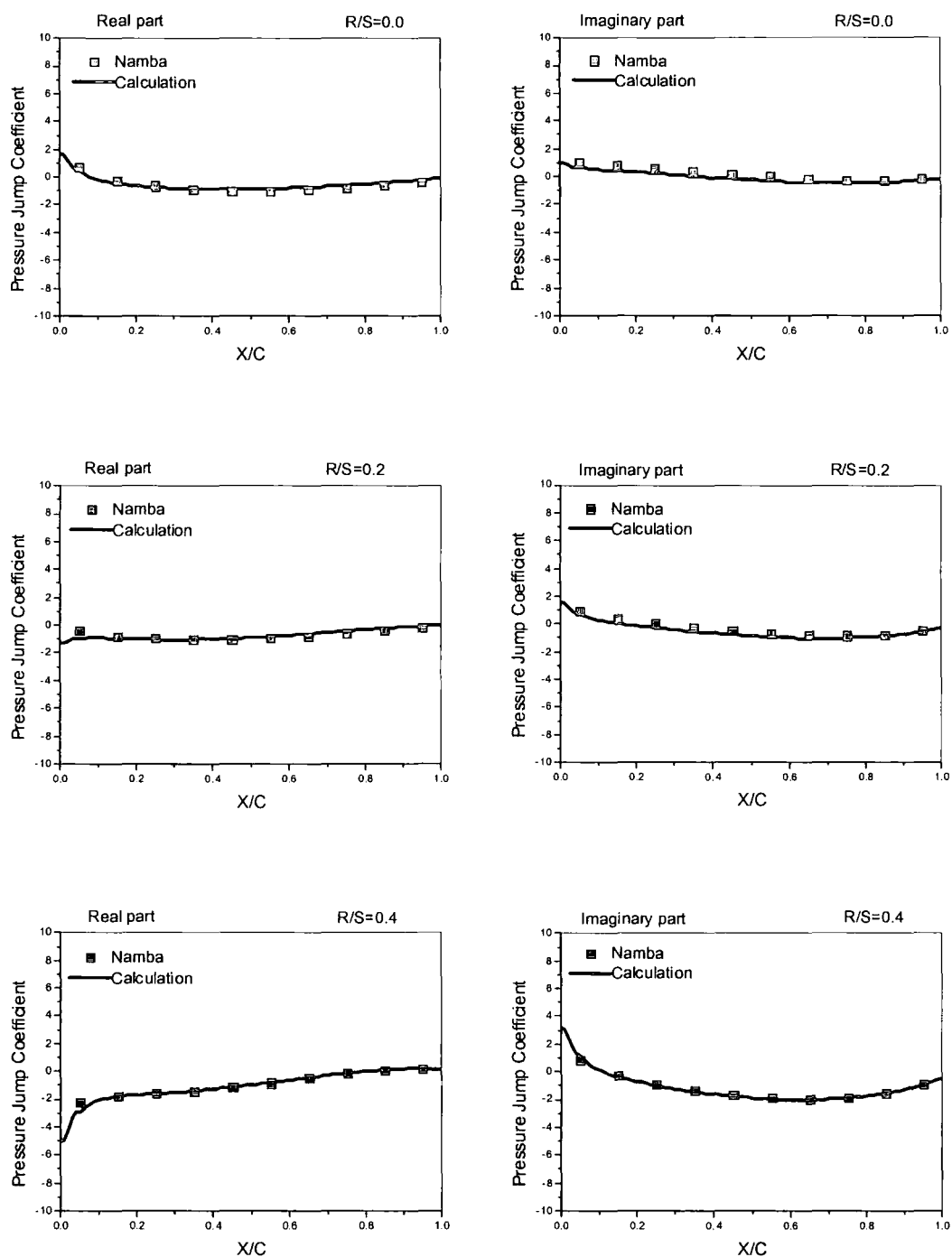
Fig. 7.1 Real and Imaginary parts of pressure jump coefficients for an oscillating
flat plate cascade. (Inter-blade phase angle = 0 deg)
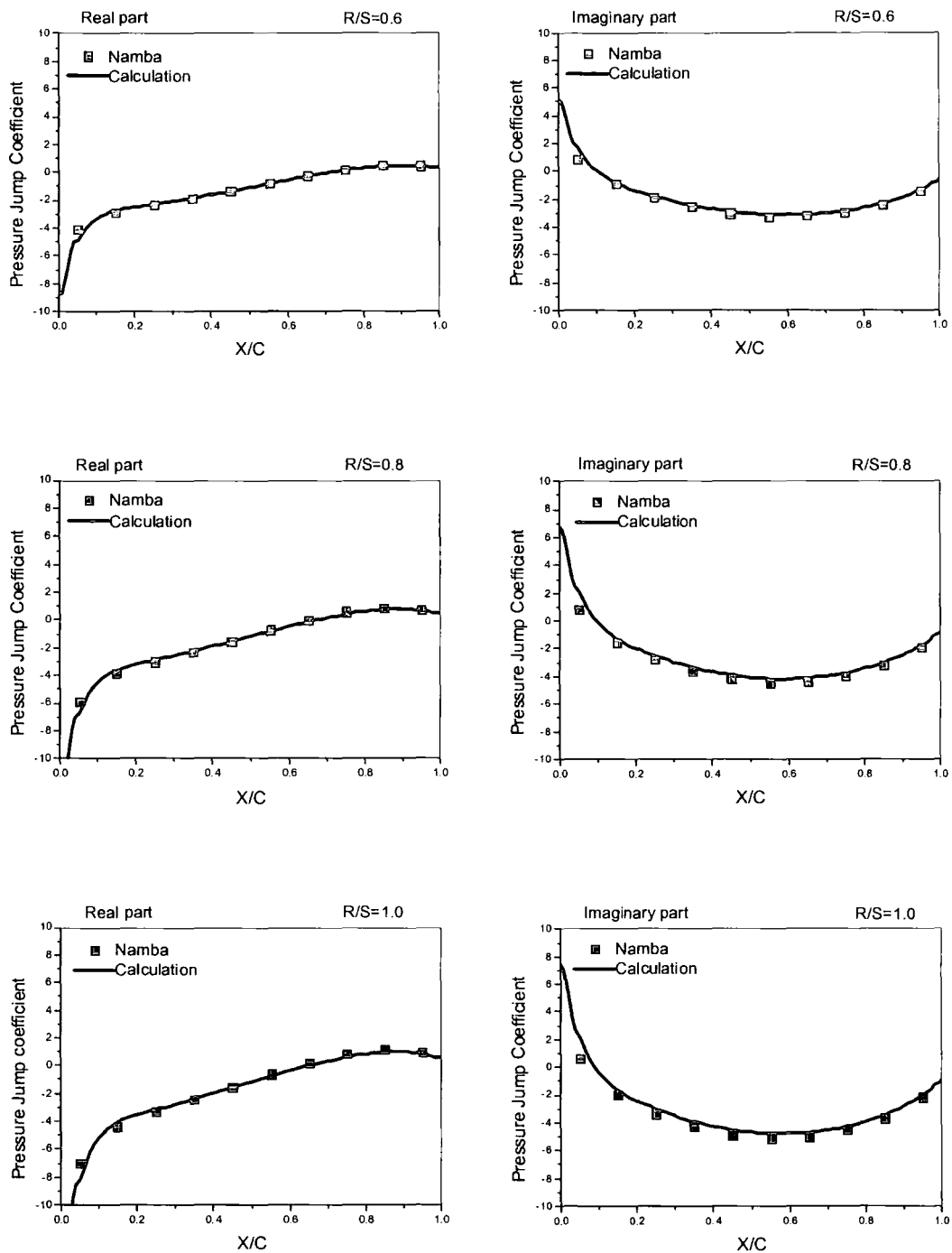
Fig. 7.2 Real and Imaginary parts of pressure jump coefficients for an oscillating
flat plate cascade. (Inter-blade phase angle = 0 deg)
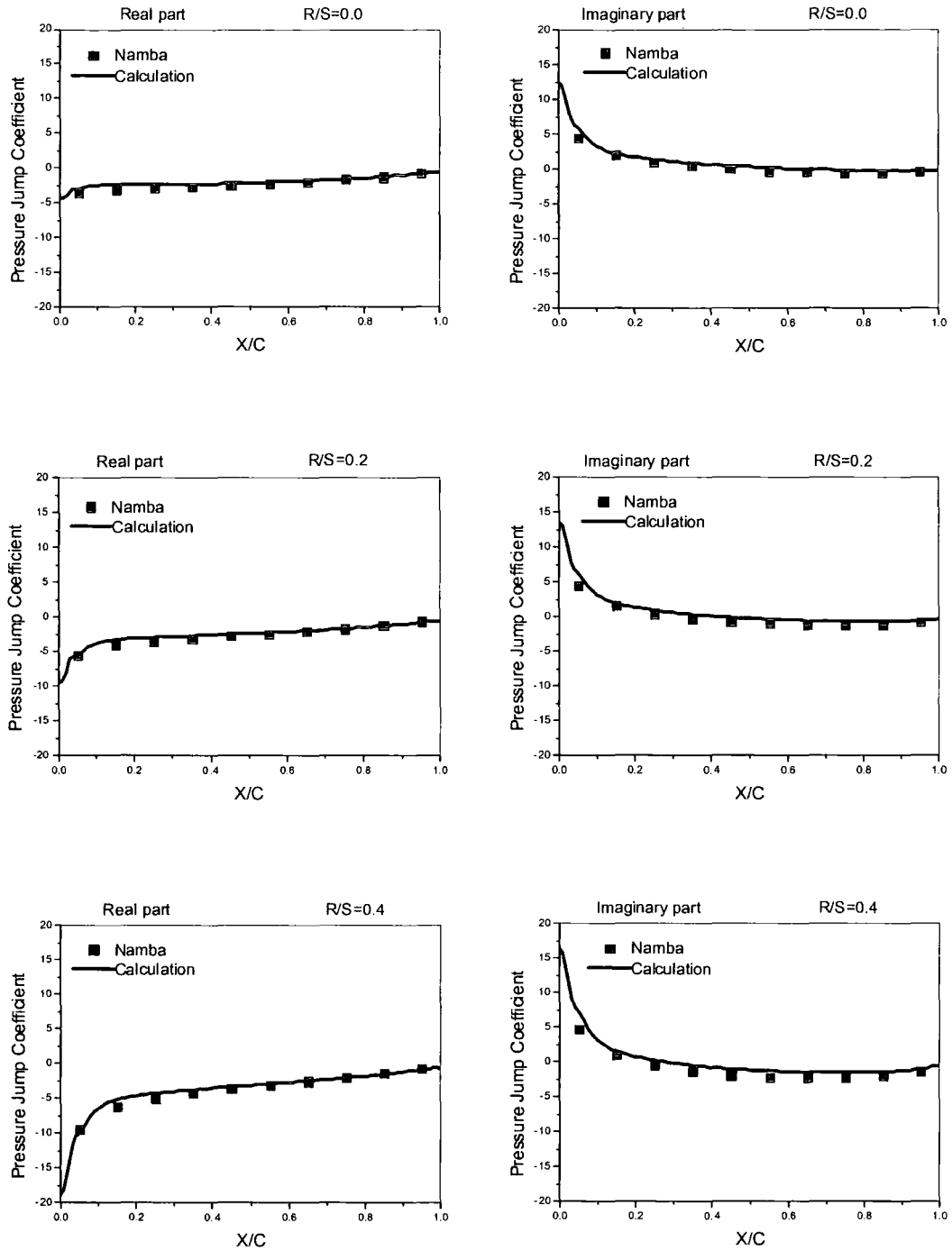
Fig. 7.3 Real and Imaginary parts of pressure jump coefficients for an oscillating flat plate cascade. (Inter-blade phase angle = 180 deg)
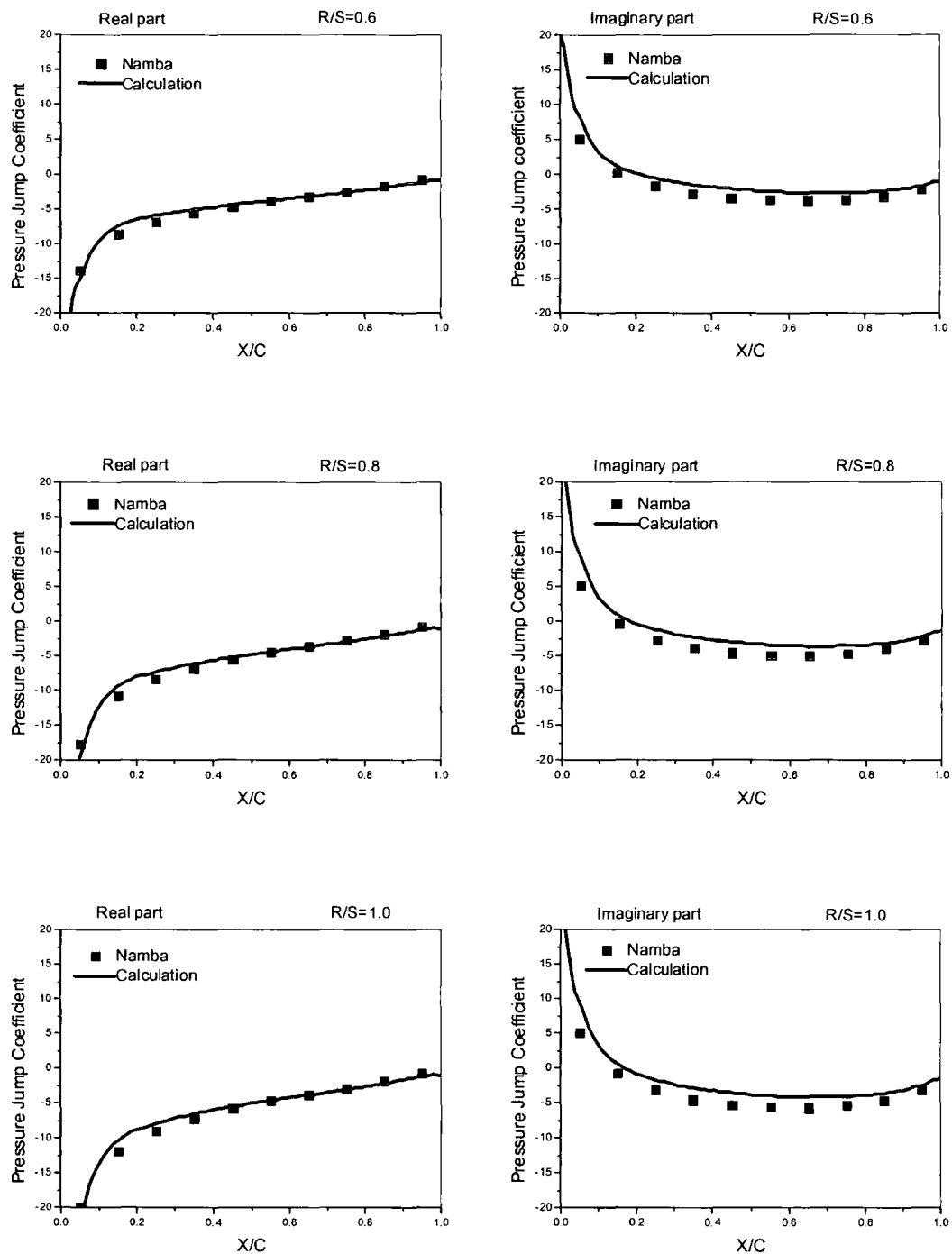
Fig. 7.4 Real and Imaginary parts of pressure jump coefficients for an oscillating
flat plate cascade. (Inter-blade phase angle = 180 deg)
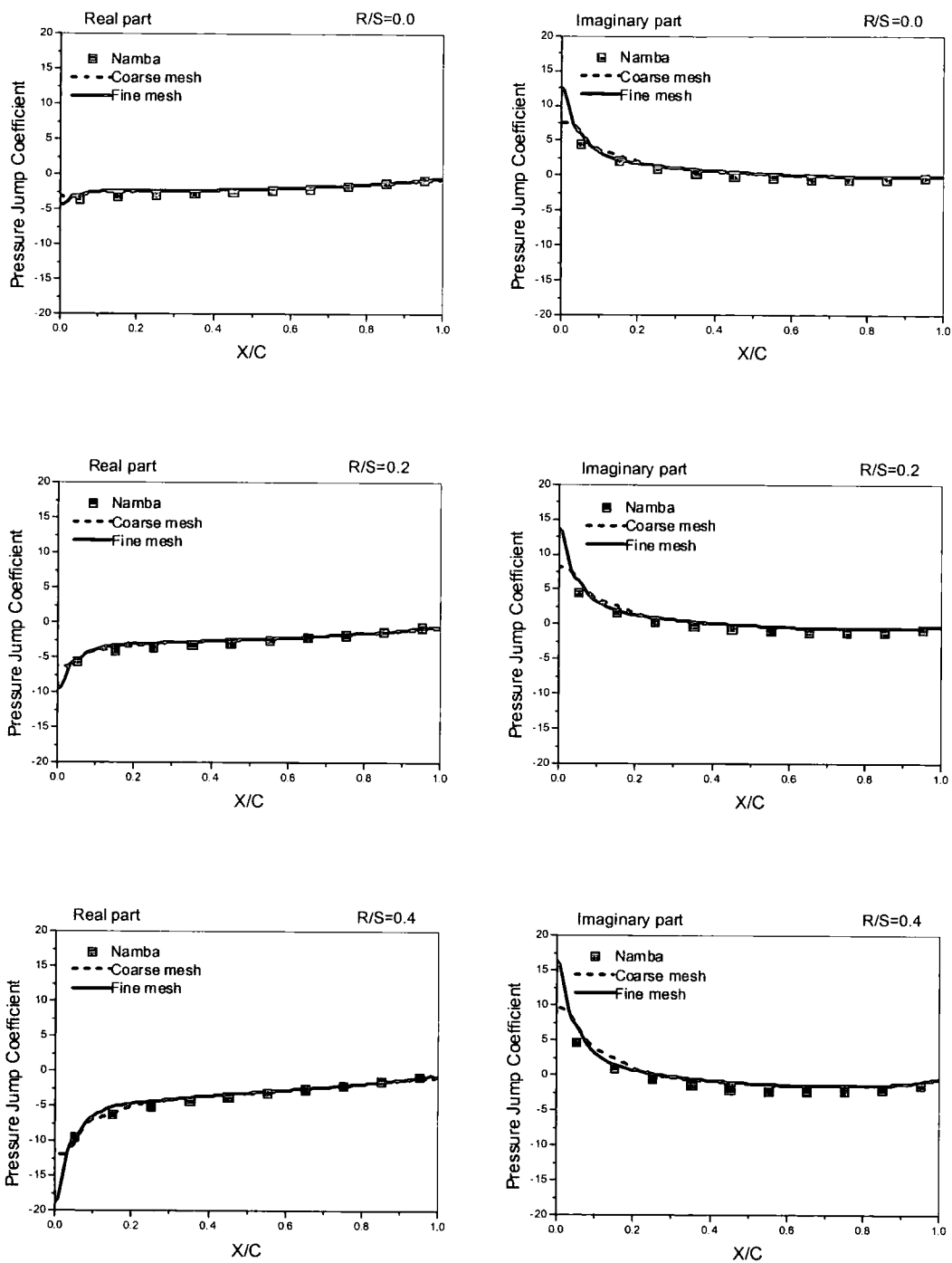
Fig. 7.4a Real and Imaginary parts of pressure jump coefficients for an oscillating flat plate cascade (IBPA=180°; Coarse mesh=81x21x21; Fine mesh=161x41x41)
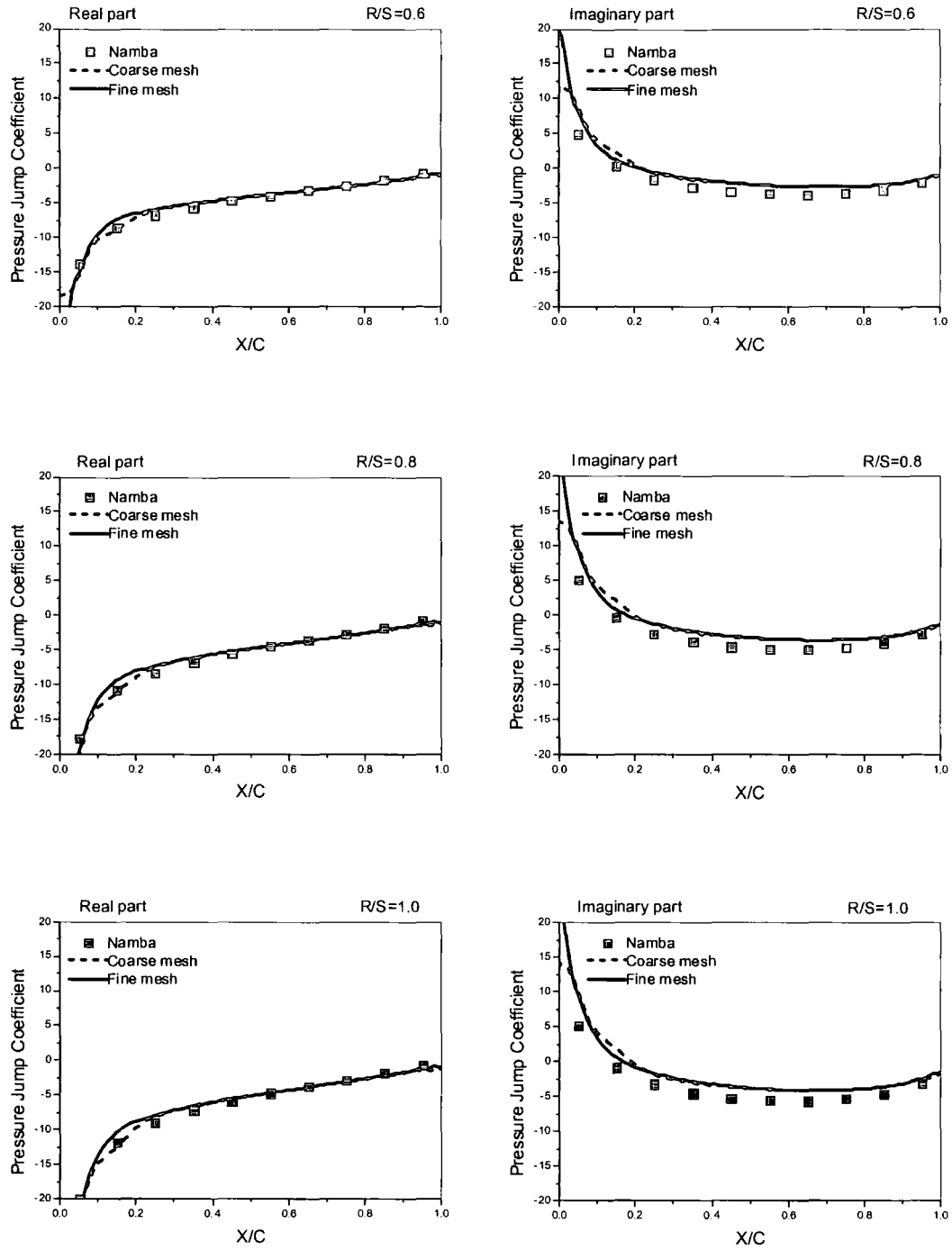
Fig. 7.4b Real and Imaginary parts of pressure jump coefficients for an oscillating flat plate cascade (IBPA=180°; Coarse mesh=81x21x21; Fine mesh=161x41x41)
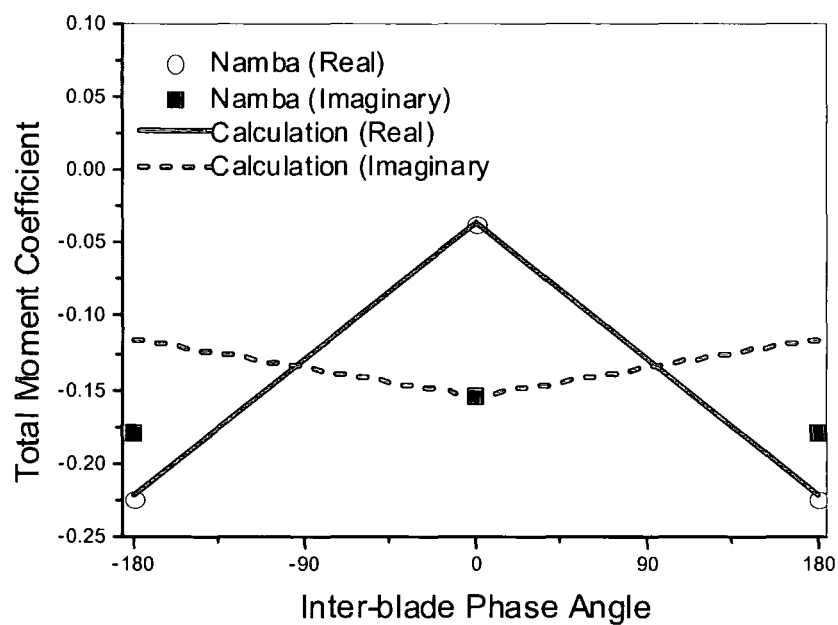
Fig. 7.5 Real and Imaginary parts of total moment coefficient for an oscillating
flat plate cascade. (Reduced frequency = 1.0)

Fig. 7.6a Controlled diffusion airfoil blade of the oscillating compressor cascade
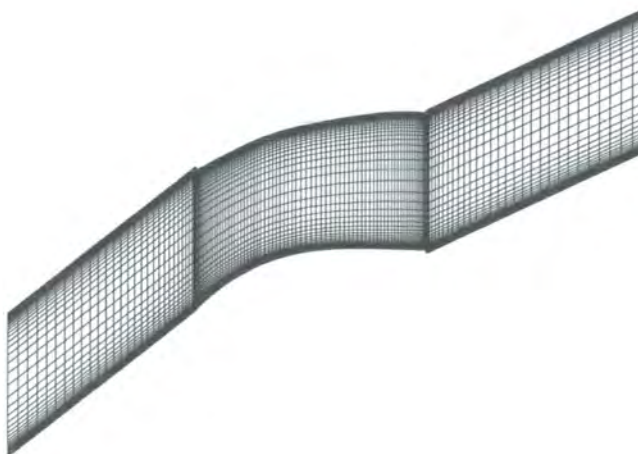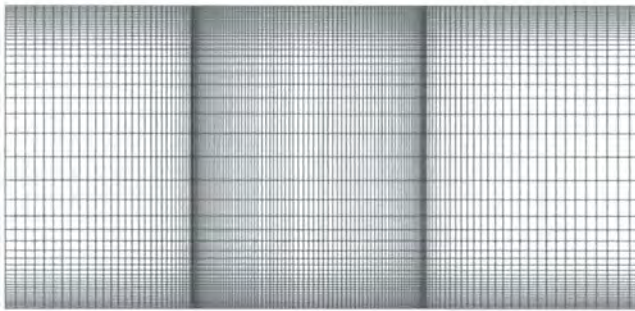
Fig. 7.6b Side view and blade-to-blade view of the computational mesh
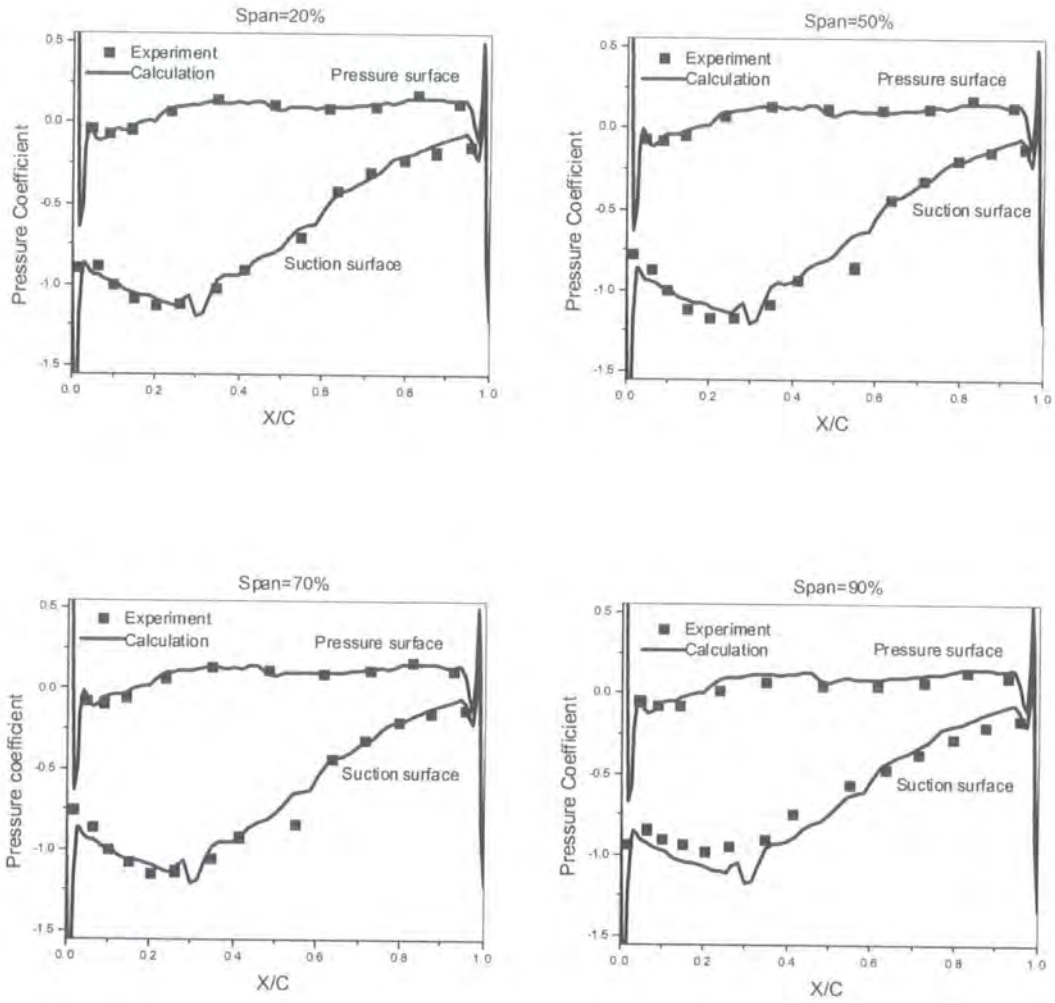
Fig. 7.7 Comparison of blade surface pressure distribution for steady flow at different
spanwise locations for oscillating linear compressor cascade.
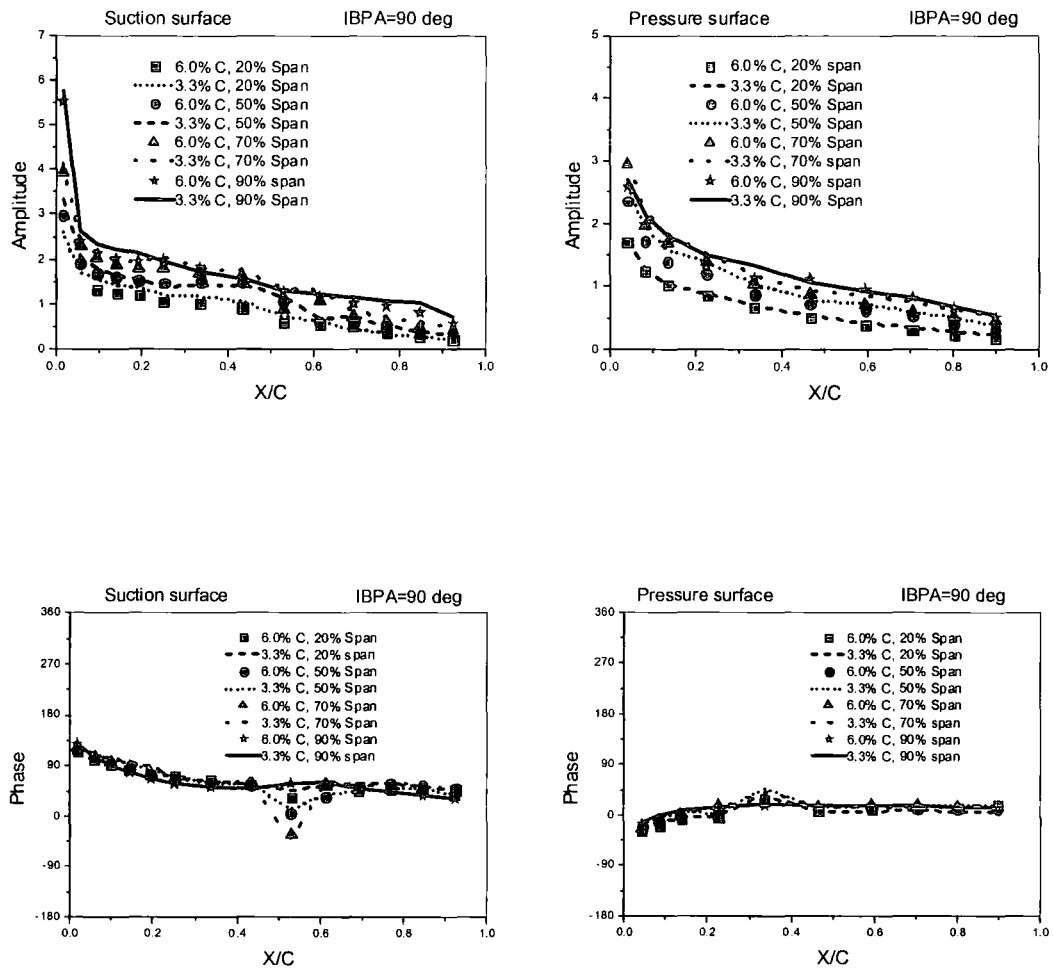
Fig. 7.7a Amplitude and phase of unsteady pressure coefficient at two bending
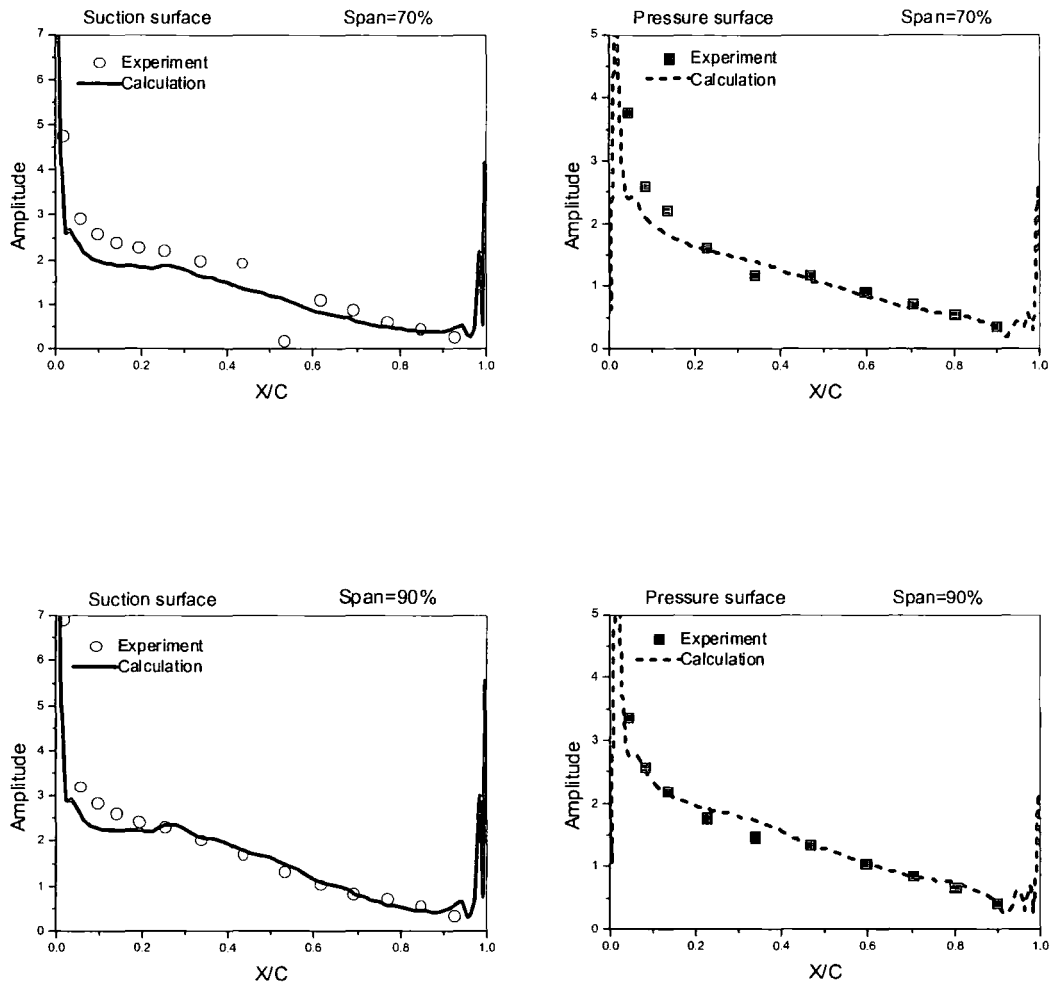amplitudes of 6.0% and 3.3% of chord. (Reduced frequency=0.4)
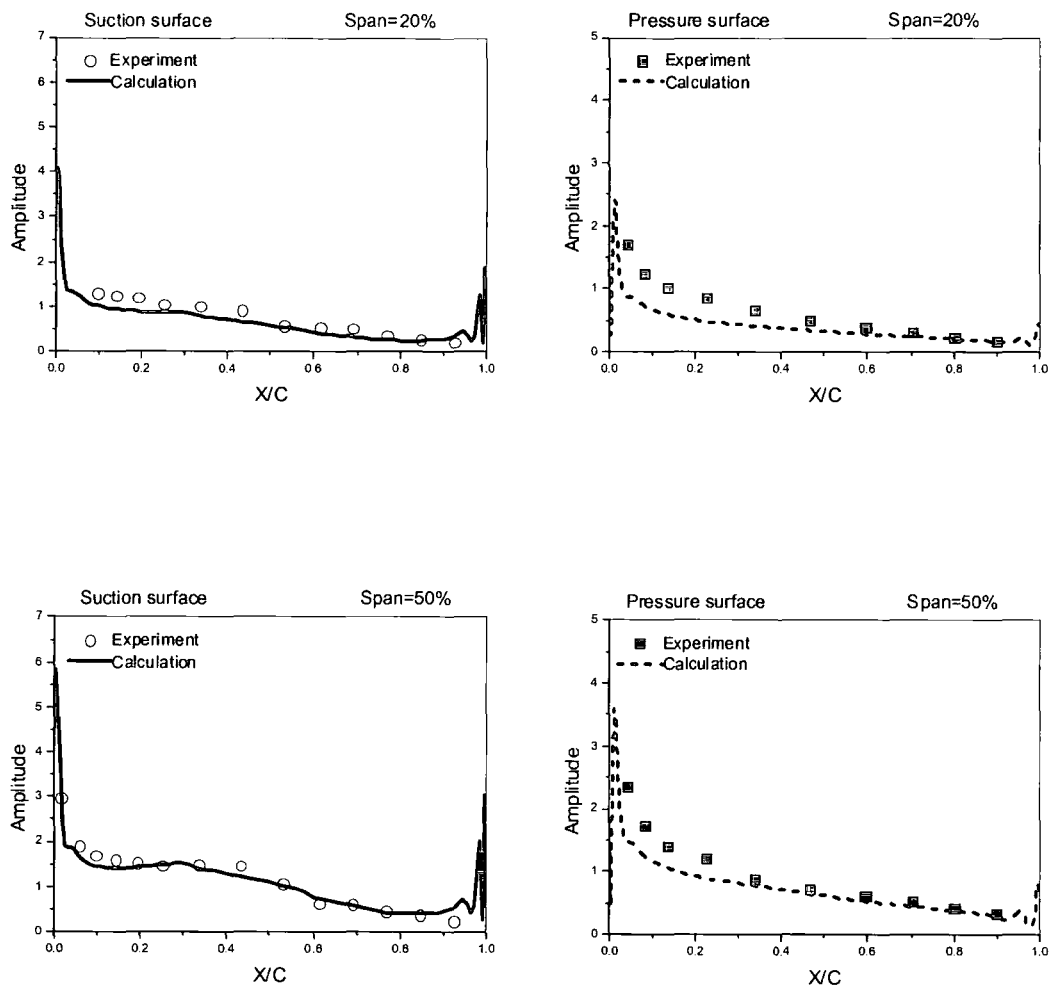
Fig. 7.8 Amplitude of unsteady pressure coefficient for oscillating cascade
(Reduced Frequency = 0.4 , Inter-blade phase angle = 90 deg)
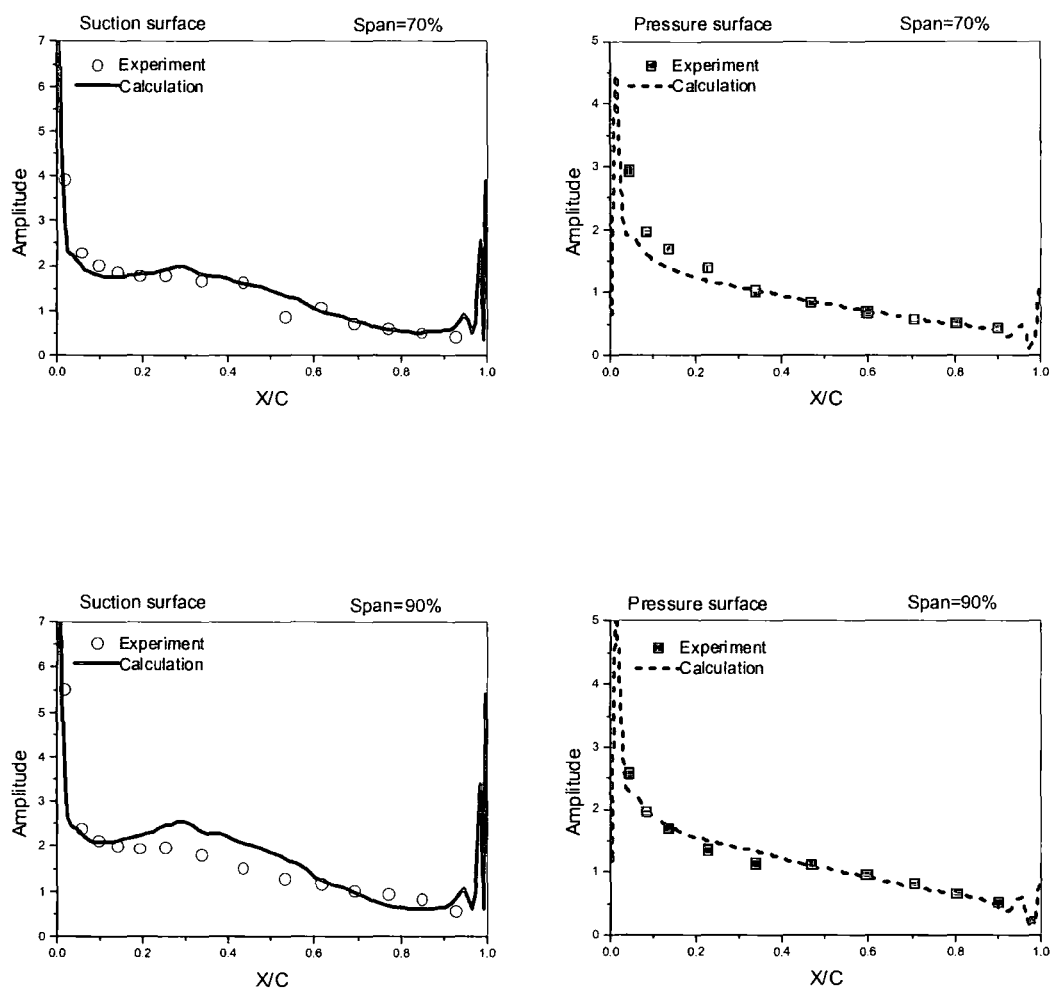
Fig. 7.9 Amplitude of unsteady pressure coefficient for oscillating cascade
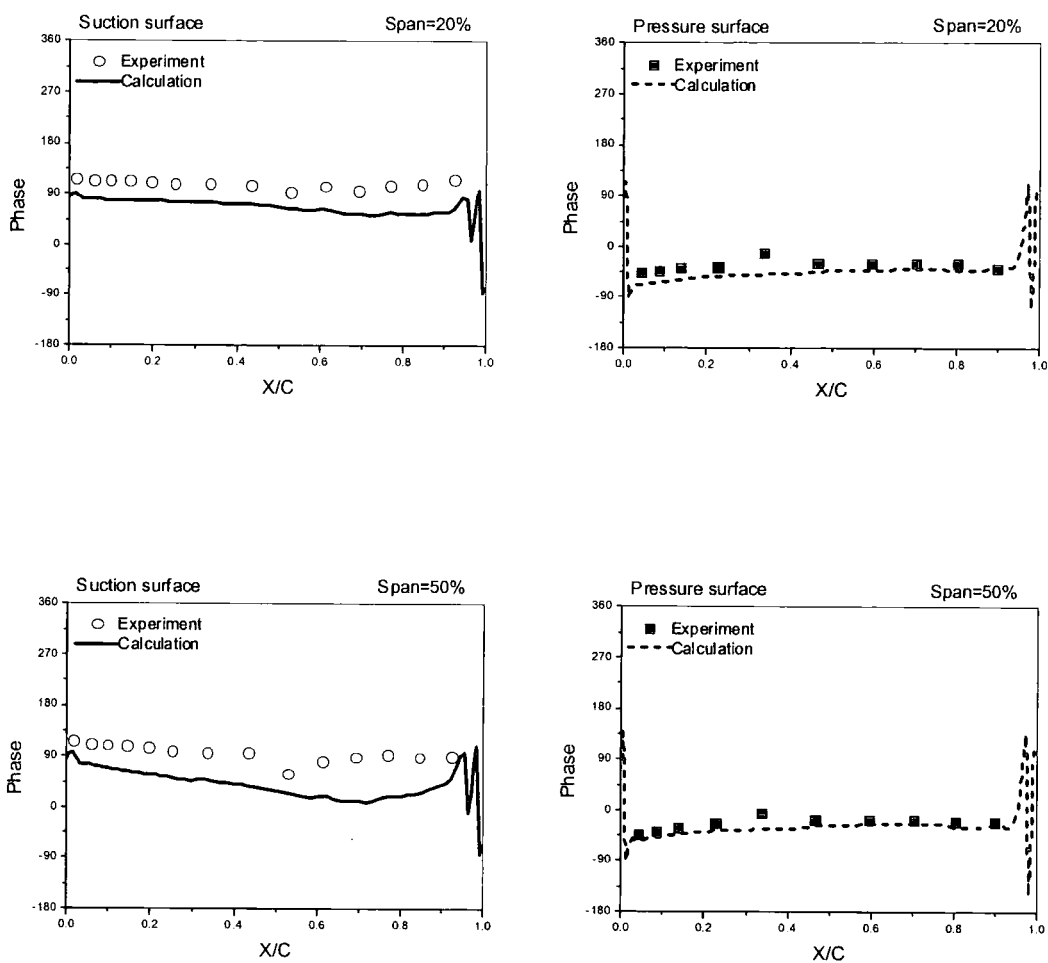(Reduced Frequency = 0.4 , Inter-blade phase angle = 90 deg)

Fig. 7.10 Phase of unsteady pressure coefficient for oscillating cascade
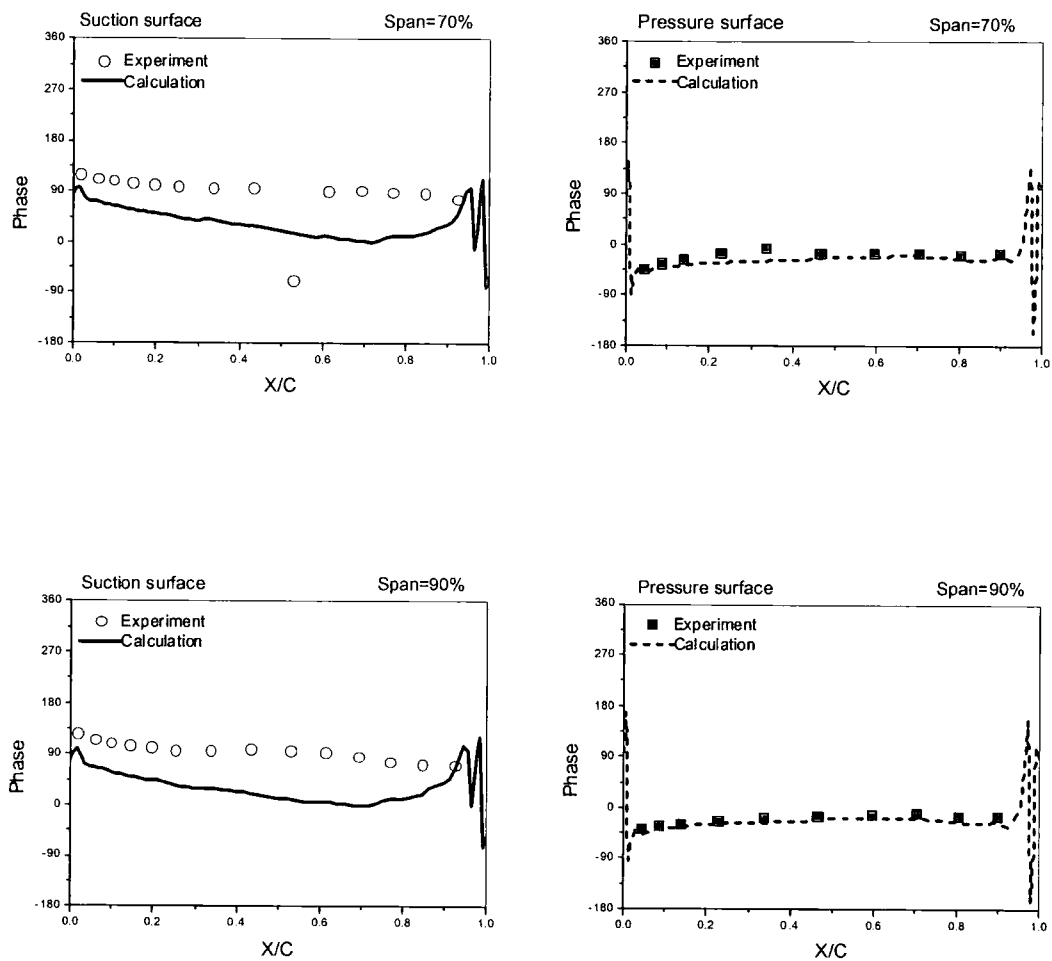(Reduced Frequency = 0.4 , Inter-blade phase angle = 90 deg)

Suction surface   Span=70%

Pressure surface   Span=70%

○ Experiment
— Calculation

▣ Experiment
- - - Calculation

Phase

Phase

360
270
180
90
0
-90
-180

360
270
180
90
0
-90
-180

0.0   0.2   0.4   0.6   0.8   1.0

X/C

X/C

Suction surface   Span=90%

Pressure surface   Span=90%

○ Experiment
— Calculation

▣ Experiment
- - - Calculation

Phase

Phase

X/C

X/C
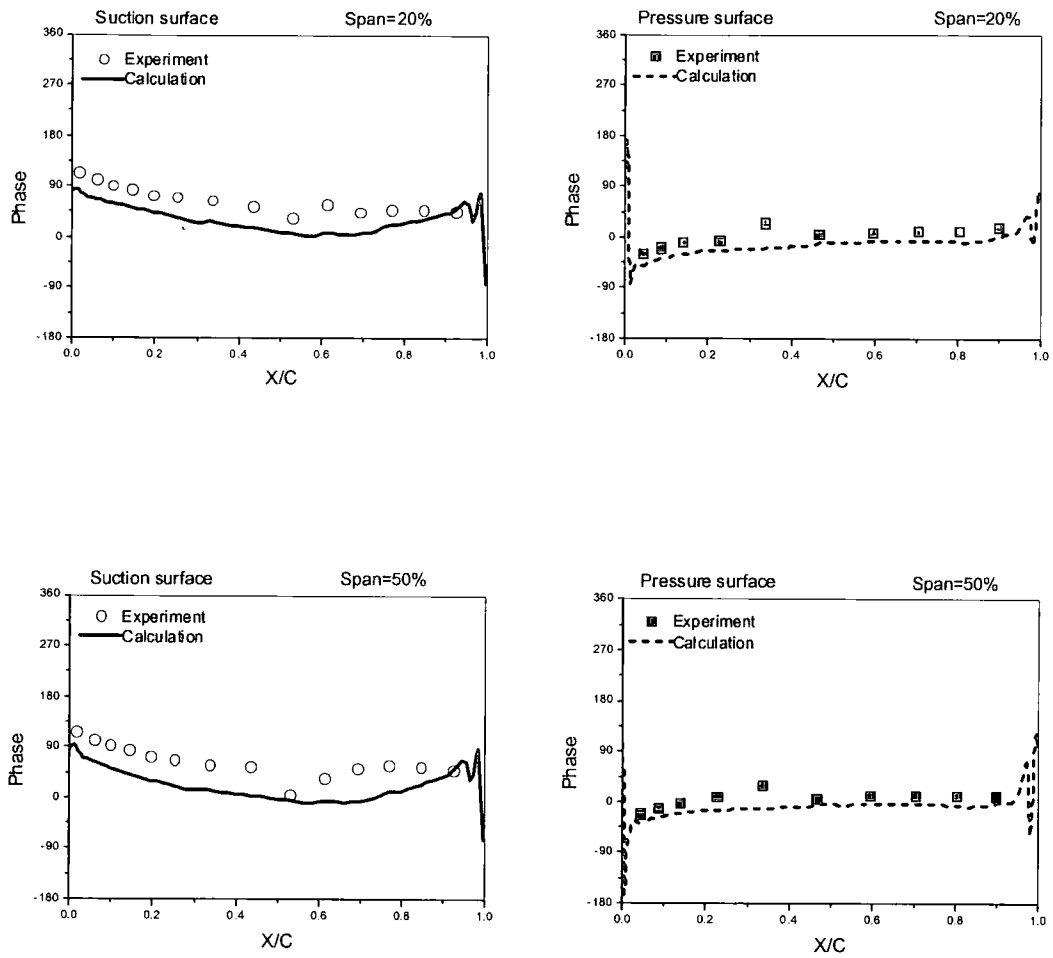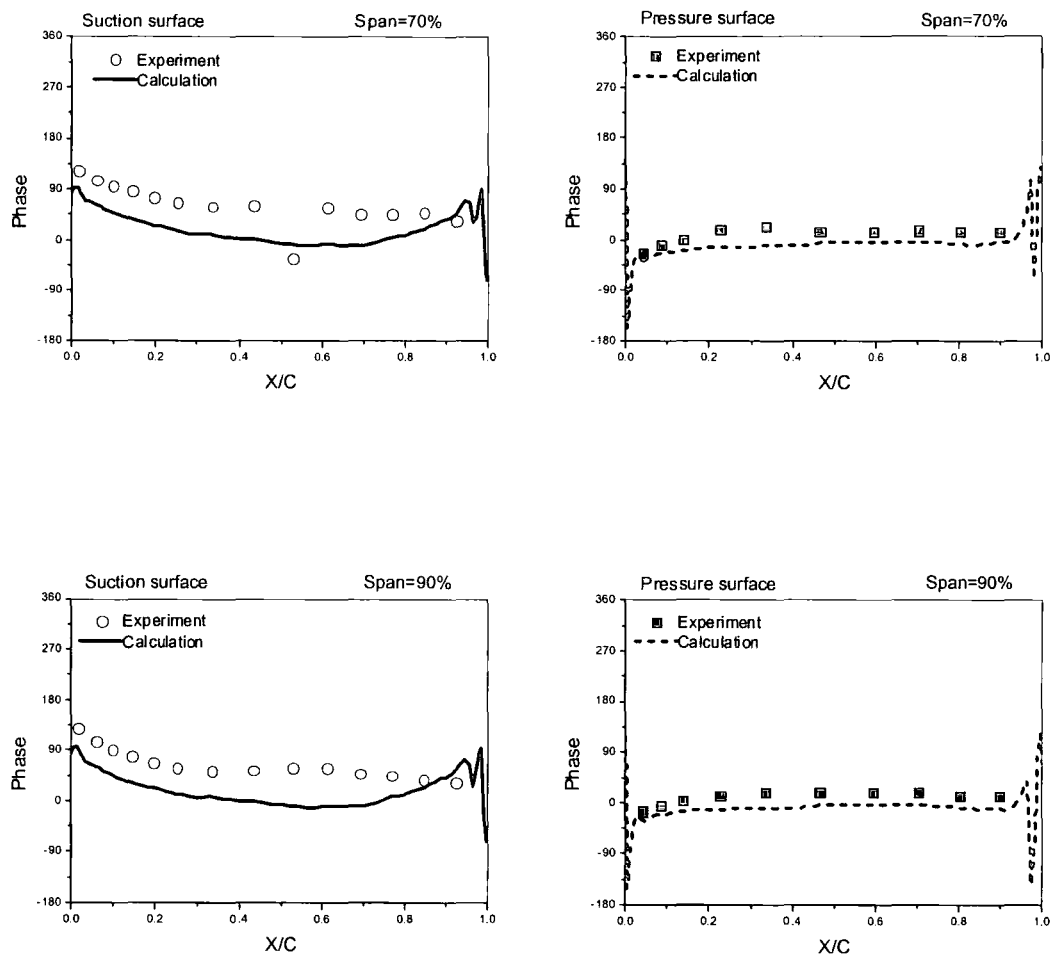
Fig. 7.11 Phase of unsteady pressure coefficient for oscillating cascade
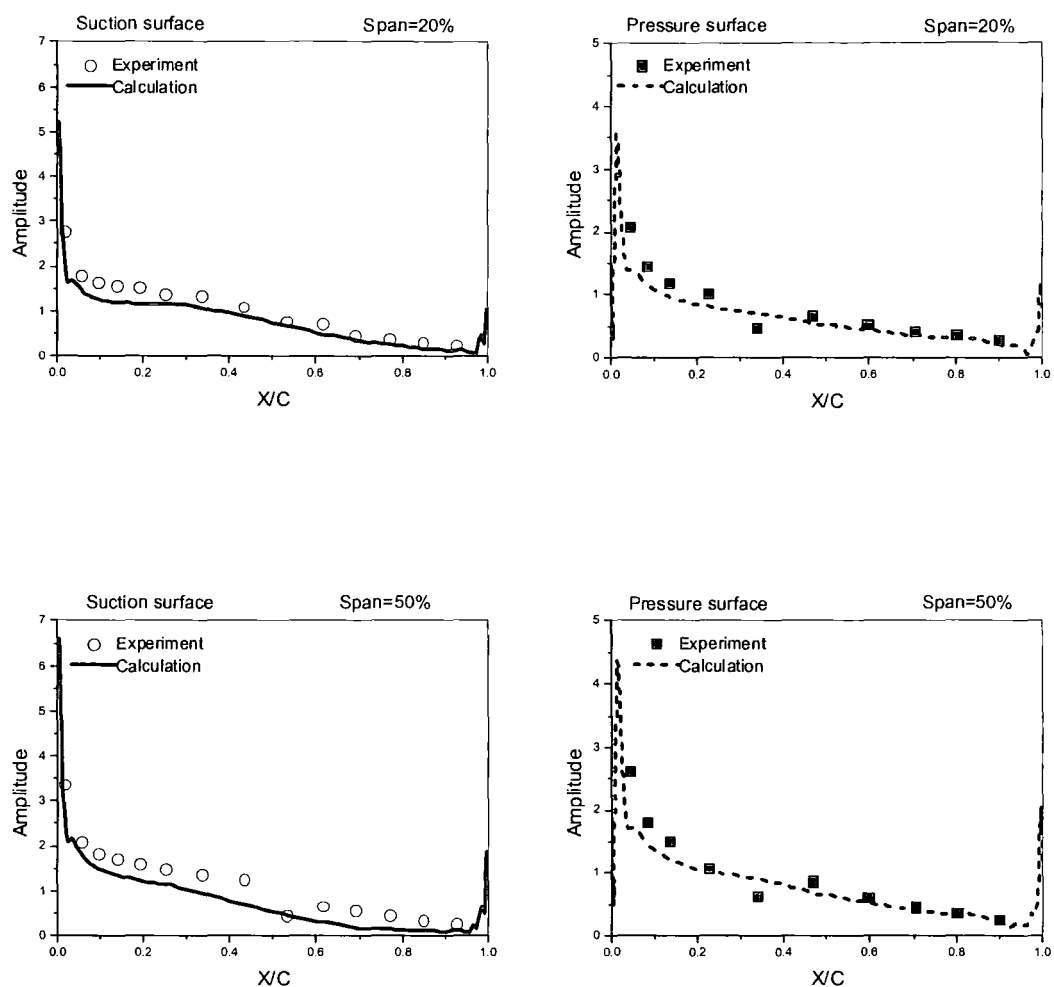(Reduced Frequency = 0.4 , Inter-blade phase angle = 90 deg)
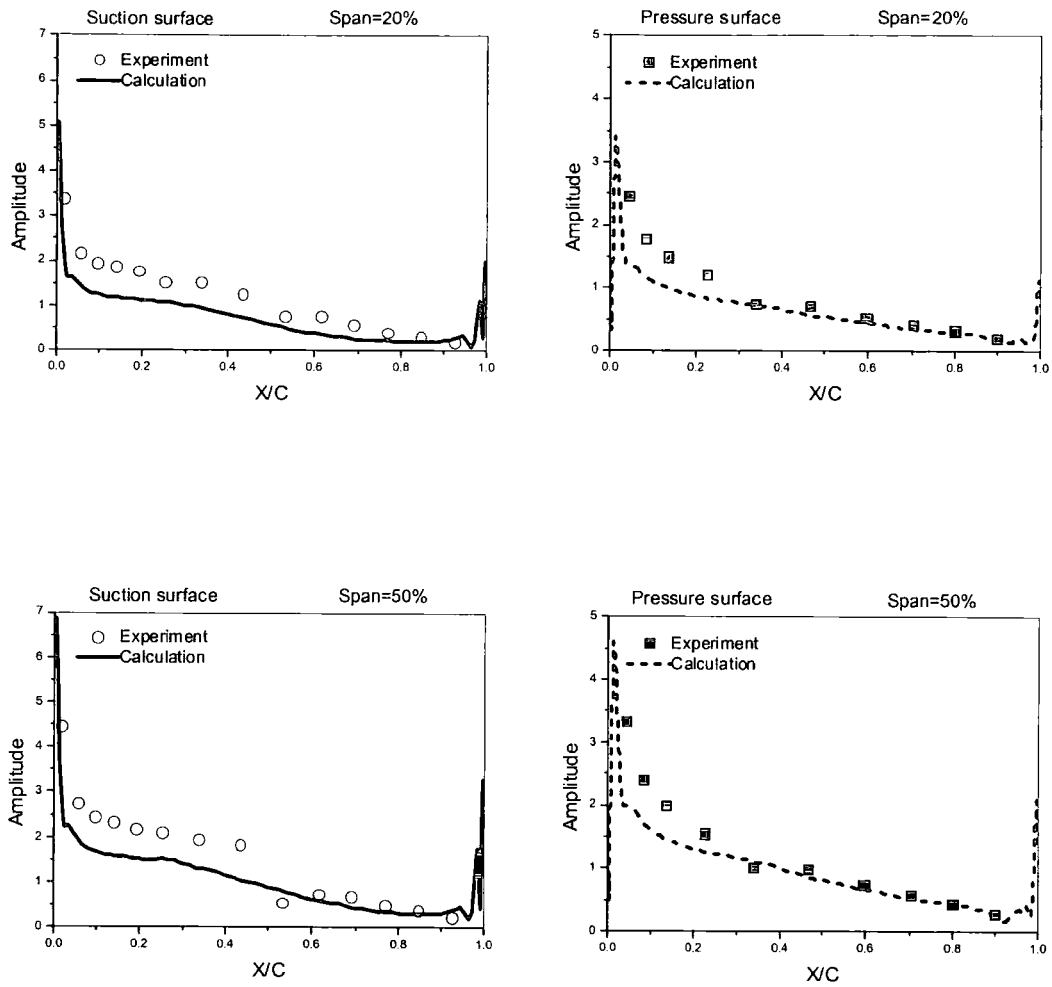
Fig. 7.12 Amplitude of unsteady pressure coefficient for oscillating cascade
(Reduced Frequency = 0.4 , Inter-blade phase angle = 180 deg)

Fig. 7.13 Amplitude of unsteady pressure coefficient for oscillating cascade
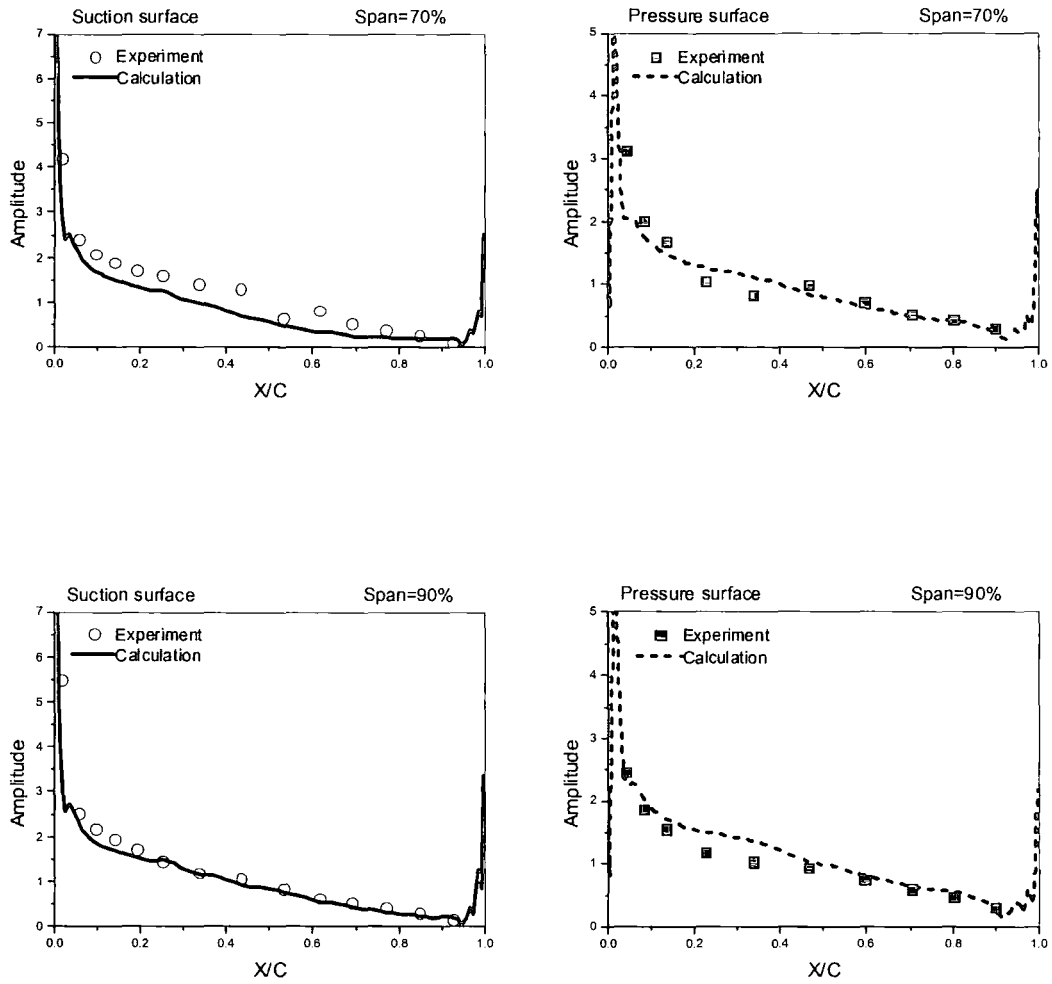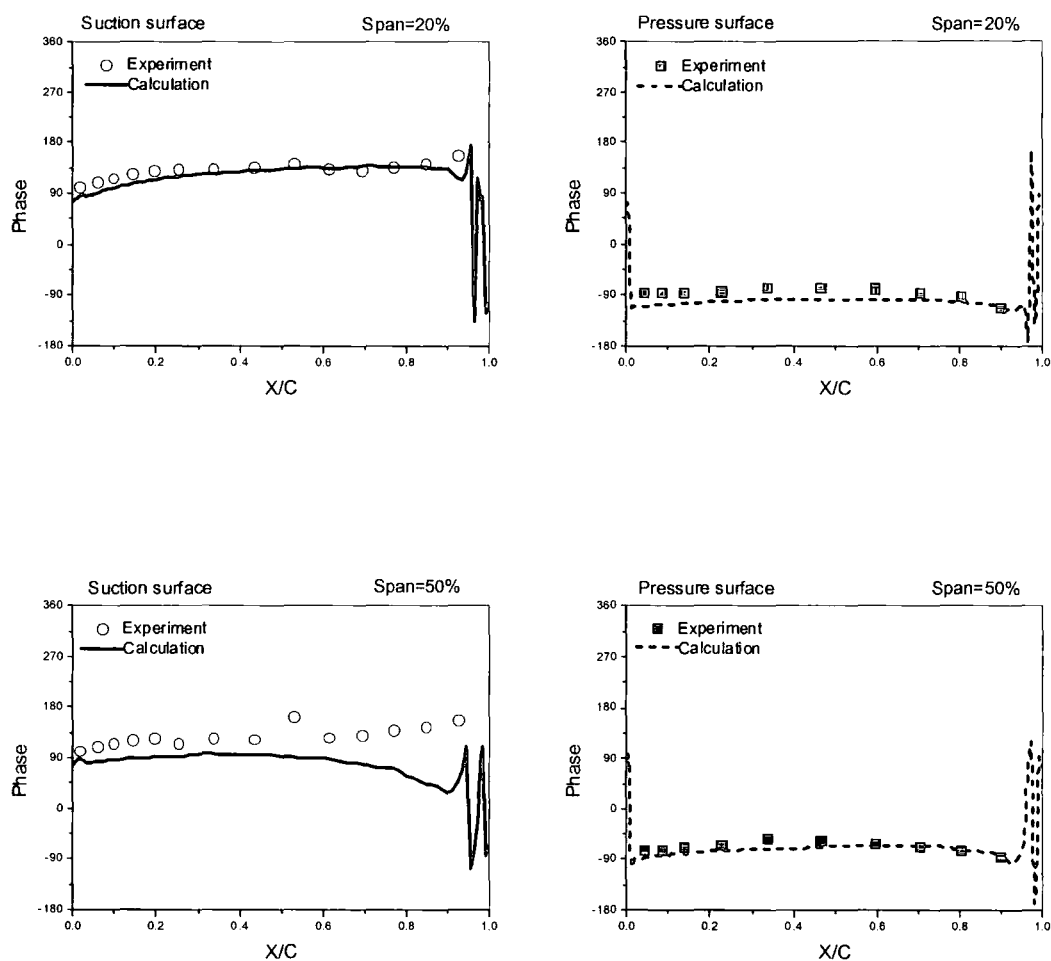(Reduced Frequency = 0.4 , Inter-blade phase angle = 180 deg)

Fig. 7.14 Phase of unsteady pressure coefficient for oscillating cascade
(Reduced Frequency = 0.4 , Inter-blade phase angle = 180 deg)

Fig. 7.15 Phase of unsteady pressure coefficient for oscillating cascade
(Reduced Frequency = 0.4 , Inter-blade phase angle = 180 deg)

Fig. 7.16 Amplitude of unsteady pressure coefficient for oscillating cascade
(Reduced Frequency = 0.4 , Inter-blade phase angle = -90 deg)

Fig. 7.17 Amplitude of unsteady pressure coefficient for oscillating cascade
(Reduced Frequency = 0.4 , Inter-blade phase angle = -90 deg)

Fig. 7.18 Phase of unsteady pressure coefficient for oscillating cascade
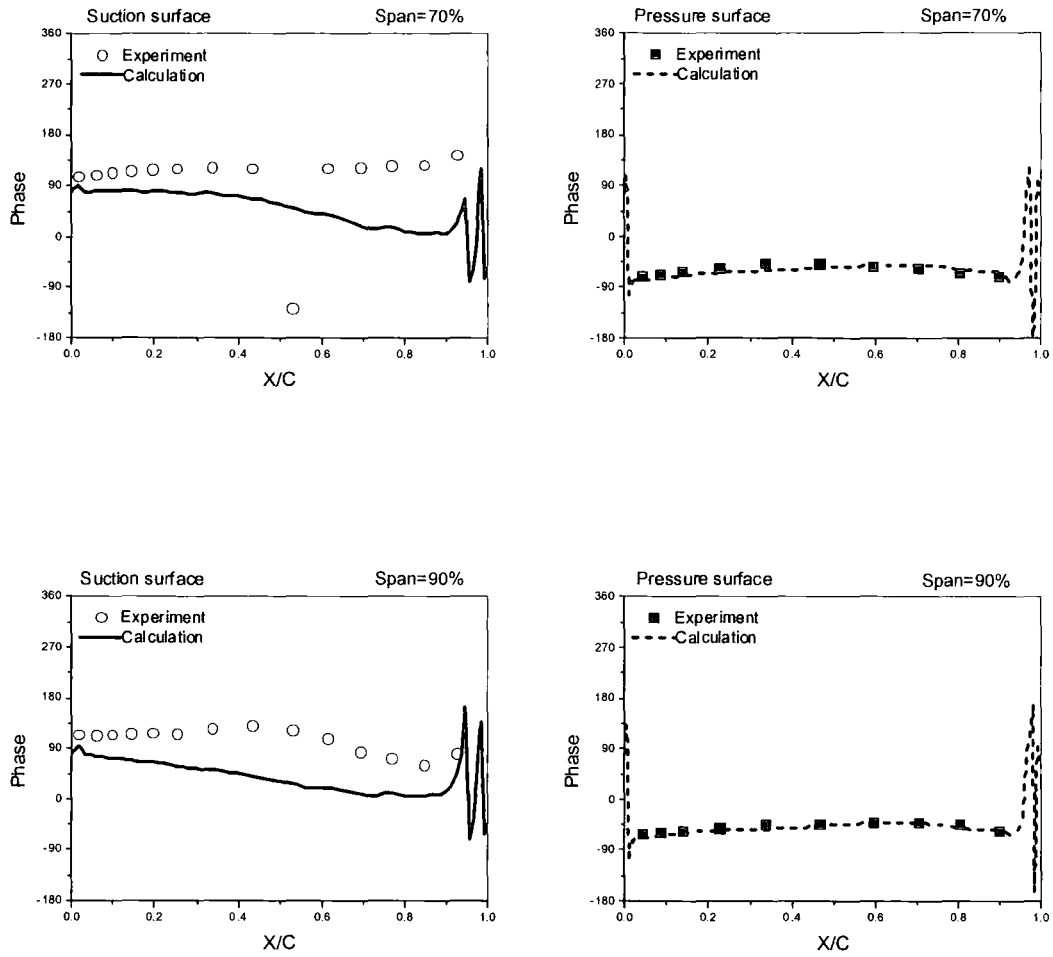(Reduced Frequency = 0.4 , Inter-blade phase angle = -90 deg)

Fig. 7.19 Phase of unsteady pressure coefficient for oscillating cascade
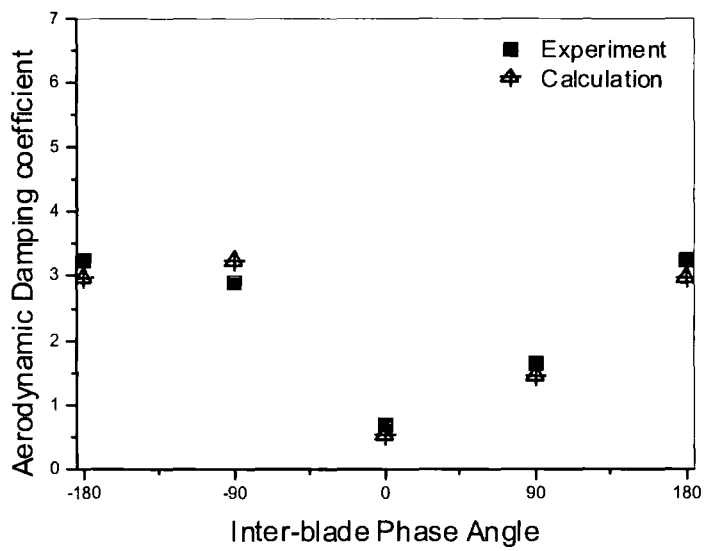(Reduced Frequency = 0.4 , Inter-blade phase angle = -90 deg)

Fig. 7.20 Aerodynamic damping coefficient in dependence of
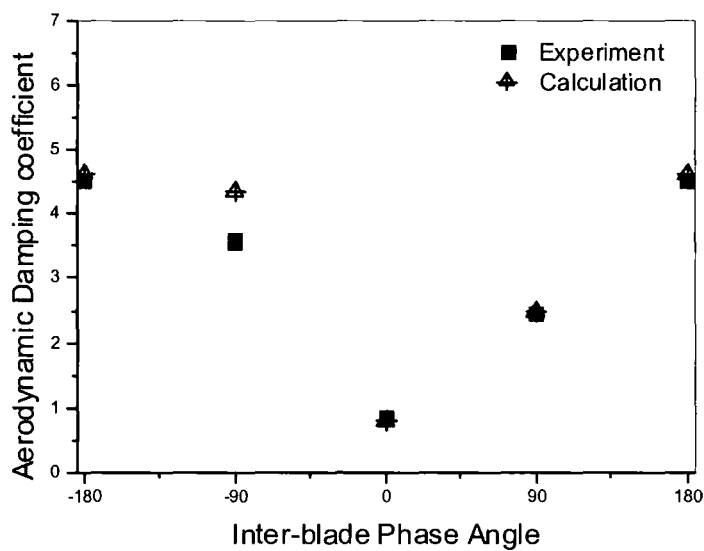inter-blade phase angle (Reduced frequency = 0.4)

Fig. 7.21 Aerodynamic damping coefficient in dependence of
inter-blade phase angle (Reduced frequency = 0.6)